

Transport in Unsaturated Porous Media

Dissertation

zur Erlangung des akademischen Grades

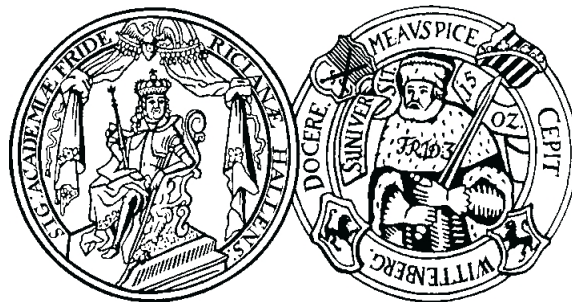
Dr. rer. nat.

vorgelegt der

Naturwissenschaftlichen Fakultät III

Institut für Geowissenschaften und Geographie

Martin-Luther-Universität Halle-Wittenberg



VON

Samuel Kwame Kumahor (MSc.)

geboren am 01.08.1981 in Ho

Datum der Einreichung: 08.08.2016

Datum der Verteidigung: 26.06.2017

Gutachter: Prof. Dr. Hans-Jörg Vogel
Prof. Dr. Wolfgang Durner

Abstract

Transport processes in unsaturated porous medium are difficult to examine due to their complex and non-linear nature. This complexity arises from, amongst others things, the occurrence of air-water interface in addition to solid-water interface for unsaturated flow. This thesis investigates the following: (i) dispersivity of inert solute as a function of water content, $\lambda(\theta)$, and (ii) transport and reactivity of citrate-coated and soil-aged Ag nanoparticles (NPs) as a function of hydrologic and chemical factors by establishing constant flux and constant pressure head (i.e., unit gradient unsaturated flow) along a repacked sand column. The major findings include: (i) transport of both the inert solute and the Ag NPs (citrate-coated and soil-aged) is sensitive to the geometry of flow field and this depends on structure of pore network, which in turn depends on flow rate (j_w) and degree of water saturation for unsaturated flow, as controlled by flux boundary condition in our column experiments, (ii) dispersivity of conservative solute is a third material property in addition to the more frequently investigated hydraulic functions, $\theta(h_m)$ and $K(h_m)$, of porous media, (iii) the NPs showed increased retardation when moving from close to saturation to unsaturated flow relative to tracer and (iv) the shapes of the breakthrough curves for both the citrate-coated and the soil-aged Ag NPs are substantially modified relative to tracer due to both physical and chemical interactions. Non-linearity in the dynamics of water flow is depicted in transport behaviour of the inert solute as a gently increase in dispersivity when moving from close to saturation towards unsaturated condition and a sudden kink at a threshold water content. Both chemical and shear forces are coupled during transport of the two forms of Ag NPs investigated. However, chemical forces dominate transport of the soil-aged Ag NPs whereas shear forces dominate transport of the citrate-coated NPs due to a more complex solution chemistry for the soil-aged Ag NPs. Both the citrate-coated and the soil-aged Ag NPs show reduced mobility at pH = 5 than at pH = 9. The convection-dispersion equation coupled with two terms for retardation and reaction could describe the observed breakthrough curves reasonably well. This form of parameterization is motivated by an extended Derjaguin-Landau-Verwey-Overbeek (eDLVO) analysis, that accounts for two parallel processes: (i) retardation at the air-water interface due

to reversible equilibrium interaction and (ii) straining at the solid–water interface due to irreversible sorption far from equilibrium. The eDLVO model satisfactorily explained the interaction of citrate–coated Ag NPs at both the air–water interface and the solid–water interface but could not fully apply to the soil–aged Ag NPs due to a complex solution chemistry and the limited validity of some chosen model parameters. Both forms of NPs were impacted by the physical flow field, thus, decreased transverse distance to the air–water interface and the solid–water interface and the formation of water films for unsaturated flow. An additional chemical interaction (cation bridging at the solid–water interface), which is irrelevant for the citrate–coated Ag NPs, was found to impact transport of the soil–aged Ag NPs. The mobility of engineered Ag NPs exposed to the environment may be limited by the ubiquitous presence of biogeochemical (organic and mineral) interfaces in addition to air–water interface and solid–water interface. Further studies would suffice to know how the eDLVO model could be improved to explain the proposed modeling concept.

Zusammenfassung

Transportprozesse in der ungesättigten Zone sind aufgrund ihrer komplexen und nichtlinearen Natur schwer zu untersuchen. Diese Komplexität ergibt sich unter anderem aus der dem Boden innewohnenden Heterogenität hinsichtlich biogeochemischer Grenzflächen und Feststoff–Wasser–Grenzflächen, sowie Luft–Wasser–Grenzflächen für ungesättigte Strömung. Diese Arbeit untersucht die folgenden Zusammenhänge: (i) Dispersivität in Abhängigkeit des Wassergehalts $\lambda(\theta)$, sowie (ii) Transportprozesse und Reaktivität von mit Citrat beschichteten und in natürlicher Bodenlösung "gealterten" Silber(Ag)–Nanopartikeln in Abhängigkeit von Wassergehalt. Es wird untersucht, wie sich die Nichtlinearität in der Strömungsdynamik auf das Transportverhalten sowohl des inerten gelösten Stoffes, als auch der beiden Formen von Ag–Nanopartikeln (mit Citrat beschichtet und im Boden gealtert) auswirkt. Die wichtigsten Ergebnisse der Studie sind: (i) Das Transportverhalten wird durch die Geometrie des Strömungsfeldes gesteuert, welche wiederum von Porenstruktur, Randbedingungen und Wassergehalt bei ungesättigter Strömung abhängig ist, (ii) die Dispersivität in Abhängigkeit des Wassergehalts $\lambda(\theta)$ wird als dritte Materialfunktion eines konservativen gelösten Stoffes in poröser Medien identifiziert, zusätzlich zu den viel untersuchten bodenhydraulischen Funktionen, $\theta(h_m)$ und $K(h_m)$, (iii) im Übergang von gesättigter zu ungesättigter Strömung tritt Retardierung von Nanopartikeln an Luft–Wasser–Grenzflächen als ein zusätzlicher Prozess beim Transport auf, (iv) Die Durchbruchkurven für Citrat–beschichtete und boden–gealterte Ag–Nanopartikel werden wesentlich verändert sowohl aufgrund physikalischer und als auch chemischer Wechselwirkungen an Grenzflächen. Die Retardierung von Nanopartikeln dabei aus einer Kombination eines dynamischen Gleichgewichtsprozesses an den Gas–Wasser Grenzflächen, während die chemische Sorption an die Fest–Wasser Grenzflächen als Ungleichgewichtsprozess betrachtet wird. Anders als im Fall von Citrat–beschichteten Teilchen konnte das erweiterte Derjaguin–Landau–Verwey–Overbeek Modell die Interaktionen bodengealterter Ag–Nanopartikel an der Feststoff–Wasser und Luft–Wasser–Grenzfläche nicht zufriedenstellend erklären. Eine zusätzliche chemische Wechselwirkung, nämlich Kationenbrücken an der Feststoff–Wasser–Grenzfläche, die für die Citrat–beschichteten Ag–Nanopartikel nicht von Bedeutung ist, wirkt sich im

Fall von bodengealterten Ag-Nanopartikeln deutlich aus. Ein Modell auf Grundlage der Konvektions-Dispersionsgleichung mit einem Retardations und einem Reaktionsterm konnte die experimentellen Durchbruchkurven recht gut modellieren. Die Ergebnisse deuten darauf hin, dass die Mobilität industriell hergestellter Ag-Nanopartikel unter natürlichen Freilandbedingungen durch die allgegenwärtige Präsenz biogeochemischer (sowie Gas-Wasser und Wasser-Festschubstanz) Grenzflächen stark herabgesetzt sein könnte.

Acknowledgements

Thanks are due to the German Research Foundation (Deutsche Forschungsgemeinschaft, DFG) for the financial support within the Research Group INTERNANO, the HIGRADE School of the Helmholtz Center for Environmental Research, UFZ–Leipzig/Halle for their support, Dr. Max Köhne (Department of Soil Physics, UFZ–Halle) for his technical support, and Prof. K.B. Laryea (Department of Soil Science, University of Ghana) for very insightful discussion on the section on solute transport. My thanks to the Department of Analytics at the UFZ–Leipzig especially Dr. H.-J. Stärk and Mr. Jürgen Steffen for conducting analyses of silver nanoparticles. I am grateful to Prof. Dr. Gabriele E. Schaumann and Dr. George Metreveli (University of Koblenz–Landau) for contributing significantly to discussion on the interaction of nanoparticles in porous media and the extended Derjaguin–Landau–Verwey–Overbeek model. I am also grateful to Dr. Sonda Klitzke for contributing to the ‘ageing’ of the nanoparticles. Thanks to the INTERNANO team for the very insightful discussions during project meetings and also to the Structure and function working group, Department of Soil Physics–Helmholtz Centre for Environmental Research, UFZ–Halle for providing a tolerant working atmosphere. Thanks to my friend Anja Heinz for her support. I am grateful to Tilly for her support and my utmost appreciation to Anty Esther for bringing me so far. Selikem, you arrived at a critical time–thanks for holding on. I am grateful to my family for their support and encouragement. Finally, to my supervisor Prof. Dr. Hans–Jörg Vogel–thanks for being an excellent coach.

Contents

Acknowledgements	v
List of Figures	ix
List of Tables	xiv
1 Introduction	1
1.1 Background and motivation	1
1.2 Thesis outline	2
1.3 A framework to investigate transport	3
1.4 Factors and processes	4
1.5 Objective and working hypothesis	5
2 Water flow and solute transport in unsaturated sand—a comprehensive experimental approach	6
2.1 Abstract	6
2.2 Introduction	7
2.3 Materials and Method	8
2.3.1 Unsaturated Solute Transport	8
2.3.2 Porous medium	9
2.3.3 Structure analysis	10
2.3.4 Multistep–Outflow, Multistep–Flux and Multistep–Transport Experimental Setup	10
2.3.4.1 Multistep–Outflow Experiment	11
2.3.4.2 Multistep–Flux Experiment	13
2.3.4.3 Multistep–Transport Experiment	13
2.4 Result and Discussion	14
2.4.1 Multistep–Outflow Approach	14
2.4.2 Multistep–Flux Approach	15
2.4.3 Multistep–Transport Approach	17
2.4.4 Consistency of Multistep–Outflow, Multistep–Flux and Multistep–Transport Approaches	19

2.4.5	Structure Analysis to Interpret Unsaturated Transport . . .	22
2.5	Conclusion	23
3	Transport of citrate-coated Ag nanoparticles in unsaturated sand	26
3.1	Abstract	26
3.2	Introduction	27
3.3	Materials and method	29
3.3.1	Silver nanoparticles	29
3.3.2	Sand medium	29
3.3.3	Water flow dynamics and transport experimental protocol .	30
3.3.4	Quantification of air-water-interfacial area	31
3.3.5	Hydrodynamic size, electro-kinetic characterization and in- terfacial potential energies	33
3.3.6	Analysis of breakthrough curves	33
3.3.6.1	Tracer BTCs	33
3.3.7	Model formulation: unsaturated transport of silver nanopar- ticles	34
3.3.8	Parameter estimation	35
3.4	Results and discussion	36
3.4.1	Size and colloidal stability of citrate-coated Ag nanoparticles	36
3.4.2	Consequence of silver nanoparticle hydrodynamic size and attachment properties on transport	36
3.4.3	Tracer and nanoparticle transport characteristics	38
3.4.3.1	Experimental breakthrough curves and modeling .	38
3.4.4	Influence of flow regime on transport	39
3.4.5	Effect of surface charge on transport	45
3.4.6	Retention profiles	45
3.5	Conclusion	46
4	Transport of soil-aged silver nanoparticles in unsaturated sand	47
4.1	Abstract	47
4.2	Introduction	48
4.3	Materials and methods	50
4.3.1	Aging of Ag nanoparticle in soil solution	50
4.3.2	Porous media and transport experiments	51
4.3.3	Characterization of the flow field	51
4.3.4	Characterization of pore-water chemistry	52
4.3.5	Hydrodynamic diameter, zeta potential and interfacial in- teraction energy	53
4.3.6	Model formulation	53
4.3.7	Parameter estimation	54
4.4	Results and discussion	55
4.4.1	Porous media properties and hydraulic state during transport	55
4.4.2	Properties of nanoparticles	55

4.4.3	Experimental breakthrough curves and soil-aged Ag nanoparticle transport	57
4.4.4	Retention profiles	58
4.4.5	Consequence of pore-water chemistry on transport	58
4.4.5.1	Dissolved organic carbon	63
4.4.5.2	Impact of multivalent cations and ionic strength	64
4.4.6	Extended DLVO energies and their controls on transport	65
4.5	Conclusion	67
5	Conclusions recommendations and outlook	68
5.1	Experimental concept	68
5.2	Major outcomes	69
5.3	Unsaturated transport framework	70
5.4	Outlook	72
A		74
B		79
Bibliography		86
		99

List of Figures

1.1	Porous media properties, boundary conditions and their interrelationships. NPs: nanoparticles, AWI: air–water interface; SWI: solid–water interface	2
1.2	Conceptual framework aimed at mechanistic understanding of unsaturated transport.	4
2.1	Pore (red) and solid (gray) structure of fine-grained quartz sand (grain diameter: 0.1–0.3 mm) obtained using high resolution X–ray computed tomography.	11
2.2	Multistep–outflow (MS–O), multistep–flux (MS–F), and multistep–transport (MS–T) experimental setup: tensiometers T1 and T2 (connected to KELLER PR41X sensors); pressure sensors Pc1 (control lower boundary pressure) and Pc2 (measures the water dynamics in the burette based on the difference to Pc1); magnetic valves Mv1 and Mv2 to control pressure at lower boundary. During MS–O experiment, V1 is opened to the burette only while V2 is closed. During MS–F, V1 is closed to the burette, V2 is opened to pressure tank, V3 is closed to the fraction collector and opened to the water reservoir (i.e., the water cycle is continuous for MS–F). During MS–T experiment (for input solution or tracer), V1 is closed to the burette, V2 is opened to pressure tank, and V3 is opened to the fraction collector. For MS–F and MS–T experiments, the control program adjusts Pc1 to the value measured by T1 (while T2 checks if a constant h_m is established within the entire column); balance 1 measured the volumetric water content while balance 2 checks the exact input flux during the MS–F and MS–T experiments.	12
2.3	Result obtained from multistep–outflow (MS–O) experiment for fine–grained quartz sand (grain diameter: 0.1–0.3 mm) indicating imposed pressure at the lower boundary of column (h_b) for drainage and imbibition, measured and modeled outflow, and pressure head (h_m).	15

2.4 (a) Hysteretic water retention characteristic obtained via inverse parameter optimization based on multistep–outflow (MS–O) and directly measured trajectories of state variables during multistepflux (MS–F) experiments. Also indicated are the measured water contents (θ_{MS-T}) during the transport experiment (pink dots) and the critical water content ($\theta_{critical}$) at which dispersivity increased abruptly (blue dot). The red arrow shows a fast adaption of h_m after a step change in boundary j_w (i.e., trajectory toward a non–equilibrium state) followed by a slow equilibration phase (i.e., trajectory toward some quasi–equilibrium state) indicated as the black arrow. (b) Hysteretic hydraulic conductivity function obtained via inverse parameter optimization based on MS–O (K_{MS-O}) and trajectories of $K-h_m$ directly measured during MS–F (K_{MS-F}). Also indicated are the measured hydraulic conductivity (K_{MS-T}) during the transport experiment (pink dots) and the critical hydraulic conductivity ($K_{critical}$) at which dispersivity increased abruptly (blue dot). The red arrow shows a fast adaption of h_m after a step change in boundary j_w (i.e., trajectory toward a non–equilibrium state) followed by a slow equilibration phase (i.e., trajectory toward some quasi–equilibrium state) indicated as the black arrow. 16

2.5 (a) Dynamics of pressure head (h_m) and volumetric water content (θ) during stepwise decrease (drainage) in infiltration rate (j_w) during multistep–flux (MS–F) and (b) for increasing infiltration steps. h_b , h_{ml} , and h_{mu} are lower boundary pressure (Pc1), upper (T1), and lower (T2) pressure heads within the column. 18

2.6 Breakthrough curves for various flow rates as normalized flux concentration versus infiltrated pore volume. 20

2.7 Validation of the multistep–transport (MS–T) approach for average pore–water velocity, v [i.e., obtained using CXTFIT (v_{CXTFIT}) versus measured directly (v_{MS-T})]. 21

2.8 Optimized dispersivity (λ) using CXTFIT as a function of water content (θ) (the insert figure is a plot of θ and pore–water velocity, v versus λ) 21

2.9 The fraction of isolated water clusters versus water content (θ) derived from cluster analysis of a three–dimensional image obtained from X–ray computed tomography 24

2.10 (a) Distribution of air (red), solid (gray) and water [i.e., continuous (blue) and isolated (green) water clusters at $\theta = 0.11$ based on a three–dimensional image obtained from X-ray computed tomography. (b) Distribution of percolating (blue) and isolated (green) water clusters at $\theta = 0.11$ based on a three–dimensional image obtained from X–ray computed tomography. 24

3.1	Multistep–outflow (MS–O), multistep–flux (MS–F) and multistep–transport (MS–T) experimental setup (Figure after Kumahor et al. [50]). The citrate–coated Ag nanoparticle (NP) transport experiment uses the MS–T setup but for a specified flow rate at the top boundary and outflow collected in fractions.	31
3.2	Experimental conditions during citrate–coated Ag NP transport (from top to bottom: increasing flow rate, j_w ; from left to right: increasing pH). In the legend, h_{mu} , h_{ml} and h_b are upper, lower and boundary pressure heads respectively.	32
3.3	Dimensionless DLVO (a) and extended DLVO (b) interaction energy profiles for citrate–coated Ag NPs versus solid–water interface (SWI) and air–water interface (AWI) at pH = 5 and pH = 9. The extended DLVO profiles account for hydrophobic interactions. The insert Figures in (a) and (b) represent a section of the interaction energy profiles in order to visualize the absence or presence of secondary minimum.	38
3.4	Equilibrium sorption coefficient (K_{eq}) as a function of area of the air–water interface (AWI).	41
3.5	Experiment breakthrough curves, BTCs (a) and retention profiles, RP (b) for citrate–coated Ag nanoparticles, NPs ($j_w = 2.4 \text{ cm h}^{-1}$; pH = 5 and pH = 9). The symbols and lines represent experimental outcomes and model results respectively. The result of tracer experiment [50] are shown in black symbols (experiment) and line (model result) for $j_w = 2.4 \text{ cm h}^{-1}$. The dispersion coefficient, $D_{eff} = 14.15 \text{ cm}^2 \text{ h}^{-1}$ for $j_w = 2.4 \text{ cm h}^{-1}$, of the tracer experiment was fixed for NP parameter estimation. The inset Figure zooms in on the shape of NP BTCs.	42
3.6	Experiment breakthrough curves, BTCs (a) and retention profiles, RP (b) for citrate–coated Ag nanoparticles, NPs ($j_w = 9.7 \text{ cm h}^{-1}$; pH = 5 and pH = 9). The symbols and lines represent experimental outcomes and model results respectively. The result of tracer experiment [50] is shown in black symbols (experiment) and line (model result) for $j_w = 9.7 \text{ cm h}^{-1}$. The dispersion coefficient, $D_{eff} = 6.95 \text{ cm}^2 \text{ h}^{-1}$ for $j_w = 9.7 \text{ cm h}^{-1}$, of the tracer experiment was fixed for NP parameter estimation.	43
3.7	Experiment breakthrough curves, BTCs (a) and retention profiles, RP (b) for citrate–coated Ag nanoparticles, NPs ($j_w = 17 \text{ cm h}^{-1}$; pH = 5 and pH = 9). The symbols and lines represent experimental outcomes and model results respectively. The result of tracer experiment [50] is shown in black symbols (experiment) and line (model result) for $j_w = 17 \text{ cm h}^{-1}$. The dispersion coefficient, $D_{eff} = 6.48 \text{ cm}^2 \text{ h}^{-1}$ for $j_w = 17 \text{ cm h}^{-1}$, of the tracer experiment was fixed for NP parameter estimation.	44

- 4.1 Dissolved organic carbon (OC) content, concentration of Ca^{2+} and Mg^{2+} and ionic strength measured in column eluate sampled between the 7th and 8th pore volume (PV). The horizontal line (in black) indicates 1 mM KNO_3 solution used as electrolyte for the citrate-coated Ag NPs transport experiments. The labels of x-axis are described in Table 4.1. 56
- 4.2 Experiment breakthrough curves, BTCs (a) and retention profiles, RPs (b) for soil-aged Ag nanoparticles, NP ($j_w = 2.7 \text{ cm h}^{-1}$ at pH = 5 and $j_w = 2.4 \text{ cm h}^{-1}$ at pH = 9). The symbols and lines represent experiment and model results respectively. The BTCs for soil-aged (this study) and citrate-coated Ag NPs [51] are compared. The results of the tracer experiment [50] are shown in black symbols (experiment) and line (model result) for $j_w = 2.4 \text{ cm h}^{-1}$. The dispersion coefficient, $D_{eff} = 14.15 \text{ cm}^2 \text{ h}^{-1}$ for $j_w = 2.4 \text{ cm h}^{-1}$, of the tracer experiment was fixed during parameter estimation for the soil-aged Ag NPs. 59
- 4.3 Experiment breakthrough curves, BTCs (a) and retention profiles, RPs (b) for soil-aged Ag nanoparticles, NP ($j_w = 9.7 \text{ cm h}^{-1}$; pH = 5 and pH = 9). The symbols and lines represent experiment and model results respectively. The BTCs for soil-aged (this study) and citrate-coated Ag NPs [51] are compared. The results of the tracer experiment [50] are shown in black symbols (experiment) and line (model result) for $j_w = 9.7 \text{ cm h}^{-1}$. The dispersion coefficient, $D_{eff} = 6.95 \text{ cm}^2 \text{ h}^{-1}$ for $j_w = 9.7 \text{ cm h}^{-1}$, of the tracer experiment was fixed during parameter estimation for the soil-aged Ag NPs. 60
- 4.4 Experiment breakthrough curves, BTCs (a) and retention profiles, RPs (b) for soil-aged Ag nanoparticles, NPs ($j_w = 17 \text{ cm h}^{-1}$; pH = 5 and pH = 9). The symbols and lines represent experiment and model results respectively. The BTCs for soil-aged (this study) and citrate-coated Ag NPs [51] are compared. The results of the tracer experiment [50] are shown in black symbols (experiment) and line (model result) for $j_w = 17 \text{ cm h}^{-1}$. The dispersion coefficient, $D_{eff} = 6.48 \text{ cm}^2 \text{ h}^{-1}$ for $j_w = 17 \text{ cm h}^{-1}$, of the tracer experiment was fixed during parameter estimation for the soil-aged Ag NPs. The data (BTCs and RPs) for citrate-coated Ag NPs at $j_w = 17 \text{ cm h}^{-1}$ and pH = 5 were reoptimized by allowing flexibility in fitting $S_{np,max}$. 61
- 4.5 Equilibrium sorption coefficient (K_{eq}) of soil-aged Ag NPs versus area of the air-water interface (AWI). The red and blue points (data) and line (trend) refer to citrate-coated (Kumahor et al. [51]) and soil-aged Ag NPs (this study) respectively. The data (BTCs and RPs) for the citrate-coated Ag NPs at $j_w = 17 \text{ cm h}^{-1}$ and pH = 5 (refer to key) were reoptimized by allowing flexibility in fitting $S_{np,max}$ (represented as cross). 63

- 4.6 Dimensionless extended Derjaguin–Landau–Verwey–Overbeek (eDLVO) interaction energy profiles for soil–aged Ag NPs versus air–water interface (top Figures) and solid–water interface (bottom Figures) at pH = 5 (Exp1, Exp3, Exp5) and pH = 9 (Exp2, Exp4, Exp6). The eDLVO profiles account for hydrophobic interaction in addition to van der Waals and electrical double layer interactions. 66
- A.1 (a) Hydrodynamic diameter (h_d) of citrate-coated Ag nanoparticles (NPs) as a function of pH. The dispersion pH was adjusted in the range from neutral (pH = 7) to basic (pH = 11) using NaOH (black) while in the acidic (pH 2 to 6) range using either HNO₃ (red) or H₂SO₄ (blue). The average h_d value was calculated from 6 values obtained from 2 measurements (thus each measurement is repeated three times) (b) Zeta (ζ) potential of citrate-coated Ag NPs as a function of pH. The dispersion pH was adjusted in the range from neutral (pH = 7) to basic (pH = 11) using NaOH (black) while in the acidic range (pH = 2 to 6) using either HNO₃ (red) or H₂SO₄ (blue). The average ζ potential value was calculated from 6 values obtained from 2 measurements (thus each measurement is repeated three times). 78
- B.1 Hydraulic states during transport. The parameters h_{mu} , h_{ml} and h_b , represent lower, upper and boundary pressure heads respectively while θ , and j_w are water content and flow rate respectively. Considering a bulk density (ρ_b) of 1.52 g cm⁻³ and a particle density (ρ_s) of 2.65 g cm⁻³ for mineral soils, the total porosity is calculated to be 0.42 (volume basis). 83
- B.2 Pressure head (red) and size distribution (green) of pores versus volume fraction of pores derived from X–ray computer tomography (CT) images and pore structure analysis. The figure was obtained at a state of energetic minimum assuming spherical air–water interfaces and complete wettability of the pore surfaces using the Young–Laplace Equation. 84

List of Tables

2.1	Optimal parameters obtained from inverse modeling of multistep-outflow (MS-O) water content (θ) and pressure head (h_m) dynamics for fine-grained quartz sand (0.1–0.3 mm grain diameter): θ_r and θ_s are residual and saturated water contents, α_i and θ_d , scaling factors for imbibition and drainage, and n , τ , and K_s are shape parameter, tortuosity factor, and saturated hydraulic conductivity, respectively.	15
2.2	Transport parameters obtained by multistep-transport (MS-T) approach: flux rate (j_w), measured volumetric water content (θ_{MS-T}), directly measured mean pore-water velocity, v_{MS-T} ($= j_w/\theta_{MS-T}$), optimized mean pore-water velocity using CXTFIT (v_{CXTFIT}), effective mean velocity, effective dispersion coefficient (D_{eff}), dispersivity (λ), molecular diffusion coefficient (D_m), measured pressure head (h_m), macroscopic peclet number (Pe), and coefficient of determination (r^2).	20
3.1	Model parameters obtained from 1-D convection-dispersion and reaction model for citrate-coated Ag NPs and calculated mass balance from NP transport experiments; the model accounts for time and depth straining. The parameters j_w , v , β , $S_{np,max}/C_o$, k_{att} , k_{det} and R are flow rate, pore-water velocity, shape factor, normalized maximal attainable amount of NPs attached, attachment coefficient, detachment coefficient, and retardation factor respectively. The mass of NPs adsorbed and mobilized through the column is expressed as fraction of the total applied mass [%]. The experiment conducted at pH = 5 and $j_w = 2.4 \text{ cm h}^{-1}$ could not be fitted due to almost complete retention within the column.	40
4.1	Description of the soil-aged Ag NPs transport experiments conducted at the various flow rates (j_w) corresponding to the measured water contents (θ) and pH values. The experiments, Exp1 and Exp2, have slightly different flow rates and this could be captured because the specified (based on pump calibration) and actual (obtained from balance reading) flow rates were monitored.	52
4.2	Properties of soil-aged Ag nanoparticles versus citrate-coated Ag nanoparticles.	56

4.3	Parameters obtained from a 1-D convection dispersion and reaction model for the soil-aged Ag NPs compared with parameter estimates for that of the citrate-coated Ag NPs (in parenthesis; obtained from Kumahor et al., [51]). The model concept accounts for retardation at the air-water interface (AWI) as well as time and depth dependent retention at the solid-water interface (SWI). Due to almost complete retention within the column, the experiment conducted at $j_w = 2.7 \text{ cm h}^{-1}$ at $\text{pH} = 5$ could not be modeled.	62
A.1	Input parameters and physical constants used for the calculation of the total interaction energy between nanoparticles and collector. . .	77
B.1	Input parameters and physical constants used for the calculation of the total interaction energy between nanoparticles and collector. . .	82
B.2	Major constituents in eluate collected between the 7 th and 8 th pore volume. Addition of HNO_3 to adjust pH elevated NO_3^- concentration at $\text{pH} = 5$	85

In memory of my father Sylvanus Mensah Kumahor

Chapter 1

Introduction

1.1 Background and motivation

The unsaturated zone is a vertical transition from land to phreatic surface. It is a filter, a reactor and a cushion for groundwater among other functions, however, these functions critically depend on some inherent properties. Nanoparticles are among a variety of substances considered as emerging contaminants [74] in the environment. Synthesis and use of nanoparticles may result in elevated concentration in contrast to natural background concentration and therefore calls for risk assessment in terms of their long-term mobility. Since the engineered forms may differ from their natural counterparts, the ability to predict the fate of engineered nanoparticles in the vadose zone would be required for decision making within the spheres of politics, science and engineering. The capabilities of the unsaturated zone to attenuate migration of nanoparticles therefore needs to be evaluated against external factors (Fig. 1.1). For instance, re-exposure of engineered nanoparticles into soils after use requires detailed enquiry with respect to: (1) their engineered versus altered (i.e., after re-exposure to the environment) properties, (2) the properties of the unsaturated porous media in relation to their mobility and (3) the impact of both chemical and physical (hydrologic) factors on their mobility. Additionally, the thermodynamic basis of retention of nanoparticles at the microscopic scale for unsaturated flow needs to be adequately reconciled with transport phenomena observed at the column scale. This would pave the way for a more robust mathematical formulation to model and predict transport.

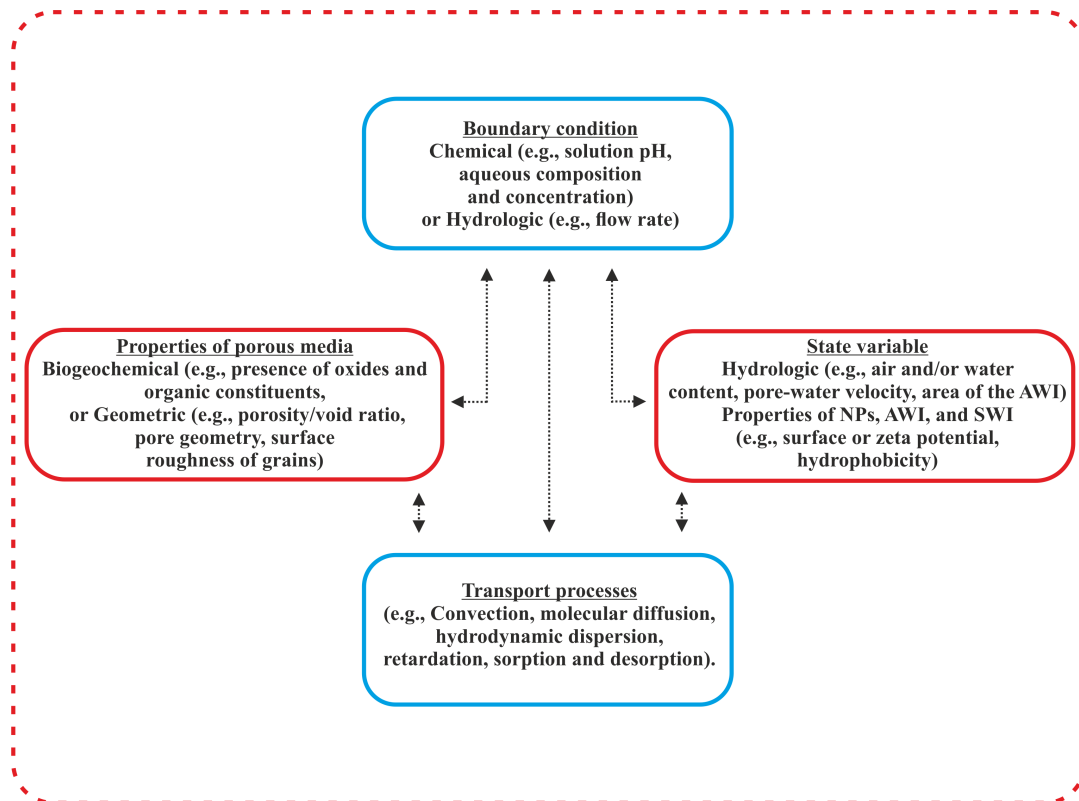


FIGURE 1.1: Porous media properties, boundary conditions and their inter-relationships. NPs: nanoparticles, AWI: air–water interface; SWI: solid–water interface

1.2 Thesis outline

This thesis is organized into five main chapters. The remaining part of this chapter discusses: (i) methodological approaches available to investigate unsaturated transport in porous media in an integrated manner, (ii) factors that are typically considered for mechanistic understanding and (iii) additional aspects that may enhance our predictive capabilities of fate and transport of nanoparticles in the environment. Lastly, the overarching objectives and working hypotheses of this study are outlined.

Chapter 2: (i) reviews relevant knowledge on tracer transport for unsaturated flow, (ii) adopts recent developments in the measurement of unsaturated hydraulic properties to investigate unsaturated water dynamics and transport of tracer (KBr) and (iii) demonstrates how X–ray computed tomography (CT) measurements and morphological analysis provide additional aspects to explain transport. The knowledge gained from this enquiry forms a basis of designing transport experiments for nanoparticles.

Chapter 3: (i) extends the knowledge gained from tracer transport for unsaturated flow (Chapter 2) to a more complex case of transport of citrate-coated Ag nanoparticles in unsaturated sand with KNO_3 as background electrolyte, (ii) relates the retention of nanoparticles to occurrence of air–water interface (AWI) in addition to solid–water interface (SWI) and (iii) adopts the classical DLVO (Derjaguin–Landau–Verwey–Overbeek) (i.e., electrostatic and van der Waals interactions) and extended DLVO (eDLVO) models (i.e., DLVO plus hydrophobic interaction) to explain local interaction of nanoparticles.

Chapter 4: (i) compares the mobility of soil-aged Ag nanoparticles in unsaturated sand with the mobility of citrate-coated Ag nanoparticles with focus on how potential transformation of particle properties upon re-exposure to the environment may alter mobility and (ii) explores in how far the eDLVO model could explain the local interaction when moving from relatively simple case of KNO_3 as background electrolyte, the case of the citrate-coated Ag nanoparticles, to soil solution.

Chapter 5: draws on the major conclusions thereof and aspects that require further enquiry.

1.3 A framework to investigate transport

Figure 1.2 integrates some methodological approaches that are useful to investigate unsaturated transport. For saturated systems, the mobility of engineered nanoparticles in porous media has been investigated typically by combining breakthrough curves (BTCs) for both tracer and nanoparticles [59, 60] with the DLVO [32] and/or eDLVO models [68]. For unsaturated flow, changes in flow geometry due to changing flux boundary condition and pore structure demands an initial step of characterizing hydraulic property, $\theta(h_m)$ and $K(h_m)$, of the porous media (Fig. 1.2) in question before conducting transport experiments. Well characterized hydraulic property prescribes a priori boundary conditions for transport. Hydraulic characteristics are further required to explain the impact of hydrologic regime on transport. This study also reconciles the local geometry of the flow field, by means of X-ray computed tomography (CT) and morphological analysis [102], with the measured hydraulic properties to explain transport. The DLVO and eDLVO models further complements the convection–dispersion (CD) and reaction model to explain the observed transport behaviour of the nanoparticles.

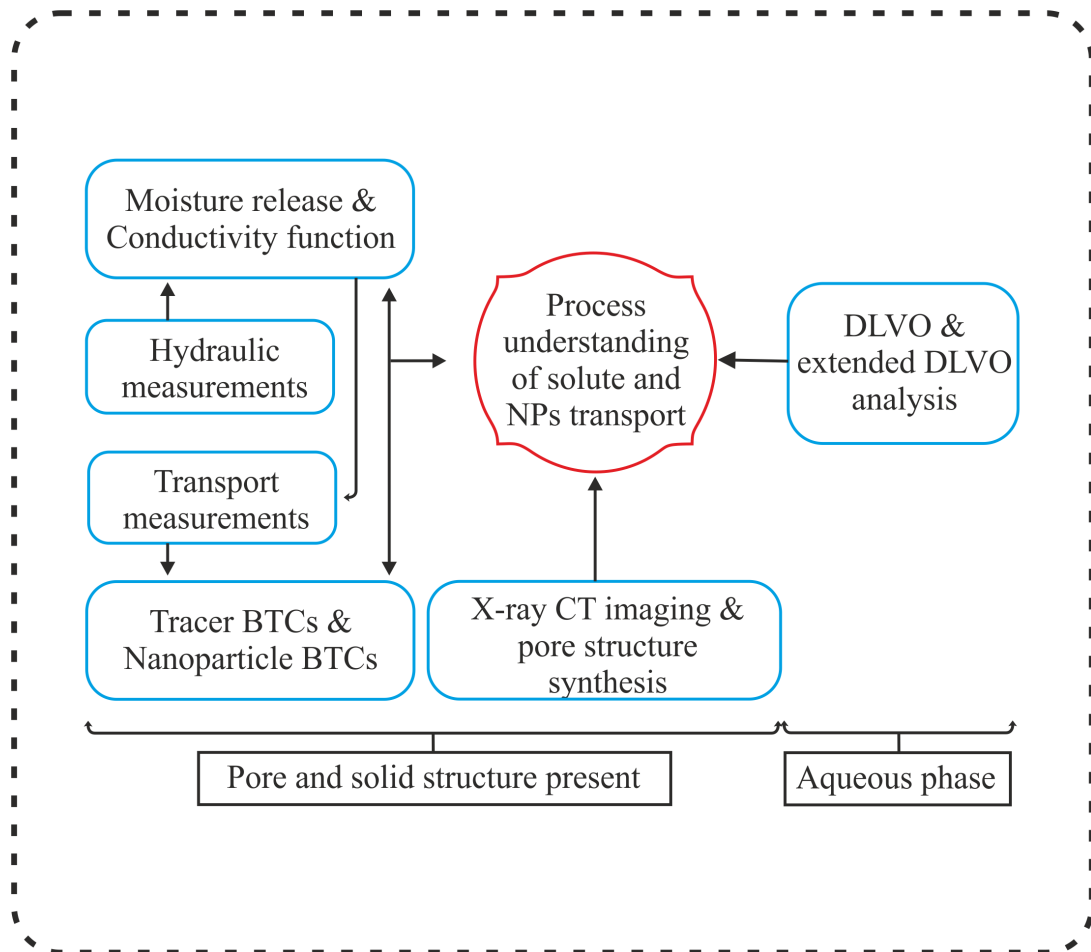


FIGURE 1.2: Conceptual framework aimed at mechanistic understanding of unsaturated transport.

1.4 Factors and processes

Figure 1.1 outlines typical facets to consider when investigating transport in porous media. Column experiments aimed at measuring the mobility of nanoparticles generally consider: (i) solution chemistry (e.g., pH, ionic strength, composition of solution), (ii) properties of nanoparticles (e.g., stability, surface potential, hydrodynamic size) (iii) biogeochemical composition of porous media (e.g., presence of clay minerals, oxides or organic matter) (iv) geometrical properties of porous media (e.g., grain size, surface roughness) (v) hydrologic conditions (e.g., flow rate j_w , water content θ and pore-water velocity v). Schaumann et al. [76] discussed these factors and their related processes in detail. These factors have been mostly studied for saturated systems and need to be re-visited for unsaturated flow. Broadly, interaction of solutes and/or nanoparticles in porous media are a result of both the properties of porous media and boundary conditions. Porous

media properties can be classified as geometric (e.g., pore structure, porosity and void ratio, mineral/solid surface roughness) or biogeochemical (presence of organics and reactive minerals). Boundary conditions can also be chemical (e.g., pH, solution composition) or hydrologic (e.g., j_w , θ and v).

In this thesis, key chemical factors such as pH, ionic and/or biogeochemical composition were investigated in conjunction with hydrologic states, thus j_w , θ and v for a simplified porous medium (i.e., organics and reactive minerals are excluded as much as possible). This study further attempts to establish the linkages between transport versus state variables such as j_w , θ and v , structure of pores and the geometry of the flow field in response to flux boundary conditions, solution chemistry (pH, ionic and/or dissolved organic matter), chemical potential energy of the interfaces formed for unsaturated flow and the reactivity of nanoparticles.

1.5 Objective and working hypothesis

The overarching objectives of this thesis are to:

- i. experimentally investigate the mobility of engineered nanoparticles in porous media based on: (a) properties of nanoparticles, (b) pore structure, and (c) hydraulic state, and
- ii. numerically evaluate the mobility of engineered nanoparticles to obtain a mechanistic understanding of particle retention.

We hypothesize that:

- i. transition from saturated to unsaturated flow leads to an additional process for particle retention,
- ii. mobilization of nanoparticles is triggered by the feedback between local retention of nanoparticles governed by chemical forces and the velocity field, and
- iii. recognizing these relevant processes provide a framework to predict transport of engineered nanoparticles based on: (a) properties of nanoparticles (b) pore structure and (c) hydraulic states during transport.

Chapter 2

Water flow and solute transport in unsaturated sand—a comprehensive experimental approach

2.1 Abstract

Water flow and solute transport in unsaturated porous media are affected by the highly non-linear material properties and non-equilibrium effects. This makes experimental procedures and modeling of water flow and solute transport challenging. In this study, we present an extension to the well known multistep-outflow (MS-O) and the newly introduced multistep-flux (MS-F) approaches to measure solute dispersivity as a function of water content under well-defined conditions (i.e., constant pressure head and uniform water content). The new approach is termed multistep-transport (MS-T) and complements the MS-O and MS-F approaches. Our setup allows for applying all three approaches in a single experimental setting. Hence, it provides a comprehensive data set to parameterize unsaturated flow and transport processes in a consistent way. We demonstrate this combined approach (MS-OFT) for sand (grain diameter: 0.1–0.3 mm) and

This chapter has been published: Kumahor, S.K., de Rooij, G.H., Schlüter, S. and Vogel H.-J. 2015. Water flow and solute transport in unsaturated sand—a comprehensive experimental approach. Soil Science Society of America. Vadose Zone J. doi:10.2136/vzj2014.08.0105.

complemented the experimental results with an analysis of the underlying pore structure using X-ray computed tomography (CT). The results show that dispersivity is a non-linear function of water content, and a critical water content (≈ 0.2) exists at which dispersivity increased significantly. The results could be explained by marked change in the geometry of the flow field as derived from X-ray CT measurements. It is characterized by a reduced connectivity of the water phase. The results demonstrate the potential of a combined approach linking pore structure, hydraulic functions, and transport characteristic.

Abbreviations: BTC, breakthrough curve; CD, convection–dispersion; CT, computed tomography; EC, electrical conductivity; MS–F, multistep–flux; MS–O, multistep–outflow; MS–OFT, multistep–outflow–flux–transport; MS–T, multistep–transport.

2.2 Introduction

The investigation of solute transport during unsaturated water flow in soil is challenging. This is because soil hydraulic properties (i.e., moisture characteristic and hydraulic conductivity function) are non-linear and a well-defined equilibrium between water content θ [–] and pressure head h_m [L] can hardly be achieved. This is observed for both natural soils in the field and experimental conditions in the laboratory. Early work of Topp et al. [86] and Vachaud et al. [94] already demonstrated the nonuniqueness of soil hydraulic characteristics. The observed phenomena can ultimately be explained by the structural heterogeneity of the underlying pore network. While there is a considerable body of literature on soil hydraulic characteristics (see [25] for a recent review), the impact of changing θ on solute transport still requires further attention. For instance, to establish the functional relationship between θ and macroscopic dispersivity λ [L], requires systematic experiments with well-defined hydraulic state variables. This deficit in knowledge might be caused by the experimental difficulties to explore unsaturated solute transport under well-defined conditions.

A common experimental approach to measure soil hydraulic properties is the multistep–outflow (MS–O) approach [36, 95, 117], which has been shown to also provide valuable information on hydraulic non–equilibrium [26]. This method has

recently been extended to a multistep–flux (MS–F) approach for direct measurement of unsaturated hydraulic conductivity including hydraulic non–equilibrium effects [108, 109]. The MS–F approach is based on establishing gravity flow at a series of well–defined h_m and θ values, and, thus, it should also be an ideal setup for measuring solute breakthrough curves (BTCs) to quantify transport properties. In this paper, we extended the MS–O and the MS–F approaches with a multistep–transport (MS–T) approach that measures BTCs at constant h_m and uniform θ for different flow rates. This provides a combined tool (MS–OFT) implemented in a single experimental setup to arrive at a more complete picture of water dynamics and solute transport properties of porous media including their interrelation. We demonstrated the MS–OFT approach for a sand sample with the focus on transport of inert solutes as the new component. This experimental approach was complemented by an analysis of the pore structure using X–ray CT images, which allowed us to explain the dependency of measured λ on θ .

2.3 Materials and Method

2.3.1 Unsaturated Solute Transport

The classical way of modeling transport of conservative solutes in porous media is the convection–dispersion (CD) model:

$$\frac{\partial \theta C}{\partial t} = \theta D_{eff} \frac{\partial^2 C}{\partial z^2} - j_w \frac{\partial C}{\partial z} \quad (2.1)$$

where j_w [LT^{-1}] is flow rate, D_{eff} [L^2T^{-1}] is effective dispersion coefficient, C [ML^{-3}] is solute concentration, z [L] is travel distance and t [T] is time. The CD model is justified in the case when transport distance is much larger than some characteristic length of small–scale heterogeneity. Then, D_{eff} is a combined effect of molecular diffusion, D_m [L^2T^{-1}] and hydrodynamic dispersion, D_h [L^2T^{-1}], due to pore–scale variability of velocities obeying a Fickian regime. Small–scale heterogeneity within the flow field is expressed as dispersivity λ ($= D_{eff}/v$; where v [LT^{-1}] is pore–water velocity) [L], which can be interpreted as a characteristic length of heterogeneity within the flow field. Since the structure of the flow field depends on θ , we consider $\lambda(\theta)$ to be another material property related to

solute transport. It has been shown that λ is scale dependent [23, 33] owing to the fact that terrestrial systems are hierarchically structured at any scale. This, however, is not considered in this paper. We focus on the measurement of $\lambda(\theta)$ for a macroscopically homogeneous media without any hierarchy in scale, such that λ is expected to be merely a function of θ .

Under field conditions, both j_w and gradient in h_m respond to external forcing, thereby satisfying the Darcy–Buckingham law. A decrease in j_w and a corresponding decrease in θ may not necessarily invoke a decrease in v ($=j_w/\theta$). However, decrease in θ deactivates large pores, increases tortuosity of flow paths, prolongs solute residence time, and impedes solute mixing such that v is actually expected to decrease (e.g., [87]). On this premise, we note that there are some contrasting views about $\lambda(\theta)$. For example, some studies reported higher λ for lower θ (e.g., [24, 61, 62, 67]), and this was conceptually attributed to the presence of immobile water (e.g., [24, 34]). In such cases, experimental data could be evaluated using the mobile–immobile (MIM) model (e.g., [24, 34]). Generally, packed sediments are typical of increased λ when θ is decreased (e.g., [34]). In contrast, a lower λ value for lower j_w was attributed to deactivation of large pores due to decreased θ (e.g., [97]). Toride et al. [87] observed maximum λ at intermediate θ during unit gradient flow. Using a multidirectional pore network model, Raouf and Hassanizadeh [71] obtained a maximum for λ occurring at a critical saturation. Considering this ambiguity, a standard procedure to directly measure $\lambda(\theta)$ as a third material property besides $h_m(\theta)$ and $K(\theta)$ would be helpful. The experimental setup described in the following is designed to measure all three material properties in a single experimental setting.

2.3.2 Porous medium

Fine-grained quartz sand (grain diameter: 0.1–0.3 mm) was repacked in a polyvinyl chloride cylinder (16.2-cm diam. and 10.0-cm height). The column was tapped gently at the sides during packing to establish a uniform bulk density, ρ_b [ML^{-3}] ($= 1.52 \text{ g cm}^{-3}$) throughout the entire column. This column was used for the entire series of hydraulic (MS–O and MS–F) and solute transport (MS–T) experiments.

2.3.3 Structure analysis

We obtained a three-dimensional image (Fig. 2.1) of the fine-grained quartz sand from a sample with the same ρ_b ($= 1.52 \text{ g cm}^{-3}$) as the experimental column using an industrial X-ray CT scanner (X-Tek HMX 225). The image was acquired at an energy level of 90 kV and 612 μA with a resultant voxel size of 0.014 mm. The three-dimensional image was processed according to the following steps: (i) increase of image dimensions using trilinear interpolation, (ii) image denoising using median filter (e.g., [78]), (iii) threshold detection using gradient mask [78, 79] and (iv) hysteresis thresholding [78, 100] using the two thresholds detected by gradient masking. In this way, the image was segmented into pore and solid. After segmentation, the pore structure was analyzed using standard procedures in mathematical morphology to quantify the pores size distribution [102]. Based on this pore size distribution, we calculated the spatial distribution of air and water within the porous media at different pressure heads [35, 99]. This approach is based on the simplifying assumptions that the interface between air and water is spherical and that its curvature is related to h_m in accordance with the Young-Laplace equation for complete wettability (i.e., the contact angle is assumed to be zero). The phase distribution obtained in this way is an approximation of the phase distribution at minimum energy, which is hardly achieved in reality due to non-equilibrium effects. Nonetheless, it may serve as valuable information to estimate the connectivity of the water phase at various water contents, which we expect would be useful for the interpretation of unsaturated water flow and solute transport. This connectivity is quantified by counting the number of separated clusters of water at different degrees of water saturation using the algorithm of Hoshen and Kopelman [37].

2.3.4 Multistep-Outflow, Multistep-Flux and Multistep-Transport Experimental Setup

The device for all three types of experiments is shown in Fig. 3.1. The column was placed on a porous sintered glass plate. The glass plate was covered with a nylon diaphragm of -250 hPa air-entry value and equipped with a pressure sensor (KELLER, PR41X) to monitor h_m at the lower boundary of the column (Pc1). This pressure was controlled by two magnetic valves, Mv1 and Mv2, connected to

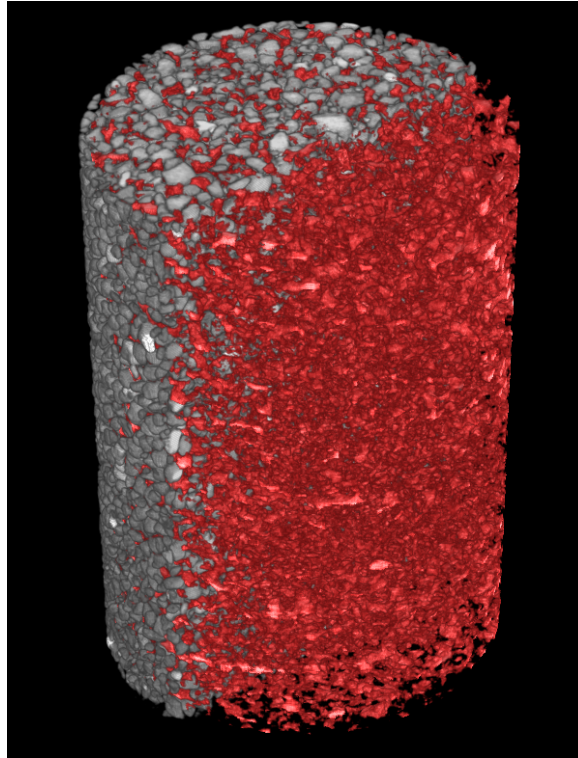


FIGURE 2.1: Pore (red) and solid (gray) structure of fine-grained quartz sand (grain diameter: 0.1–0.3 mm) obtained using high resolution X-ray computed tomography.

atmosphere and a pressure reservoir, respectively. Two tensiometers measured h_m close to the top of the column (T1) and within the column (T2).

2.3.4.1 Multistep–Outflow Experiment

For the MS–O experiment, the amount of outflow across the lower boundary versus h_m within the column was monitored following a prescribed protocol. The MS–O dynamics are such that the initially water–saturated sand column is subjected to stepwise drainage and imbibition following the same course of pressure steps for decreasing and increasing pressure heads. One such drainage–imbibition cycle was performed for capillary saturation of the sample to establish the initial conditions for the second cycle, which was finally evaluated. Dynamics of θ within the sample and the corresponding h_m during drainage and imbibition were measured at high temporal resolution (seconds). The lower limit of drainage for the MS–O experiment was -60 cm when outflow ceased. Based on the measured dynamics of water flow and h_m , the hydraulic characteristics $h_m(\theta)$ and $K(\theta)$ were obtained using a classical van Genuchten model [96] and a modified dependent domain model [66]

to include hysteresis. This resulted in two shape parameters for drying and wetting. Parameter estimation was based on an inverse solution of Richards equation using the software package MuPhi [42].

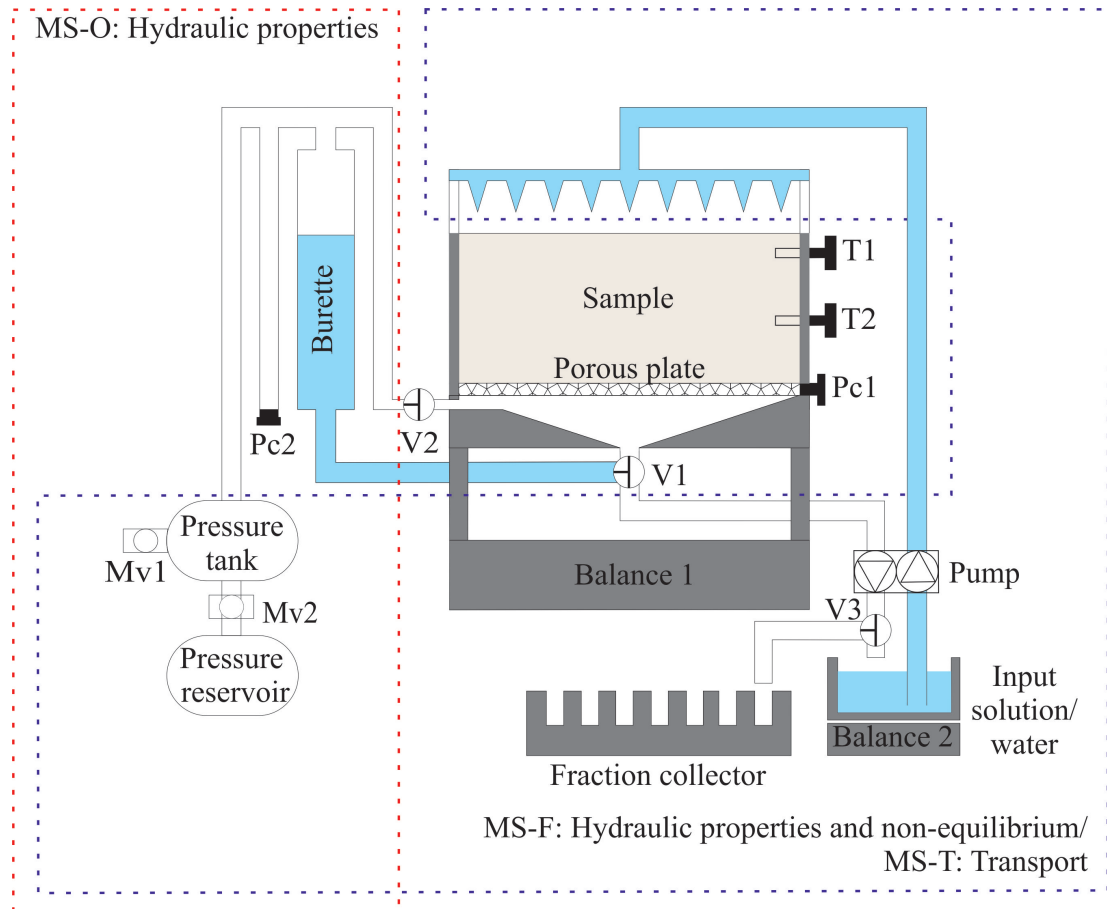


FIGURE 2.2: Multistep-outflow (MS-O), multistep-flux (MS-F), and multistep-transport (MS-T) experimental setup: tensiometers T1 and T2 (connected to KELLER PR41X sensors); pressure sensors Pc1 (control lower boundary pressure) and Pc2 (measures the water dynamics in the burette based on the difference to Pc1); magnetic valves Mv1 and Mv2 to control pressure at lower boundary. During MS-O experiment, V1 is opened to the burette only while V2 is closed. During MS-F, V1 is closed to the burette, V2 is opened to pressure tank, V3 is closed to the fraction collector and opened to the water reservoir (i.e., the water cycle is continuous for MS-F). During MS-T experiment (for input solution or tracer), V1 is closed to the burette, V2 is opened to pressure tank, and V3 is opened to the fraction collector. For MS-F and MS-T experiments, the control program adjusts Pc1 to the value measured by T1 (while T2 checks if a constant h_m is established within the entire column); balance 1 measured the volumetric water content while balance 2 checks the exact input flux during the MS-F and MS-T experiments.

2.3.4.2 Multistep–Flux Experiment

The basic idea of the MS–F experiment is to harmonize h_m at the lower boundary (PC1) with that close to the upper surface of the sample (T1) while a constant j_w is applied using a peristaltic pump (Fig. 3.1). Water was infiltrated via 19 hypodermic needles uniformly distributed over the column surface, and hence, we assume uniformity in the surface flux density. In this way, a constant h_m and a uniform θ were established for a series of different j_w values. The resulting gravity flow conditions are given by:

$$j_w = -K \left(\frac{\partial h_m}{\partial z} + 1 \right) \quad (2.2)$$

where $\partial h_m / \partial z = 0$ and z is the vertical coordinate (positive upward). Thus, the absolute value of j_w corresponds to the hydraulic conductivity, K [LT^{-1}] at the given h_m . The MS–F setup was equipped with a balance (Mettler Toledo PBA Series) to measure the mass of the column at high temporal resolution (seconds). This allowed for deriving the differences in θ for the various flow rates. The water content is assumed to be constant throughout the depth of the column. Thus, with a complete cycle of drainage (decreasing flux steps) and imbibition (increasing flux steps), the MS–F approach provides a direct measure of K , h_m , and θ . The second tensiometer (T2) monitors h_m within the column as a check for consistency in hydraulic states during both the MS–O and the MS–F experiments. The initial condition for the start of the MS–F experiment was the end of the imbibition cycle of the MS–O experiment. For more details on the MS–F experiments we refer to Weller et al. [108] and Weller and Vogel [109].

2.3.4.3 Multistep–Transport Experiment

The new MS–T approach is based on the same concept as the MS–F approach, that is the establishment of gravity flow conditions for different j_w by adjusting the h_m at the lower boundary to that measured close to the surface. In this way, the vertical profile of hydraulic state variables h_m and θ were uniform for different flow rates. Once gravity flow was established at a given j_w , the infiltration water was changed to 100 mg L^{-1} KBr solution (i.e., by replacing the irrigation head with another one, already filled with KBr solution). The electrical conductivity

(EC) of the outflow was monitored to obtain the flux concentration. We measured BTCs for eight different j_w values at steady state in response to a step input. We started with the lowest j_w value of 0.5 cm h^{-1} , which was increased stepwise. The use of EC to measure tracer BTCs is possible since the sand was cleaned of organic materials and reactive minerals (nevertheless we noted the presence of some trace amounts). The transport experiments were conducted without stopping infiltration (thus, switching between deionized water and KBr solution). At the end of each experiment, the KBr solution was flushed out of the sample using at least 10 pore volumes of deionized water. While flushing, the EC was monitored until it attained a background and stable value, and then the next experiment was conducted. The BTCs were modeled based on a one-dimensional analytical solution of the CD model using CXTFIT module [88] in STANMOD [103] by optimizing for v and D_{eff} . A first-type boundary condition representative of flux-averaged concentration was used. For all measured BTCs both v and D_{eff} could be clearly identified.

2.4 Result and Discussion

2.4.1 Multistep-Outflow Approach

In Figure 2.3 the dynamics of cumulative outflow and h_m in response to decreasing and increasing pressure steps are shown together with the solution of Richards equation for optimized hydraulic parameters. As is typical for sand, there is a marked air entry in the pressure range between -20 and -30 cm, and most of the drainage occurred in the range above -60 cm. The experimental data could be fitted moderately well, including hysteresis. In the range between -20 and -30 cm the dynamics of water outflow are characterized by rapid outflow immediately after the pressure step followed by a period of much slower outflow while h_m was already constant. This is a typical effect of hydraulic non-equilibrium, which cannot be described by Richards equation [25, 108]. Nevertheless, as a main result of the MS-O experiment we obtained the optimized hydraulic parameters (Table 2.1) for the hysteretic water characteristic, $h_m(\theta)$ and the unsaturated conductivity function, $K(\theta)$, according to the parameterization of van Genuchten [96] and Mualem [66]. The corresponding hydraulic functions are shown in Figure 2.4.

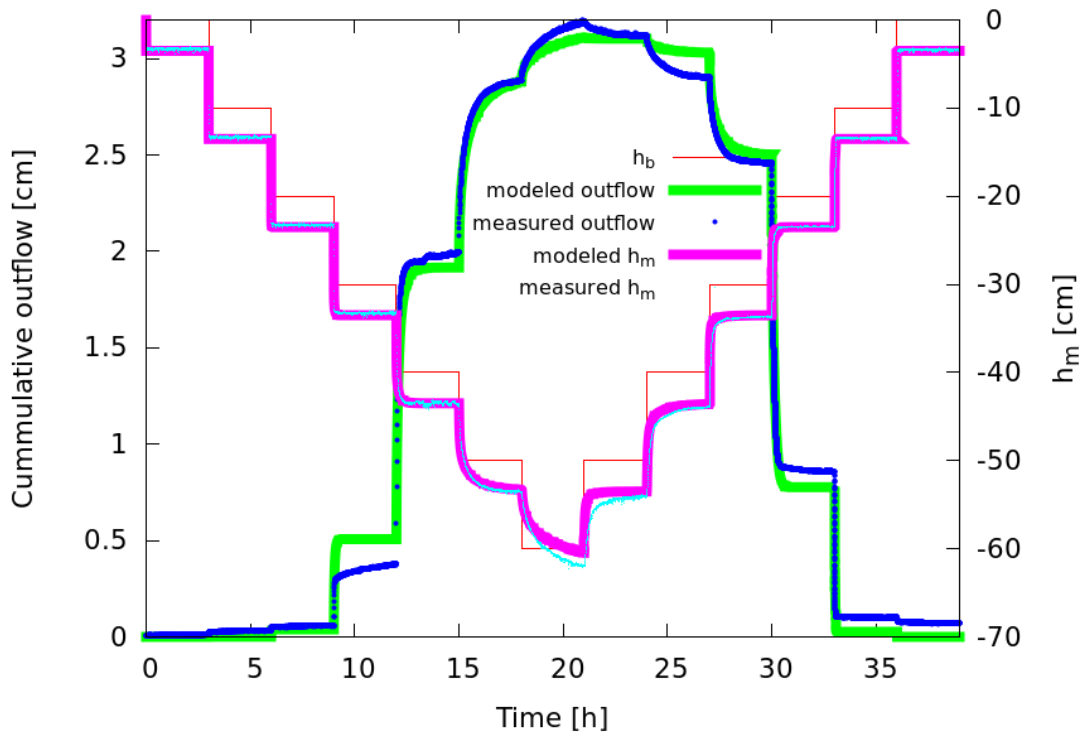


FIGURE 2.3: Result obtained from multistep–outflow (MS–O) experiment for fine–grained quartz sand (grain diameter: 0.1–0.3 mm) indicating imposed pressure at the lower boundary of column (h_b) for drainage and imbibition, measured and modeled outflow, and pressure head (h_m).

TABLE 2.1: Optimal parameters obtained from inverse modeling of multistep–outflow (MS–O) water content (θ) and pressure head (h_m) dynamics for fine–grained quartz sand (0.1–0.3 mm grain diameter): θ_r and θ_s are residual and saturated water contents, α_i and α_d , scaling factors for imbibition and drainage, and n , τ , and K_s are shape parameter, tortuosity factor, and saturated hydraulic conductivity, respectively.

<i>Medium</i>	n	α_i cm^{-1}	α_d	τ	θ_r	θ_s	K_s cm h^{-1}
Sand	9.429	0.033	0.023	0.4	0.02	0.35	17.0

2.4.2 Multistep-Flux Approach

Figures 2.5(a) and 2.5(b) show the results of the MS–F experiment for drainage and imbibition, respectively. Following a sudden change in h_m after each j_w step there is a relatively slow movement of h_m in the opposite direction toward some equilibrium state while θ remains almost constant. This h_m overshoot is another manifestation of hydraulic non–equilibrium as discussed in previous studies

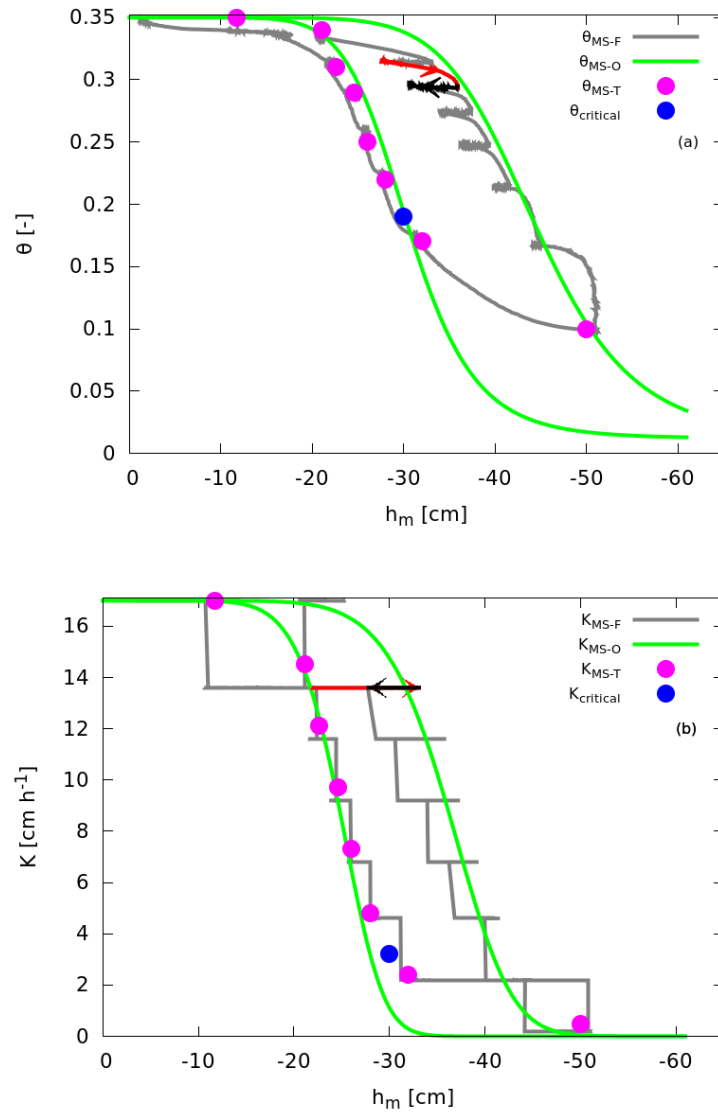


FIGURE 2.4: (a) Hysteretic water retention characteristic obtained via inverse parameter optimization based on multistep-outflow (MS-O) and directly measured trajectories of state variables during multistepflux (MS-F) experiments. Also indicated are the measured water contents (θ_{MS-T}) during the transport experiment (pink dots) and the critical water content ($\theta_{critical}$) at which dispersivity increased abruptly (blue dot). The red arrow shows a fast adaptation of h_m after a step change in boundary j_w (i.e., trajectory toward a non-equilibrium state) followed by a slow equilibration phase (i.e., trajectory toward some quasi-equilibrium state) indicated as the black arrow. (b) Hysteretic hydraulic conductivity function obtained via inverse parameter optimization based on MS-O (K_{MS-O}) and trajectories of K - h_m directly measured during MS-F (K_{MS-F}). Also indicated are the measured hydraulic conductivity (K_{MS-T}) during the transport experiment (pink dots) and the critical hydraulic conductivity ($K_{critical}$) at which dispersivity increased abruptly (blue dot). The red arrow shows a fast adaptation of h_m after a step change in boundary j_w (i.e., trajectory toward a non-equilibrium state) followed by a slow equilibration phase (i.e., trajectory toward some quasi-equilibrium state) indicated as the black arrow.

(e.g., [108, 109]). The second tensiometer (T2 in Fig. 3.1; h_{ml} [L] in Fig. 2.5) confirmed that the vertical profile of h_m was uniform shortly after each flux step, so that gravity flow as well as a uniform profile in θ was established. Hence, we obtained the unsaturated hydraulic conductivities for different h_m . The MS–F result also quantified the water retention characteristic of the sample if we consider the magnitude of change in h_m versus θ (Fig. 2.4).

2.4.3 Multistep–Transport Approach

As demonstrated by the MS–F approach (Fig. 2.5), adjusting the lower boundary pressure, h_b [L] to the value measured by the upper tensiometer h_{mu} [L] led to a uniform h_m profile along the vertical (z) axis (i.e., $h_b \approx h_{mu} \approx h_{ml}$). After each j_w step, a state of dynamic equilibrium was reached. The entire column was either on a wetting curve (increasing j_w steps) or on a drying curve (decreasing j_w steps). In this case, it can be assumed that a uniform h_m translates into a uniform θ and a uniform geometry of the flow field. These are ideal conditions to investigate solute transport at different j_w values and different hydraulic states. We measured solute (KBr) BTCs for increasing j_w steps since the non–equilibrium phenomena were much less pronounced compared to decreasing j_w steps (Fig. 2.5). Thus, a quasi–equilibrium state was established much faster during imbibition. A plausible explanation for this phenomenon is that during imbibition, entrapped gas has the tendency to be stabilized whereas during drainage, water in larger pores entrapped through narrow pore necks has the tendency to be destabilized. The measured BTCs are expressed as relative concentration versus pore volume (Fig. 2.6). After fitting the parameters v and D_{eff} (Table 2.2), all experiments could be described by the CD model (see Table 2.2 for goodness of fit given by the coefficient of determination, r^2).

The volumetric water content, θ_{MS-T} [–], which was calculated from the weight of the column measured at high temporal resolution, is essentially uniform, while j_w is given by the upper boundary condition and pore–water velocity, v_{MS-T} [L T^{–1}] ($= j_w/q_{MS-T}$), was determined directly. The inverted pore–water velocity using CXTFIT, v_{CXTFIT} [LT^{–1}], corresponds almost exactly to v_{MS-T} (Fig. 2.7). We conclude that the water phase was connected during transport and the entire volume of water for the respective j_w contributed to solute transport. Since θ_{MS-T}

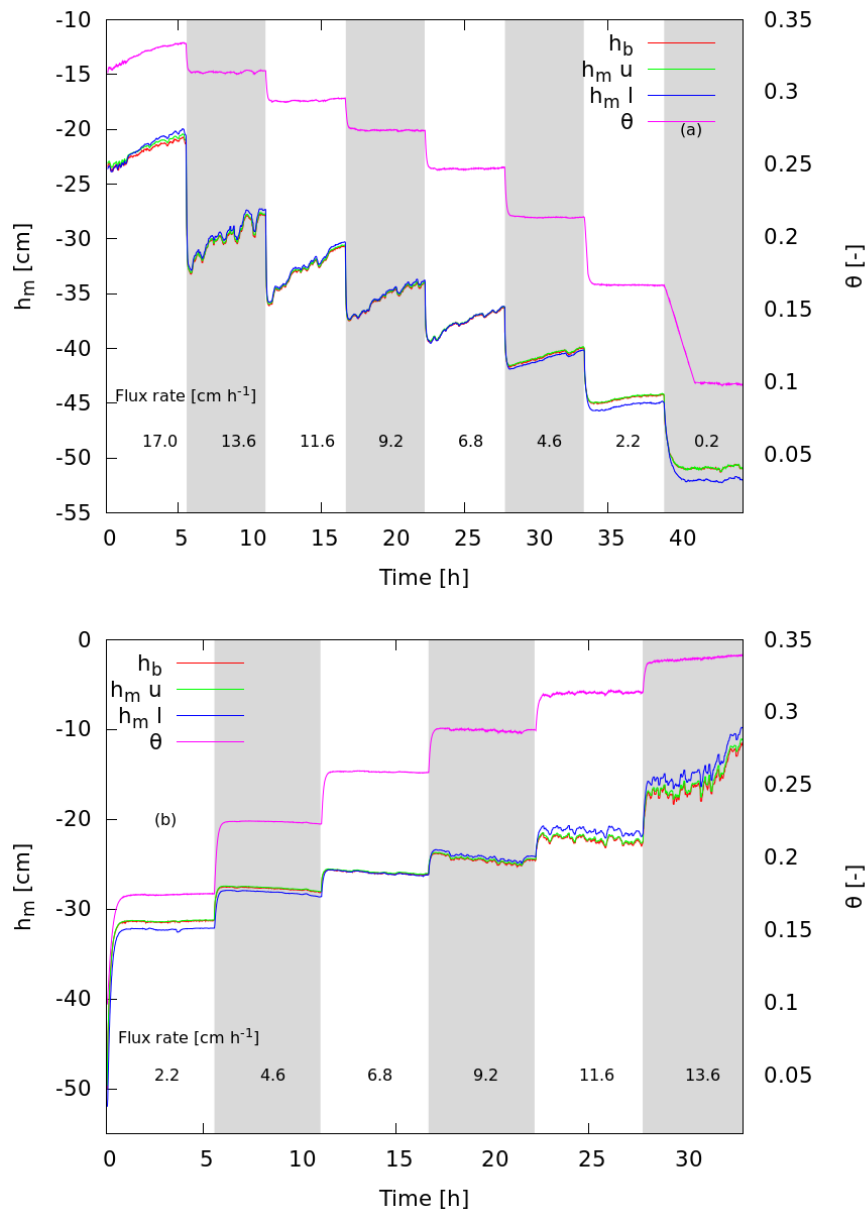


FIGURE 2.5: (a) Dynamics of pressure head (h_m) and volumetric water content (θ) during stepwise decrease (drainage) in infiltration rate (j_w) during multistep-flux (MS-F) and (b) for increasing infiltration steps. h_b , $h_{m l}$, and $h_{m u}$ are lower boundary pressure (Pc1), upper (T1), and lower (T2) pressure heads within the column.

was fairly uniform and h_m was constant throughout the vertical height of the column, no depth correction for θ (e.g., [98]) was required.

In the dry range, λ increased substantially (Fig. 2.8), and the asymmetry of BTCs was apparent. Decrease in θ may increase the proportion of pore regions with reduced accessibility. This will be explored in more detail when analyzing the pore structure further below. Padilla et al. [67] noted that smaller flow channels, tortuosity increase, prolongation of travel path, and the occurrence of water films (enveloping grains) are characteristic of unsaturated flow and solute movement, and, as a consequence, experimental data may not conform to a CD solution. Our experiment could be explained along the same lines; thus, increased tortuosity and a prolonged travel path are apparent in the dry range and reflected by increased sensitivity of λ with respect to changes in θ and v (see insert in Fig. 2.8). However, the CD model was able to describe the experimental data even for the lowest j_w where the shape of the BTC becomes asymmetric. The validity of the CD model is further corroborated by the agreement between v_{CXTFIT} and v_{MS-T} . Another indication for the validity of the CD model is the macroscopic Peclet number defined as $Pe = z/\lambda$ (where $z = 10$ cm is the transport distance). Except the lowest j_w , Pe is larger than 10 for all other flow rates (Table 2.2). It is noted that transport is controlled purely by diffusion if $Pe < 2$, a combination of diffusion, convection, and dispersion, if $2 < Pe < 9$ and mainly by convection and dispersion if $Pe > 9$ (e.g., [41]). For the lowest j_w with $Pe = 3.2$, we are close to the limit of applicability of the CD model, and the small ratio between z and λ explains the asymmetry of the BTC.

2.4.4 Consistency of Multistep–Outflow, Multistep–Flux and Multistep–Transport Approaches

The MS–O and MS–F approaches provide consistent results with respect to the hydraulic properties, including hysteresis (Fig. 2.4). In Figure 2.4, the pink dots represent the various hydraulic states during the MS–T experiment while the blue dot represents the critical region where λ increased substantially. The hydraulic states of the MS–T experiment are a subset of those of the MS–F experiment. The MS–O experiment provides hydraulic functions optimized for the given protocol of applied pressure steps. This is illustrated for the water retention characteristics (Fig. 2.4a) and for the unsaturated hydraulic conductivity function (Fig. 2.4b).

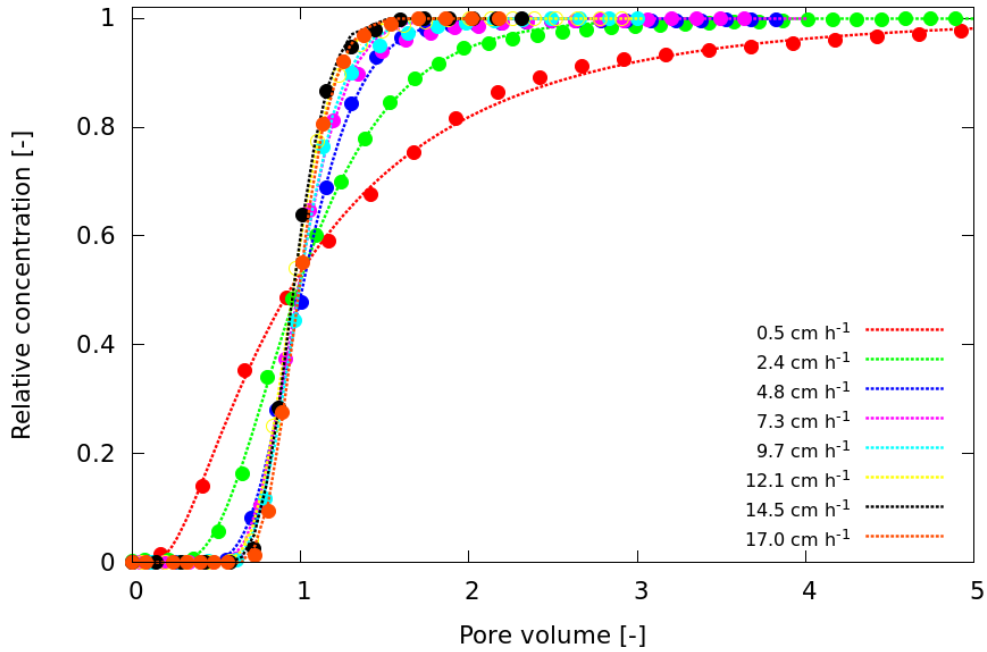


FIGURE 2.6: Breakthrough curves for various flow rates as normalized flux concentration versus infiltrated pore volume.

TABLE 2.2: Transport parameters obtained by multistep-transport (MS-T) approach: flux rate (j_w), measured volumetric water content (θ_{MS-T}), directly measured mean pore-water velocity, v_{MS-T} ($= j_w/\theta_{MS-T}$, optimized mean pore-water velocity using CXTFIT (v_{CXTFIT}), effective mean velocity, effective dispersion coefficient (D_{eff}), dispersivity (λ), molecular diffusion coefficient (D_m), measured pressure head (h_m), macroscopic pecelet number (Pe), and coefficient of determination (r^2).

j_w cm h ⁻¹	θ_{MS-T}	v_{MS-T} cm h ⁻¹	v_{CXTFIT} cm h ⁻¹	D_{eff} cm ² h ⁻¹	λ cm	D_m cm ² h ⁻¹	h_m cm	Pe	r^2
0.5	0.10	5.0	3.8	15.72	3.14	0.003	-50.0	3.2	0.999
2.4	0.17	14.6	13.5	14.15	0.97	0.009	-32.0	10.3	0.999
4.8	0.22	22.3	21.4	7.43	0.33	0.017	-28.0	30.0	0.999
7.3	0.25	28.7	28.5	7.20	0.25	0.024	-26.0	39.9	0.999
9.7	0.29	34.0	33.6	6.95	0.20	0.032	-24.6	48.9	0.999
12.1	0.31	38.8	39.8	7.32	0.19	0.039	-22.6	53.0	0.999
14.5	0.34	43.4	44.7	6.29	0.14	0.046	-21.1	69.0	0.999
17.0	0.37	48.5	48.4	6.48	0.13	0.051	-11.7	74.9	0.999

The observable differences within the state space of θ and h_m for the MS-O and MS-F or MS-T can be explained by non-equilibrium effects. Obviously, for the investigated sand, there is considerably less non-equilibrium during imbibition as

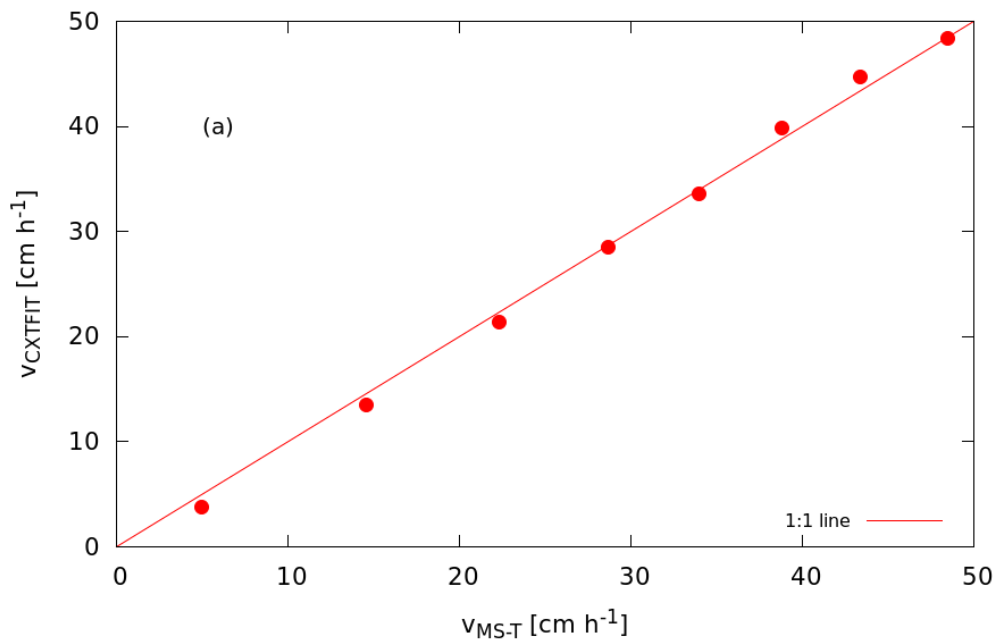


FIGURE 2.7: Validation of the multistep-transport (MS-T) approach for average pore-water velocity, v [i.e., obtained using CXTFIT (v_{CXTFIT}) versus measured directly (v_{MS-T})].

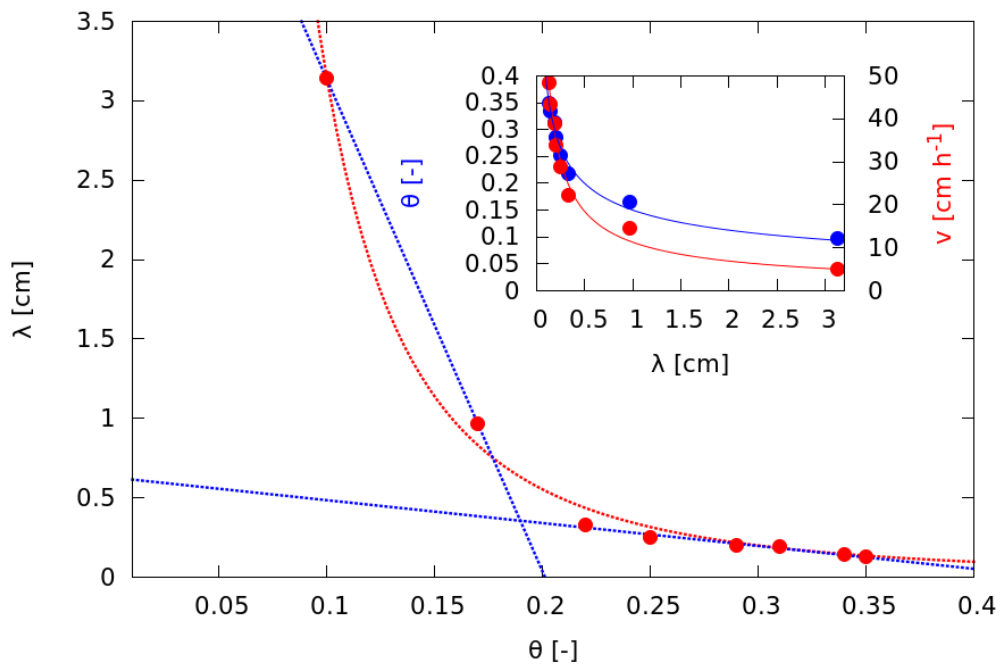


FIGURE 2.8: Optimized dispersivity (λ) using CXTFIT as a function of water content (θ) (the insert figure is a plot of θ and pore-water velocity, v versus λ)

compared to drainage. As hypothesized, water in larger pores entrapped through narrow pore necks has the tendency to be destabilized during drainage whereas entrapped gas has the tendency to be stabilized during imbibition. Consequently, a quasi-stable phase distribution is reached faster behind an imbibition front as compared to a drainage front.

For the drainage branch, the MS-O result is close to the non-equilibrium state measured by the MS-F approach, especially for the water retention characteristic (Fig. 2.4a). Obviously, the hydraulic parameters obtained using the MS-O approach are afflicted by the phenomenon of hydraulic non-equilibrium. This is evident at the air-entry point (step from -20 to -30cm) where some equilibrium state is approached very slowly (Fig. 2.3). The duration of pressure steps during the MS-O experiment was 3 h while the duration of flux steps during MS-F was in the range of 5 h. Yet, the results of MS-O corresponds to what is obtained by MS-F immediately after the flux step. We speculate that during stationary infiltration (the MS-F approach), the development toward some equilibrium state is faster because of additional viscous forces as compared to the static pressure steps in the MS-O experiment.

While the lowest j_w was established after drainage, the other flow rates were established during imbibition. They almost perfectly agree with the imbibition branch of the hydraulic functions as obtained from MS-O. In summary, the combination of MS-O, MS-F, and MS-T approaches provide the material properties $\theta(h_m)$, $K(h_m)$ and $\lambda(\theta)$ in a consistent way.

2.4.5 Structure Analysis to Interpret Unsaturated Transport

The sudden increase in λ as θ reduces below 0.2 (Fig. 2.8) can be interpreted as a considerable change in the geometry of the flow field. We note that λ is more sensitive to changes in θ and v within the dry range (see insert in Fig. 2.8). Based on the three-dimensional X-ray CT image of the pore structure, we could calculate the distribution of the fluid (air and water) phase at various h_m values to visualize the expected geometry of the flow field in the state of energetic minimum. The images were subject to a simple cluster analysis to identify which part of the water phase can be assigned to a percolating continuous cluster (i.e., connected to the

inlet and outlet boundaries) and which parts are disconnected (i.e., water filled but not connected to the inlet and outlet boundaries) and forming isolated clusters. It should be noted that the isolated water clusters obtained by image analysis are expected to be hydraulically connected via water pathways that are thinner than the image resolution ($7.0 \mu\text{m}$). Hence, these clusters may still contribute to flow and transport, but they are only accessible through regions of very low conductivity. The fraction of isolated water-filled pores is negligible close to saturation but increases as θ decreases (Fig. 2.9). The distribution of the three phases, solid, air, and water, at $\theta = 0.11$ is illustrated in Fig. 2.10(a). In Fig. 2.10(b), only the distribution of isolated (green) and percolating (blue) water is shown for the same water content. For $\theta > \theta_{critical}$ almost the entire pore space is connected to both inlet and outlet boundaries, creating a dense network of flow paths, and any point within the water phase is in short distance to some flow path of relatively high velocity. For $\theta < \theta_{critical}$, however, the fraction of disconnected water clusters increases, leading to a substantial change in the characteristics of the flow field. This is characterized by a continuous pore network connected to both inlet and outlet boundaries (blue in Fig. 2.10b) and isolated clusters of pores connected to the continuous phase via films (green in Fig. 2.10b). The water within these isolated clusters interacts with the continuous flow paths, but the limited exchange through narrow paths increases the overall dispersivity. The early breakthrough of the tracer for lower water contents is due to fast flow along the continuous water phase, and the tailing is due to solute exchange between the continuous water phase and the isolated water clusters. We conclude from our results that the continuity of the water phase is the most important feature explaining the observed increase in λ . We are aware that this can only be an approximation of the real situation because the phase distribution was calculated for the simplified case of an energetic minimum according to the Young–Laplace equation.

2.5 Conclusion

We introduced a comprehensive experimental approach combining multistep–outflow, multistep–flux, and multistep–transport (MS–OFT) for studying soil hydraulic and solute transport properties using a single experimental setup without moving the sample from one device to another. The new component, MS–T, provides BTCs at constant h_m and uniform θ and thus provides an experimental approach

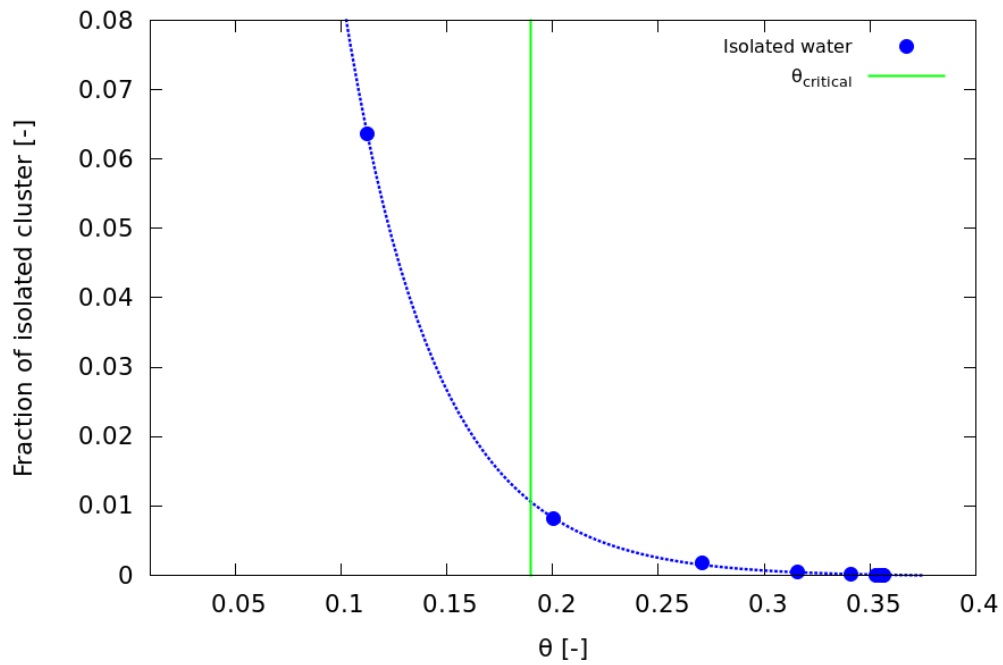


FIGURE 2.9: The fraction of isolated water clusters versus water content (θ) derived from cluster analysis of a three-dimensional image obtained from X-ray computed tomography

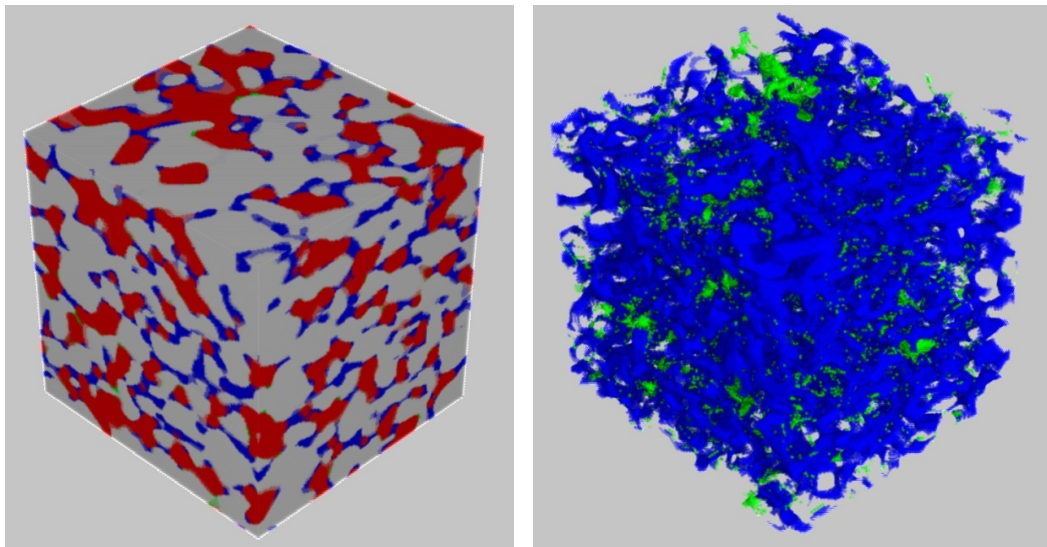


FIGURE 2.10: (a) Distribution of air (red), solid (gray) and water [i.e., continuous (blue) and isolated (green) water clusters at $\theta = 0.11$ based on a three-dimensional image obtained from X-ray computed tomography. (b) Distribution of percolating (blue) and isolated (green) water clusters at $\theta = 0.11$ based on a three-dimensional image obtained from X-ray computed tomography.

to measure solute dispersivity as a function of water content, $\lambda(\theta)$. While the hydraulic properties $h_m(\theta)$ and $K(\theta)$ have been studied a lot, this extension for solute transport is new and provides a more complete picture. We demonstrate

that the combined experimental approach, MS-OFT produces consistent results, including the hysteretic behavior of the hydraulic functions. For the sand investigated here, we found a non-linear increase in λ with decreasing θ at decreasing j_w . This could be explained by structure analysis based on X-ray CT images where the geometry of the flow field could be addressed through the connectivity of the water phase at different saturations. Our experimental results together with the analysis of the pore structure provide a framework toward a holistic understanding of water dynamics and solute transport in unsaturated porous media. It has to be expected that the relation $\lambda(\theta)$ is also hysteretic, but this will be the subject of future research.

Chapter 3

Transport of citrate-coated Ag nanoparticles in unsaturated sand

3.1 Abstract

Chemical factors and physical constraints lead to coupled effects during particle transport in unsaturated porous media. Studies on unsaturated transport as typical for soils are currently scarce. In unsaturated porous media, particle mobility is determined by the existence of an air–water interface in addition to a solid–water interface. To this end, we measured breakthrough curves and retention profiles of citrate-coated Ag nanoparticles in unsaturated sand at two pH values (5 and 9) and three different flow rates corresponding to different water contents with 1 mM KNO_3 as background electrolyte. The classical DLVO theory suggests unfavorable deposition conditions at the air–water and solid–water interfaces. The breakthrough curves indicate modification in curve shapes and retardation of nanoparticles compared to inert solute. Retention profiles show sensitivity to flow rate and pH and this ranged from almost no retention for the highest flow rate at pH = 9 to almost complete retention for the lowest flow rate at pH = 5. Modeling of the breakthrough curves, thus, required coupling two parallel processes: a kinetically controlled attachment process far from equilibrium, responsible for the shape modification, and an equilibrium sorption, responsible

This chapter has been published: Kumahor, S.K., P. Hron, G. Metreveli, G. E. Schaumann, H.–J. Vogel. 2015. Transport of citrate-coated silver nanoparticles in unsaturated sand. *Science of the Total Environment* 535 (2015) 113–121. <http://dx.doi.org/10.1016/j.scitotenv.2015.03.023>.

for particle retardation. The non-equilibrium process and equilibrium sorption are suggested to relate to the solid–water and air–water interfaces, respectively. This is supported by the DLVO model extended for hydrophobic interactions which suggests reversible attachment, characterized by a secondary minimum (depth 3–5 kT) and a repulsive barrier at the air–water interface. In contrast, the solid–water interface is characterized by a significant repulsive barrier and the absence of a secondary minimum suggesting kinetically controlled and non-equilibrium interaction. This study provides new insights into particle transport in unsaturated porous media and offers a model concept representing the relevant processes.

Keywords: Air–water interface; Solid–water interface; Engineered nanoparticle; Extended DLVO theory; Unsaturated flow; Pore structure.

3.2 Introduction

Ongoing efforts to understand mechanisms governing transport and retention of engineered nanoparticles (NPs) in porous media are motivated by their wide array of application. For instance, engineered Ag NPs are used for antibacterial [18, 115], conductive [44], diagnostic and therapeutic [21, 83], and optical [111] applications. Incidentally, NPs may be released and enriched in some compartments of the ecosystem (e.g., soils and surface waters) relative to their natural background occurrence [4]. Due to their toxic and bioaccumulative tendencies, engineered Ag NPs may pose hazard upon environmental exposure. This calls for systematic investigation into their interaction within the unsaturated zone which cushions groundwater against potential long-term contaminant sources [76].

Mechanisms governing particle transport in porous media are multifaceted ranging from geometric and hydrologic to hydrogeochemical controls. Previous studies are mostly focused on transport under fully saturated conditions (e.g., [9, 60, 107]), while transport under unsaturated conditions (e.g., [32]) still requires systematic investigation to elucidate governing mechanisms. During unsaturated flow, capillary forces are expected to control colloid interaction in the vicinity of air–water interface (AWI) (e.g., [11, 55]) and this tendency could be crucial for their transport. This phenomenon has not been fully investigated for engineered NPs especially with their specialized nature in terms of charge, reactivity and size. The

size of engineered NPs poses challenges to directly investigate the influence of capillary forces during transport. Hence, DLVO (e.g., [32, 89]) and extended DLVO (e.g., [11]) analyses are often combined with column experiments to gain insight. The classical and extended DLVO models could provide a priori an affinity index between NPs and potential collectors (AWI and solid–water interface, SWI) during transport.

We investigated unsaturated transport of citrate–coated Ag NPs within repacked sand as model porous media. The zeta (ζ) potential [$\text{ML}^2\text{T}^{-3}\text{A}^{-1}$] of clean quartz and glass is typically between -10 and -80 mV depending on the solution chemistry [30, 31, 45, 72]. Some studies suggest that the AWI bears no charge (e.g., [63]) while others reported charges in the range of -4 to -110 mV depending on solution composition (e.g., [11, 17, 57, 84, 113]). Grain surfaces which are not completely wettable may have air–water–solid (AWS) contact points. In contrast, water films may extend infinitely on completely wettable grain surfaces [55]. Both cases present avenues for straining either near AWS contact points or in water films of comparable size as NPs [76]. Chen and Flury (2005) observed colloid retention for unsaturated flow and thermodynamic properties have been suggested to play a role. Colloid retention in porous media was observed under electrostatically unfavorable deposition conditions (e.g., [12, 89, 93]) and straining has been suggested by the authors as a dominant retention mechanism. This provides a hint that physical and chemical factors may be coupled in the governing transport mechanism. Colloid transport is expected to increase for moving AWI [64] or decrease for stationary AWI [55]. Fang et al. [32] reported that decrease in water content, θ [–], had little impact on TiO_2 NP mobility owing to the net repulsive interaction between negatively charged AWI and TiO_2 NPs.

The limited number of studies on unsaturated transport of engineered NPs could be due to the difficulty in establishing well–defined experimental conditions [76]. This difficulty is further augmented by the complexity associated with the phase distribution of pore fluids (air and water) and the coupled effects of physical constraints and chemical factors. This complicates the identification of an appropriate process model. Recently, the technical problem to establish well–defined unsaturated flow conditions (i.e., constant pressure head, h_m [L], and uniform θ) has been largely solved by the newly developed multistep–flux (MS–F) approach [108, 109] and the related multistep–transport (MS–T) approach [50]. In this study, we used the new experimental tools to explore in a systematic way and with well–controlled

experimental conditions, the transport of citrate-coated Ag NPs at three different flow rates, j_w [LT^{-1}], two pH levels (5 and 9) and at a fixed pore-water ionic strength (1 mM KNO_3). Furthermore, the transport of citrate-coated Ag NPs in unsaturated sand was modeled by using a modified form of the convection-dispersion (CD) equation. The classical and extended DLVO interaction energy profiles were calculated to characterize collector-NP interaction.

3.3 Materials and method

3.3.1 Silver nanoparticles

The citrate reduction method was used for the synthesis of Ag NPs. The synthesis procedure is detailed in Metreveli et al. [65] together with the characterization of the Ag NPs. The citrate-coated Ag NPs are quasi-spherical with a hydrodynamic diameter, h_d [L], of about 40 nm. For the transport experiments, the stock of 100 mg L^{-1} Ag NP dispersion was further diluted (ratio of 1:100). The resultant dispersion was adjusted to a background electrolyte concentration of 1.0 mM KNO_3 (extra pure, MERCK) and the pH adjusted to 5 and 9 using HNO_3 (65% Suprapur, MERCK) and NaOH (pure, MERCK) respectively.

3.3.2 Sand medium

The sand (Co. Sand-Schulz, Berlin) used for the transport experiments has a grain size distribution of 0.1–0.3 mm with a median grain diameter, d_{50} [L], of 0.2 mm. The same sand was used by Kumahor et al. [50] for tracer studies. A similar grain size (275 μm) is typically used in sand filters (e.g., [19]). The sand was packed to a bulk density, ρ_b [ML^{-3}], of 1.52 g cm^{-3} . According to its industrial specifications, the cleaned sand may contain trace amounts of organics and reactive minerals. We used cleaned sand as model porous medium to: (i) exclude as much as possible the influence of organics and reactive minerals, and (ii) direct our focus towards understanding the impact of AWI on particle transport.

3.3.3 Water flow dynamics and transport experimental protocol

We combined studies on the experimental determination of hydraulic properties (i.e., moisture release and conductivity functions) with transport characteristic (for both inert solute and NPs), at the scale of a lab column to investigate the mobility of NP for well-defined hydraulic states and delineated chemical conditions in terms of pH and pore water ionic strength. The experimental column was a polyvinyl chloride (PVC) cylinder of dimensions 16.2 cm (inner diameter) and 10 cm (column height). The column was fitted on a porous glass plate with a higher conductivity compared to the sand. The low air entry point of this plate allowed for controlling h_m at the lower boundary (Fig. 3.1). The column was dry-packed while tapping gently on the sides to ensure a uniform ρ_b .

The water retention characteristic and the unsaturated hydraulic conductivity function were measured using the multistep-outflow (e.g., [36, 95, 117]) and MS-F [108, 109] approaches. The results [50] were used to design the NP transport experiments which aimed at investigating the influence of pH and flow regime (thus, structure of the flow field). Two pH values (5 and 9) and three flow rates (i.e., 2.5, 9.7 and 17.0 cm h⁻¹) corresponding to three different θ values (i.e., 0.17, 0.29 and 0.35 respectively) and pore-water velocities, v [LT⁻¹], (i.e., 14.7, 33.4 and 48.6 cm h⁻¹ respectively) were investigated with a 1 mM KNO₃ background electrolyte. With a constant j_w established via a peristaltic pump (ISMATEC) such that a constant h_m and uniform θ were realized during water flow (Fig. 3.2), we conducted the NP transport experiments along the following steps: (1) prior to application of Ag NP dispersion, the column was flushed with 5 pore volumes (PVs) of the background electrolyte solution and also to establish a stationary flow field, (2) then, 8 PVs of the Ag NP dispersion were delivered through 19 evenly distributed hypodermic needles at the surface, (3) this was followed by another 8 PVs of Ag NP-free solution to quantify the mass of NPs irreversibly retained, (4) the column was then dissected into layers of 1 cm height and oven dried at 105 °C for 24 h. The sand was homogenized and a subsample (10 g) taken for leaching studies. The retention profiles (RPs) were measured as follows: (a) the sand was moistened with some Milli-Q water, (b) 5 mL of 65% suprapur HNO₃ was added, (c) the content was placed in an ultrasonic bath at about 60 °C for 10 min, (d) then topped up to 50 mL with Milli-Q water, (e) this was followed by centrifugation (f)

and the supernatant diluted 1:50 with Milli-Q water for ICP-MS measurements.
 (5) A mass balance was calculated from the BTCs and RPs.

This procedure was repeated for the different flow rates and pH values. Moisture content was measured using a weighing balance (Balance 1 in Figure 3.1) and h_m was continuously monitored at high temporal resolution using two tensiometers installed at about 2.0 cm and 8.0 cm from the bottom of the column. The experimental conditions for the various flow rates and pH levels are shown in Figure 3.2.

3.3.4 Quantification of air–water–interfacial area

The area of the AWI was quantified as a function of h_m using a 3-D image of the sand from a sample with the same ρ_b ($= 1.52 \text{ g cm}^3$) as the experimental

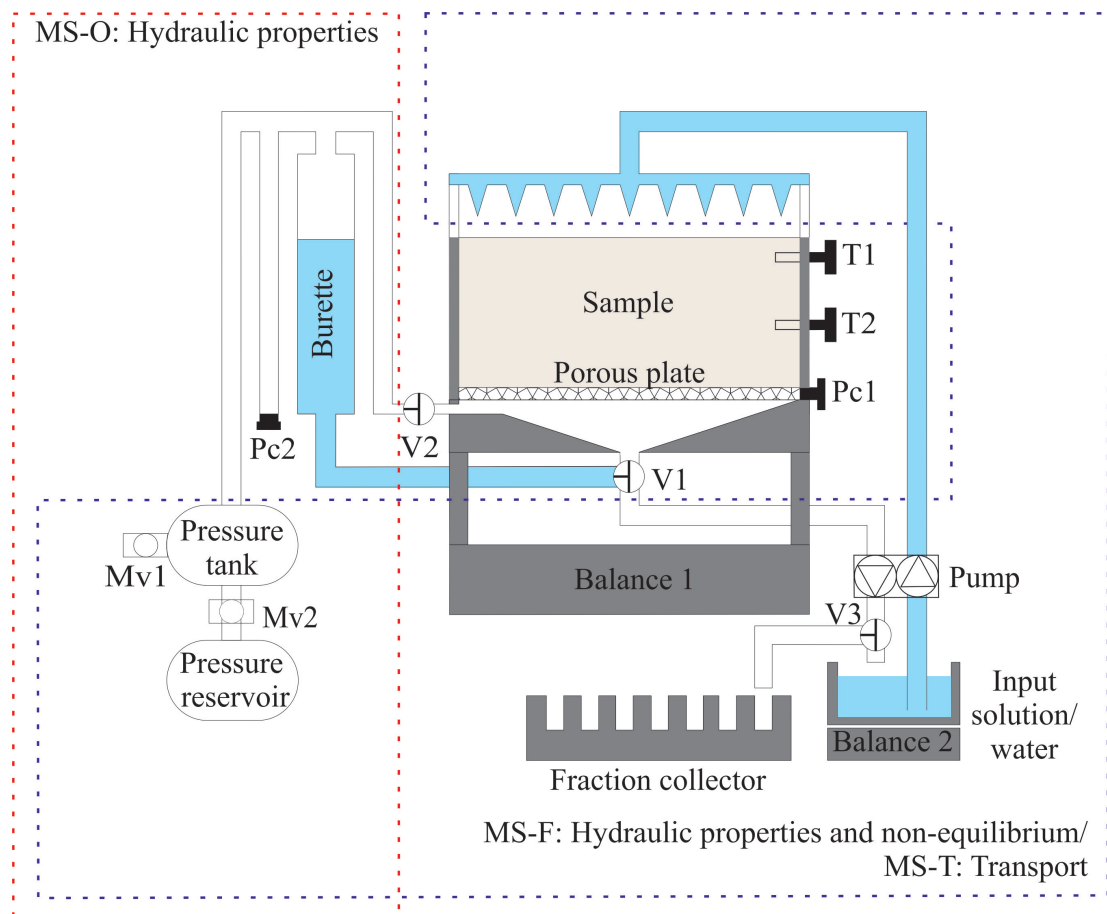


FIGURE 3.1: Multistep-outflow (MS-O), multistep-flux (MS-F) and multistep-transport (MS-T) experimental setup (Figure after Kumahor et al. [50]). The citrate-coated Ag nanoparticle (NP) transport experiment uses the MS-T setup but for a specified flow rate at the top boundary and outflow collected in fractions.

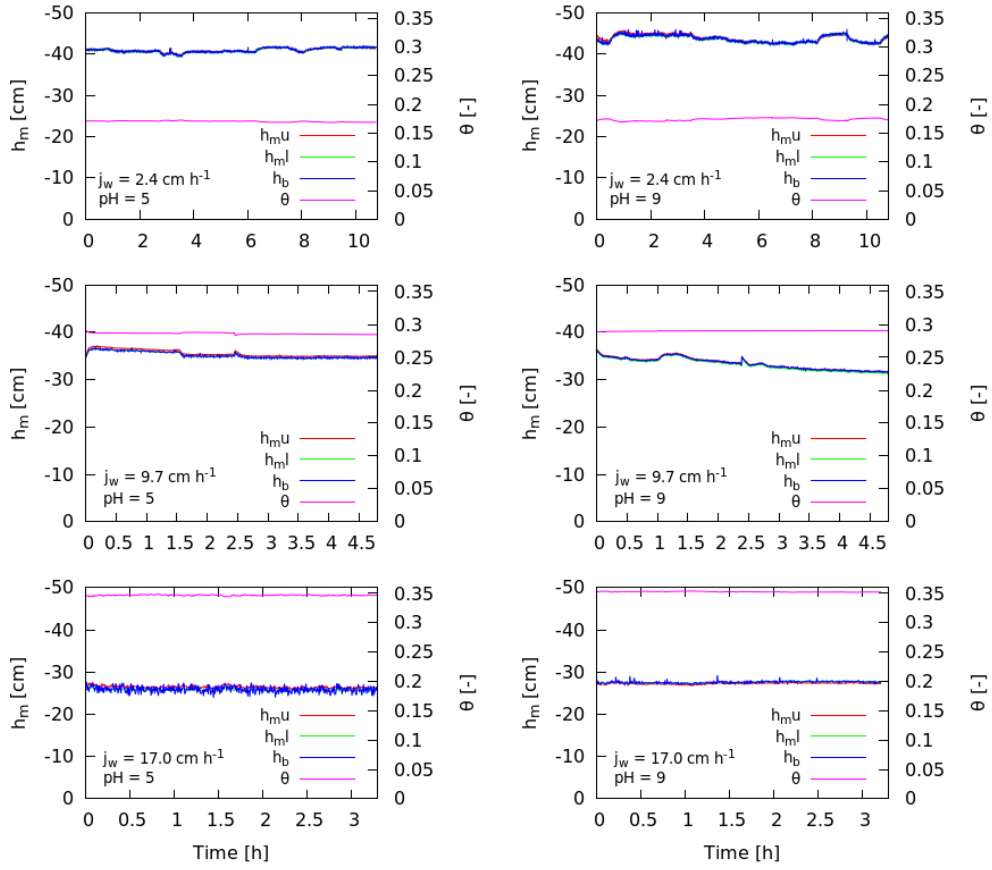


FIGURE 3.2: Experimental conditions during citrate-coated Ag NP transport (from top to bottom: increasing flow rate, j_w ; from left to right: increasing pH). In the legend, $h_{m,u}$, $h_{m,l}$ and h_b are upper, lower and boundary pressure heads respectively.

column obtained using an industrial X-ray CT scanner (X-Tek HMX 225). Image acquisition procedure, pre-processing steps and image segmentation are detailed in Kumahor et al. [50]. After image segmentation, the pore size distribution was derived following standard procedures in mathematical morphology [102]. The area of the AWI was calculated at different h_m values following a procedure detailed in Schlüter et al. [78] based on the fluid phase distribution. The simplifying assumptions of this approach are that: (i) the AWI is spherical, and (ii) its radius of curvature, r [L] is related to h_m in accordance with the Young-Laplace equation (e.g., [101]). With these assumptions, we obtained an approximate area of the AWI for a given h_m at an energetic minimum which should be useful for the interpretation of unsaturated flow and NP transport.

3.3.5 Hydrodynamic size, electro–kinetic characterization and interfacial potential energies

The hydrodynamic diameter, h_d , (e.g., [22, 48] and the zeta (ζ) potential of the citrate–coated NPs were characterized as a function of pH using a particle analyzer (Delsa Nano C, Beckman Coulter, Fullerton, USA; laser wavelength: 658 nm). The h_d was measured using Dynamic Light Scattering (DLS) while the ζ potential was obtained from the electrophoretic mobility of the NPs using the Smoluchowski equation (e.g., [20]). For h_d and ζ potential measurements, the dispersion was adjusted to a background electrolyte of 1.0 mM KNO_3 representative of the pore–water ionic strength established during the transport experiments. In the acidic range (pH = 2 to 6), both HNO_3 and H_2SO_4 were compared for their influence on h_d and ζ potential while NaOH was used to adjust the pH in the neutral to basic range (pH = 7 to 11). The h_d and ζ potential for pH = 5 (using HNO_3) and pH = 9 were used to characterize the classical and extended DLVO interfacial potential energy profiles for NP–collector interaction. The classical DLVO theory describes the interplay between van der Waals attractive forces, E_{vdW} [ML^2T^2] and electrostatic double layer repulsive forces, E_{EDL} [ML^2T^2] as a function of separation distance, h_s [L] while the extended DLVO is the DLVO augmented for hydrophobic interaction, E_{HYD} [ML^2T^2] [11, 29]. The extension for hydrophobic interaction is justified by the presence of AWI and citrate which is amphiphilic. A sphere (NP)–plate (collector) interaction (e.g., [11, 29, 89] was considered given a small h_d of Ag NPs (about 40 nm) relative to either the r of the AWI (varies with θ) or d_{50} . Equations, input parameters and constants used for the calculations are given in the Supplementary data (Appendix A).

3.3.6 Analysis of breakthrough curves

3.3.6.1 Tracer BTCs

The BTCs and model results obtained for the inert solute (KBr solution) are detailed in Kumahor et al. [50]. The travel distance z [L] is 10 cm which is more than two orders of magnitude larger than the characteristic length of the pore structure (i.e., $d_{50} = 0.2$ mm) and hence, a meaningful analysis of transport characteristics can be expected. Modeling of tracer BTCs was based on a 1–D analytical solution of the CD equation using CXTFIT module [88] in STANMOD [103]. The

dispersion coefficients (D_{eff}) of inert solute corresponding to the three j_w values are listed in Figures 3.5–3.7 (see figure captions).

3.3.7 Model formulation: unsaturated transport of silver nanoparticles

We propose a model formulation which is motivated by the qualitative interpretation of the BTCs. There is a steep initial breakthrough followed by a long tailing as typical for non-equilibrium sorption but at the same time the initial breakthrough is shifted in time with respect to the tracer as typical for a simple retardation at equilibrium. Hence, the BTCs suggest two parallel processes controlling NP transport: (i) retardation of NPs relative to the tracer which can be represented by a retardation factor R [–] in analogy to equilibrium sorption and (ii) a non-equilibrium process depicted as unbalanced attachment and detachment rates. With this, we modeled the transport of the citrate-coated Ag NPs using a 1-D form of the CD equation in combination with a reaction term given as:

$$\frac{\partial \theta RC}{\partial t} = \theta D_{eff} \frac{\partial^2 C}{\partial z^2} - j_w \frac{\partial C}{\partial z} - \rho_b \frac{\partial S_{np}}{\partial t} \quad (3.1)$$

where C [ML⁻³] is the concentration of NPs in the aqueous phase, t [T] is time and S_{np} [–] is the amount of attached NPs. For the special case of linear sorption, R relates to an equilibrium sorption coefficient (K_{eq}) given by:

$$R = 1 + \frac{\rho_b K_{eq}}{\theta} \quad (3.2)$$

where $K_{eq} = S_{np}^e / C$ and S_{np}^e is the amount of NPs sorbed under equilibrium conditions. This special case (assumption) holds for the attachment of citrate-stabilized Ag NP to quartz at concentrations of up to 40 g L⁻¹ [2]. For higher NP concentrations, a Langmuir type of Ag NP sorption as observed for bare Ag NP [2] should be expected. The reaction term, illustrated by attachment k_{att} [T⁻¹] and detachment k_{det} [T⁻¹] coefficients, accounts for the non-equilibrium mass transfer between the aqueous phase and the collector:

$$\rho_b \frac{\partial S_{np}}{\partial t} = \theta k_{att} \psi C - \rho_b k_{det} S_{np} \quad (3.3)$$

The relation (Eq. 3.4) incorporates a dimensionless time and depth dependent straining function, ψ [-]:

$$\psi = \left(1 - \frac{S_{np}}{S_{np,max}}\right) \left(\frac{d_{50} + z}{d_{50}}\right)^{-\beta} \quad (3.4)$$

where $S_{np,max}$ [-] is maximal attainable amount of NPs attached for a given chemical boundary and β [-] is a shape factor for retention along the flow path. Hence, the first and second terms on the right hand side of Eq. (3.4) represent temporal dynamics and depth dependent interaction of NPs respectively [59, 60, 89]. When $\beta = 0$, the transport process is strictly time-dependent. A β of 0.432 was considered for sand [60, 89] and 1.532 for undisturbed loamy sand soil [59]. We note that β should depend on factors such as pore geometry, geometry of the flow field (varies for unsaturated flow), NP geometry and pore-water chemistry.

3.3.8 Parameter estimation

The parameters j_w , θ , D_{eff} , k_{att} , k_{det} , R , $S_{np,max}$ and β were either obtained directly from the experiments or estimated via inverse modeling. Flow rate and θ were directly obtained from the transport experiments while D_{eff} was obtained by fitting a 1-D analytical solution of the CD model to tracer BTCs [50]. The $S_{np,max}$ was determined from the RPs. Based on the chosen model (Eqs. (3.1–3.4)), the remaining parameters k_{att} , k_{det} , R and β were obtained via parameter estimation using the Levenberg–Marquardt Algorithm with sensitivities derived by numerical differentiation. The forward model solves the transport equation for the NPs in the aqueous phase (Eq. 3.1) together with the reversible attachment models (Eq. 4.3) and (Eq. 3.4) with given initial concentrations (e.g., [38]). In order to minimize numerical errors, the 10 cm 1-D domain was discretized into 512 elements for cell-centered finite volume simulation (e.g., [38]). The concentration in the last element was taken as outflow concentration in each time step.

3.4 Results and discussion

3.4.1 Size and colloidal stability of citrate-coated Ag nanoparticles

Figures A.1(a) and A.1(b) (in Supplementary data) show the dependence of h_d and ζ potential, respectively, on pH in the range of pH = 2 to pH = 11. For pH = 6 and above, h_d is 40 ± 0.4 nm whereas below pH = 6, h_d increases up to 189 ± 8 nm (H_2SO_4) and 143 ± 5 nm (HNO_3) at pH = 2. Thus, slight and significant aggregation should be taken into account for pH = 5 and pH < 5 respectively. For $7 \leq \text{pH} \leq 11$, ζ potential varies between -40 mV and -65 mV and then increases with decreasing pH to $+4$ mV (H_2SO_4) and $+7$ mV (HNO_3) at pH = 2. At pH ≤ 4 where significant aggregation is apparent, the absolute ζ potential value is below 20 mV. Our finding is in line with Tourinho et al. [91] who noted that a suspension of homogeneously charged particles will remain stable as long as the absolute ζ potential value is greater than 30 mV. Badawy et al. [27] reported no aggregation of citrate-coated Ag NPs in 10mM NaNO_3 solution for $6 < \text{pH} < 9$ which is consistent with our results. We note that between pH = 3 and 5, the ζ potential profiles differ depending on the acid used. The ζ potential value is more positive and h_d is smaller with the use of HNO_3 compared to the use of H_2SO_4 at pH = 3. Additionally, a slightly different point of zero charge (pH_{PZC}) was observed for H_2SO_4 (i.e., pH_{PZC} around = 3) compared to HNO_3 (i.e., pH_{PZC} around = 4). We suggest that at pH = 3, moderate oxidation by excess NO_3^- from HNO_3 may lace Ag NPs surfaces with Ag^+ and this could explain the more positive ζ potential and the smaller h_d .

3.4.2 Consequence of silver nanoparticle hydrodynamic size and attachment properties on transport

The duration of measurement of both h_d and ζ potential including sample preparation was about 30 minutes while the transport experiments lasted for about 3.5, 5 and 11 hours corresponding to j_w values of 17, 9.7 and 2.4 cm h^{-1} (Fig. 3.2). Due to the slight aggregation observed at pH = 5 (Fig. A.1a) and with regard to duration of the transport experiments, there is a tendency of Ag NP aggregation during transport. This should be considered relevant for the longest transport

experiment which lasted for about 11 hours (i.e., $j_w = 2.4 \text{ cm h}^{-1}$) and with h_d to pore diameter, d_p [L] ratio [-] of about 0.005 and higher. This value is greater than the critical h_d/d_p ($= 0.002$) above which colloid straining is reported to be relevant [13]. On the contrary, h_d may remain constant for the transport experiments conducted at $\text{pH} = 9$.

Applying the classical DLVO theory for Ag NP–collector interaction suggests no secondary minimum and a repulsive energy barrier at both collectors (Fig. 3.3a). A repulsive energy barrier at SWI–NP distances ranging between 1 and 2 nm is lower at $\text{pH} = 5$ ($55 kT$) than at $\text{pH} = 9$ ($84 kT$). Diffusion controlled activation energies generally range from 20–40 kJ mol^{-1} (e.g., [7]), which corresponds to 8–16 kT . An energy barrier above this range can be considered high enough to prevent immediate attachment to the primary minimum. Also, colloidal suspensions are usually considered very stable if the energy barrier exceeds 20 kT [29]. At the AWI, the classical DLVO profiles suggest no attachment due to the absence of a primary minimum.

The DLVO theory extended for hydrophobic interactions indicates a repulsive energy barrier for attachment at both collectors and a secondary minimum at the AWI (Fig. 3.3b). The profile characteristics for the SWI suggest kinetically controlled and partly irreversible Ag NP attachment in the primary minimum, independently of whether hydrophobic forces are considered or not. In contrast, the consideration of hydrophobic interactions is relevant for the AWI, where it clearly modifies the DLVO profiles and results in formation of a secondary minimum. For $\text{pH} = 9$, the secondary minimum at the AWI (separation distance = 44 nm and depth = $3.4 kT$) may permit weak but reversible attachment as discussed by Zhou et al. [116] for inter-particle interaction. The repulsive maximum ($39 kT$) and the activation energy required to proceed from the secondary minimum to the primary minimum ($42.4 kT$) is high enough to prevent fast attachment in the AWI primary minimum. For $\text{pH} = 5$, a secondary minimum of $5.1 kT$ and an energy barrier of $4.5 kT$ at the separation distances of 33 nm and 7 nm, respectively, also may suggest a weak but reversible attachment in the AWI secondary minimum. We are however cautious to fully exclude irreversible attachment in the primary minimum since NP with sufficient thermal energy may overcome the $9.6 kT$ activation energy required to proceed to the AWI primary minimum.

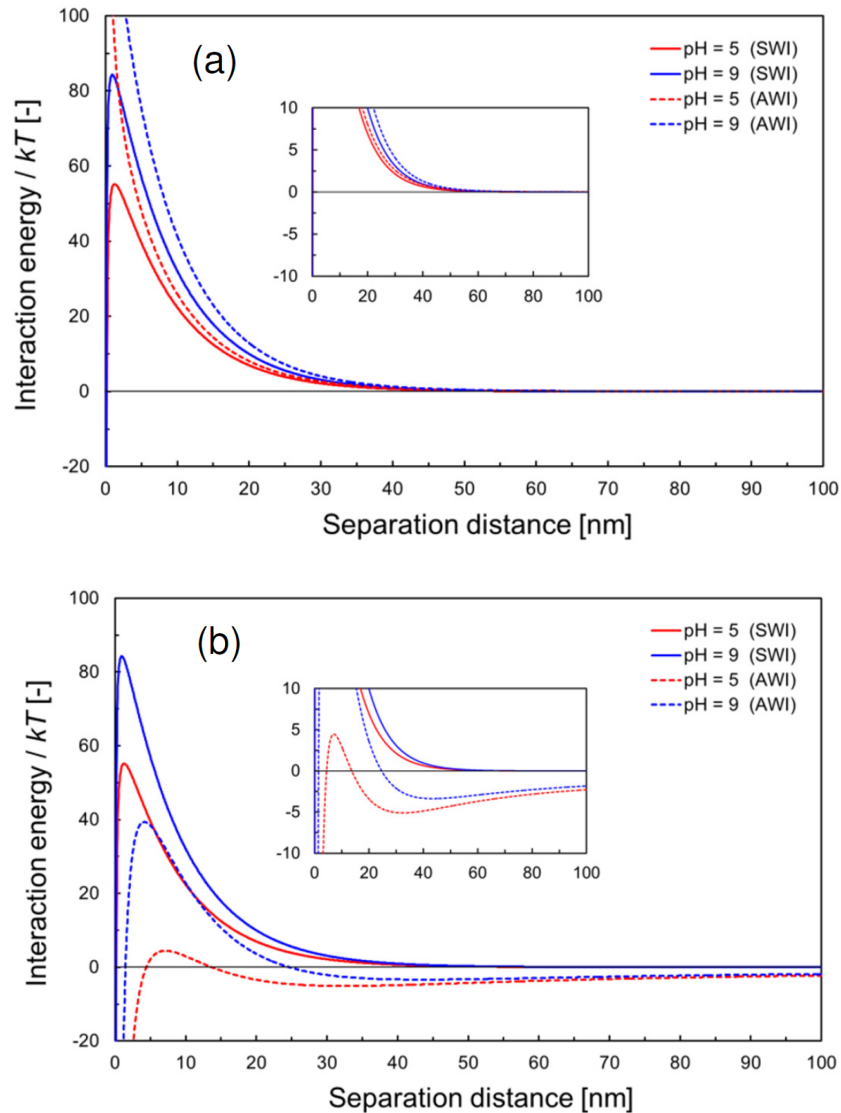


FIGURE 3.3: Dimensionless DLVO (a) and extended DLVO (b) interaction energy profiles for citrate-coated Ag NPs versus solid-water interface (SWI) and air-water interface (AWI) at pH = 5 and pH = 9. The extended DLVO profiles account for hydrophobic interactions. The insert Figures in (a) and (b) represent a section of the interaction energy profiles in order to visualize the absence or presence of secondary minimum.

3.4.3 Tracer and nanoparticle transport characteristics

3.4.3.1 Experimental breakthrough curves and modeling

Figure 3.2 shows the observed θ and h_m during the citrate-coated Ag NP transport experiments for the various j_w values and pH levels. The established θ and h_m depict well-defined unsaturated flow conditions (i.e., uniform θ and constant h_m) while flow is gravity driven. The NP BTCs and the corresponding RPs are

shown in Figs. 3.5 to 3.7. The experimental results and model outputs are indicated as points and lines respectively. All the BTCs could be modeled reasonably well (goodness of fit given by the coefficient of determination, r^2 values are listed in Table 3.1) except for the lowest j_w (2.4 cm h⁻¹) at pH = 5. Under these conditions, NPs were almost completely retained within the column. We obtained a consistent mass balance for this experiment with slight overestimation at the solid phase as shown in Table 3.1. The BTCs depict a non-linear increase in mobility with increasing j_w and θ , and lower NP mobility at pH = 5 compared to pH = 9. The presence and absence of a secondary minimum at the AWI and SWI, respectively, justify coupling of equilibrium sorption for the AWI with an attachment-detachment model for SWI as represented by the chosen model (Eqs. (3.1)–(3.4)). The resulting differences in k_{att} and k_{det} (Table 3.1) suggest intermediate to fast attachment to the SWI but slow detachment. This non-equilibrium interaction at the SWI is in line with the suggestions from the DLVO and extended DLVO profiles. This conclusion is further supported by the observation that saturated NP transport, with mainly NP-SWI interactions, can be described solely with an attachment-detachment kinetics (e.g., [13]). In some cases, experimental data was described with only an attachment process (e.g., [60]) suggesting negligible detachment. The retardation term required to describe the BTCs is an added feature and has not been typically observed for saturated transport. We acknowledge few data points but we suggest that the equilibrium sorption may be linked with the AWI and its surface area (Fig. 3.4). The presence of the secondary minimum and of a repulsive energy barrier (Fig. 3.3b) supports this suggestion although pH = 5 presents a lower limit (9.6 kT) for irreversible sorption. For instance, Hu et al. [39] reported an irreversible sorption of citrate-coated Ag NPs to the AWI. This suggests that reversibility of attachment to the AWI is sensitive to the properties of the AWI and the Ag NPs as influenced by the solution chemistry. Therefore, the exact knowledge of these physicochemical properties for the respective experiments is required for final evidence.

3.4.4 Influence of flow regime on transport

For higher j_w and θ , a broader spectrum of pores is activated leading to much faster NP breakthrough compared to lower j_w and θ . Kumahor et al. [50] observed that dispersivity $\lambda[L]$ increased non-linearly with decreasing θ . This was interpreted as a change in the geometry of the flow field when θ is reduced. This is characterized

TABLE 3.1: Model parameters obtained from 1-D convection–dispersion and reaction model for citrate-coated Ag NPs and calculated mass balance from NP transport experiments; the model accounts for time and depth straining. The parameters j_w , v , β , $S_{np,max}/C_0$, k_{att} , k_{det} and R are flow rate, pore–water velocity, shape factor, normalized maximal attainable amount of NPs attached, attachment coefficient, detachment coefficient, and retardation factor respectively. The mass of NPs adsorbed and mobilized through the column is expressed as fraction of the total applied mass [%]. The experiment conducted at pH = 5 and $j_w = 2.4 \text{ cm h}^{-1}$ could not be fitted due to almost complete retention within the column.

j_w	v	pH	$S_{np,max}$	k_{att}	k_{det}	β	R	<i>Mass balance</i>	r^2		
cm h ⁻¹	h ⁻¹	[-]	L g ⁻¹	h ⁻¹	h ⁻¹	[-]	[-]	<i>Solid</i> <i>Aqueous</i> <i>Total</i>	[-]		
								%			
2.4	14.1	5	–	–	–	–	–	111.6	0.01	147	–
2.4	14.1	9	2.176	314187.9	0.014	1.88	3.44	70.0	0.5	127.2	0.989
9.7	33.4	5	4.415	3162.8	0.014	1.47	2.46	50.7	56.2	98.5	0.997
9.7	33.4	9	1.234	1082.2	0.015	1.22	2.65	22.5	67.3	119.9	0.999
17	48.6	5	2.468	984.2	0.000	1.03	1.48	28.6	55.3	84.3	0.964
17	48.6	9	0.194	102.2	0.038	0.84	1.58	4.6	91.0	114.3	0.994

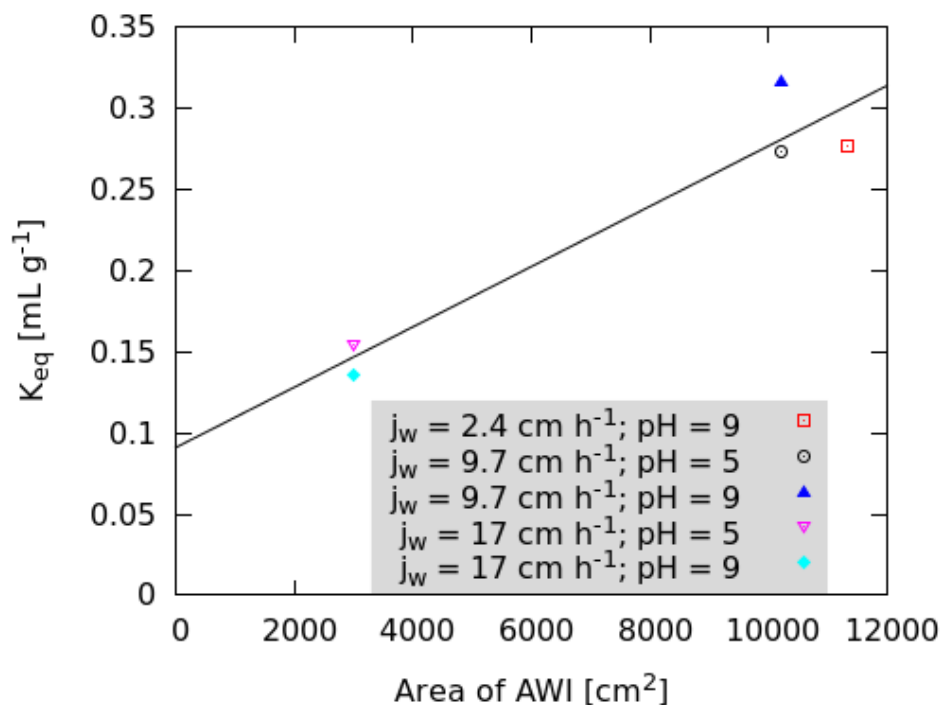


FIGURE 3.4: Equilibrium sorption coefficient (K_{eq}) as a function of area of the air–water interface (AWI).

by an increased proportion of hardly accessible regions connected to the main flow paths via bottle necks of low hydraulic conductivity [50]. We hypothesize that within such flow regimes, water film straining should be significant and this is reflected by the increased NP retention with decreased j_w and θ . This is further supported by the h_d/d_p of about 0.005 or greater for $j_w = 2.4 \text{ cm}^{-1}$ and this value is greater than the critical h_d/d_p reported for straining to be a relevant transport process [13].

After the main breakthrough, Ag NPs concentrations start to oscillate (Figs. 3.5–3.7) for the higher flow rates ($j_w = 9.7 \text{ cm h}^{-1}$ and 17.0 cm h^{-1}). Such oscillations were also observed by others (e.g., [47, 73]) but no plausible explanation has been suggested so far. Based on a joint evaluation of the hydraulic state variables measured during our experiments (Fig. 3.2), these oscillations have to be considered as real features and not artifacts of the experimental setup. The attachment and detachment model (e.g., [89]) could not describe this phenomenon. Furthermore, the optimized k_{det} which ranges between 0 and 0.038 h^{-1} (Table 3.1) can be neglected at least in our study. Further research is therefore needed to unravel the reasons for this phenomenon.

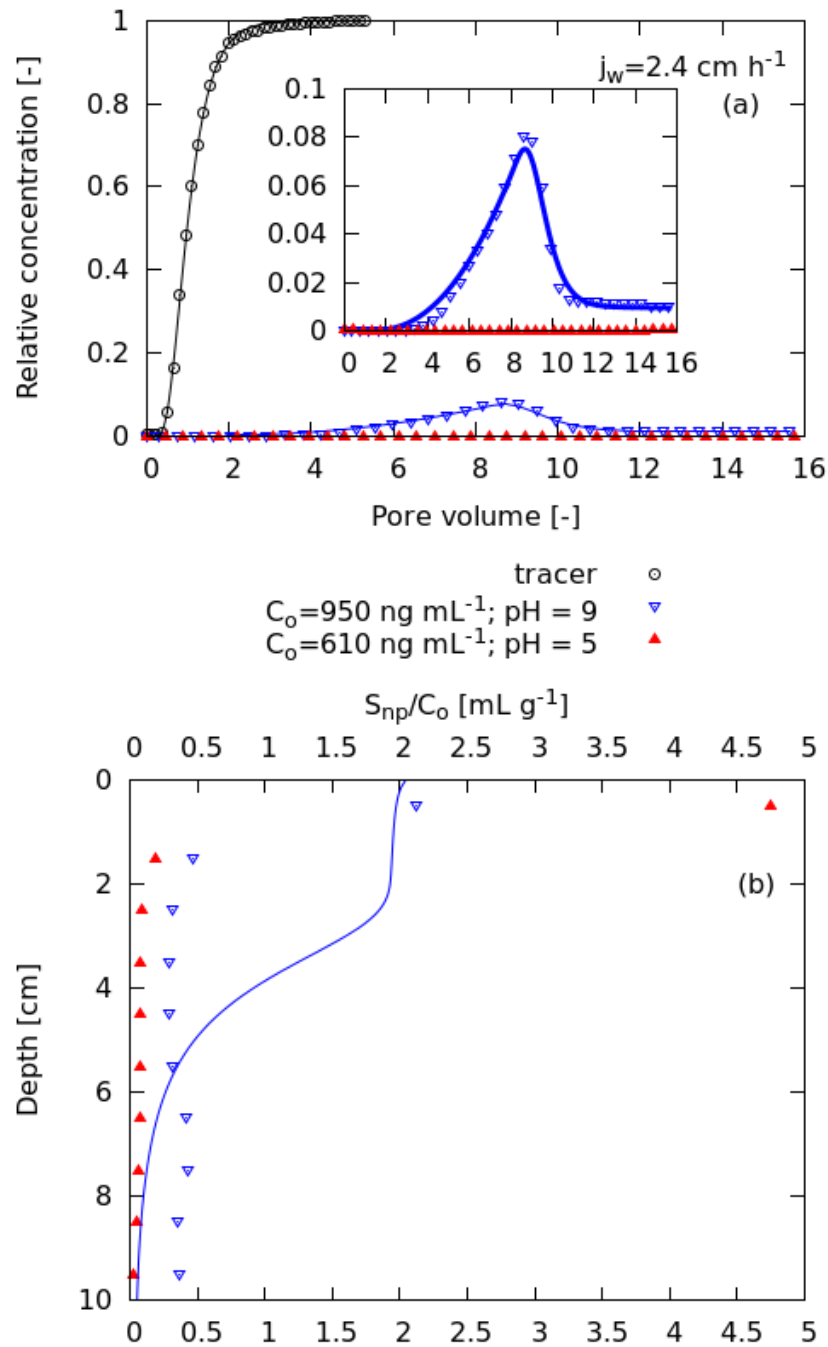


FIGURE 3.5: Experiment breakthrough curves, BTCs (a) and retention profiles, RP (b) for citrate-coated Ag nanoparticles, NPs ($j_w = 2.4 \text{ cm h}^{-1}$; pH = 5 and pH = 9). The symbols and lines represent experimental outcomes and model results respectively. The result of tracer experiment [50] are shown in black symbols (experiment) and line (model result) for $j_w = 2.4 \text{ cm h}^{-1}$. The dispersion coefficient, $D_{eff} = 14.15 \text{ cm}^2 \text{ h}^{-1}$ for $j_w = 2.4 \text{ cm h}^{-1}$, of the tracer experiment was fixed for NP parameter estimation. The inset Figure zooms in on the shape of NP BTCs.

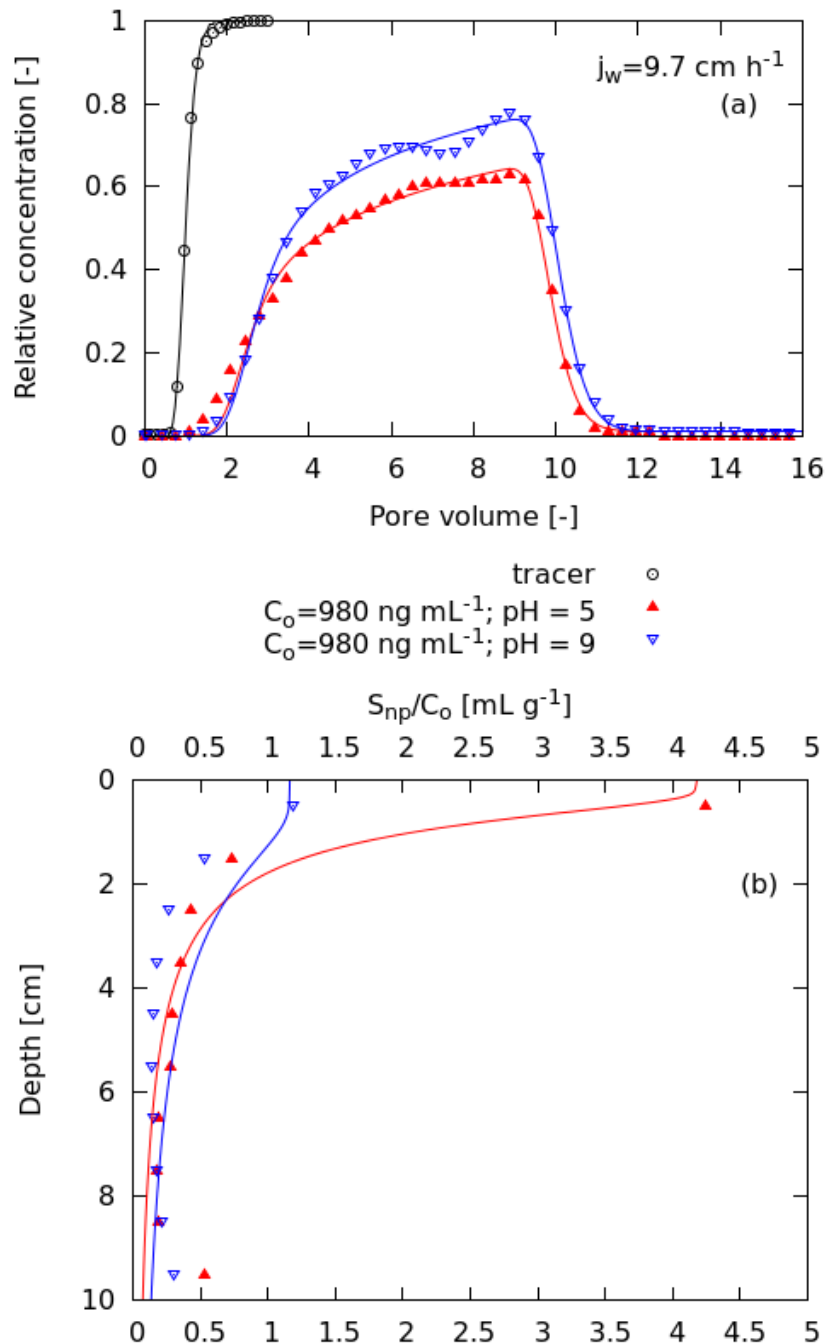


FIGURE 3.6: Experiment breakthrough curves, BTCs (a) and retention profiles, RP (b) for citrate-coated Ag nanoparticles, NPs ($j_w = 9.7 \text{ cm h}^{-1}$; pH = 5 and pH = 9). The symbols and lines represent experimental outcomes and model results respectively. The result of tracer experiment [50] is shown in black symbols (experiment) and line (model result) for $j_w = 9.7 \text{ cm h}^{-1}$. The dispersion coefficient, $D_{eff} = 6.95 \text{ cm}^2 \text{ h}^{-1}$ for $j_w = 9.7 \text{ cm h}^{-1}$, of the tracer experiment was fixed for NP parameter estimation.

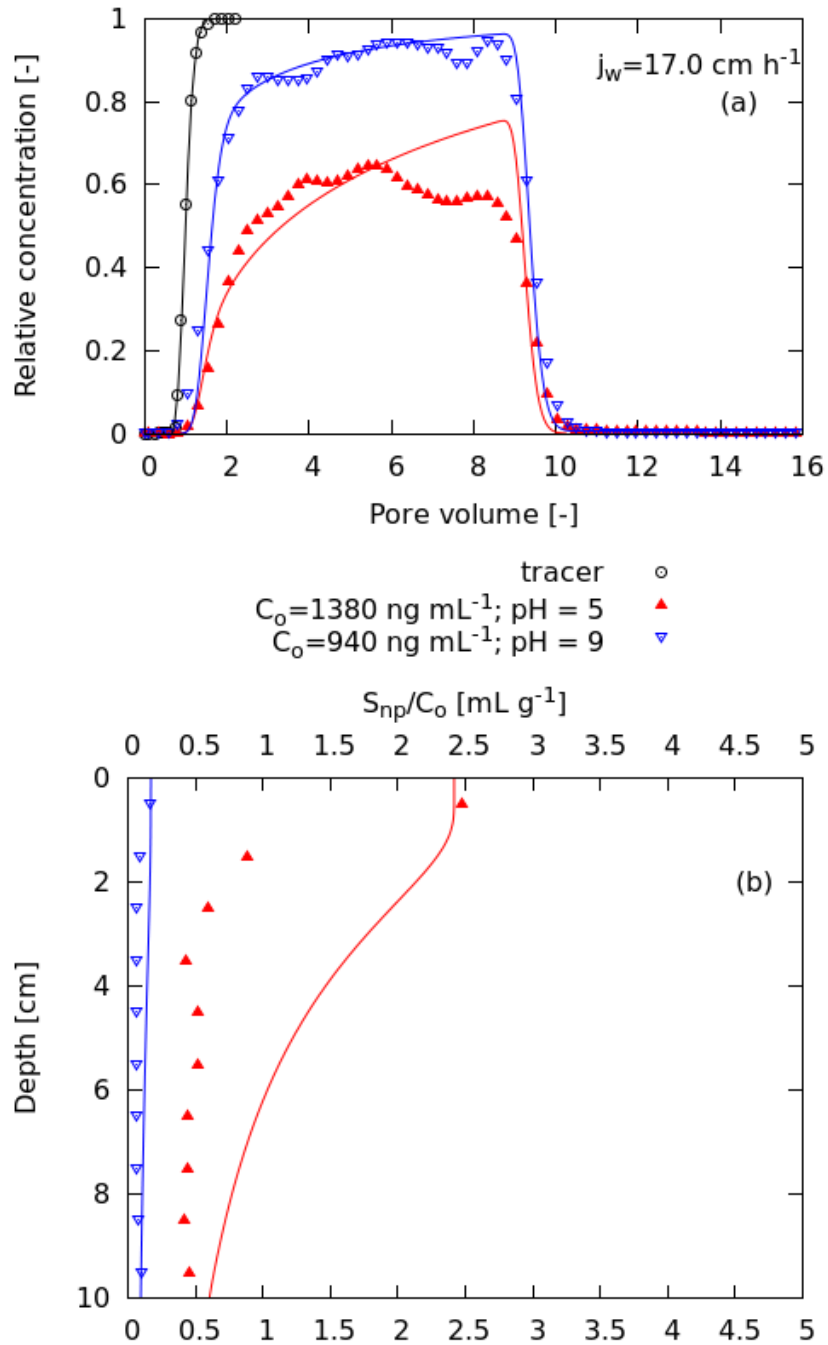


FIGURE 3.7: Experiment breakthrough curves, BTCs (a) and retention profiles, RP (b) for citrate-coated Ag nanoparticles, NPs ($j_w = 17 \text{ cm h}^{-1}$; pH = 5 and pH = 9). The symbols and lines represent experimental outcomes and model results respectively. The result of tracer experiment [50] is shown in black symbols (experiment) and line (model result) for $j_w = 17 \text{ cm h}^{-1}$. The dispersion coefficient, $D_{eff} = 6.48 \text{ cm}^2 \text{ h}^{-1}$ for $j_w = 17 \text{ cm h}^{-1}$, of the tracer experiment was fixed for NP parameter estimation.

3.4.5 Effect of surface charge on transport

Mobility increased with j_w and θ and a generally lower NP breakthrough was observed at pH = 5 compared to pH = 9 for a given j_w and θ (Table 3.1). This goes along with a less negative ζ potential value (Fig. A.1) and a resulting reduced colloidal stability of the Ag NPs. At pH = 5, the carboxylic groups of citrate may protonate and this is expected to decrease the collector–NP repulsive forces. We therefore expect greater retention at pH = 5 compared to pH = 9. This suggests that physical constraints (e.g., equivalent pore radius, hydrodynamic drag, geometry of flow field and hd of the Ag NPs) and chemical factors (e.g., pH and surface charge) may be coupled during transport as suggested by Chen and Flury [16].

3.4.6 Retention profiles

The prognosis of the DLVO theory is unfavorable conditions for deposition onto the collectors (Fig. 3.3). However, maximum retention was observed close to the column surface (Figs. 3.5–3.7). For much larger colloids than used in our study, retention was also observed under unfavorable conditions and straining was suggested to be a dominant mechanism (e.g., [14, 89]). Our model parameterization could mimic the influence of j_w and θ on the NP transport given by a higher k_{att} for lower j_w and θ for a given pH level. Also, the greater k_{att} obtained at pH = 5 compared to pH = 9 is consistent with the lower repulsive electrostatic interactions at pH = 5. Hence, the model concept is sensitive to the investigated flow dynamics and the delineated chemical boundaries. The magnitude of NPs retained at the column surface is highly sensitive to j_w and pH. This ranges from almost no retention for the highest j_w at pH = 9 to almost complete retention for the lowest j_w at pH = 5 (Figs. 3.5–3.7). This suggests that flow dynamics and chemical forces are coupled to determine the shape of the RPs. It is however noted that filtration theory is not always valid for deposition under unfavorable conditions ([92]) and probably unable to mimic coupled physical and chemical processes.

The NPs were delivered onto the column surface via 19 hypodermic needles as uniformly distributed droplets into a partly saturated sand and we assume uniformity in flux density of water and NP application concentration over the column surface. Within the first few millimeters close to the column surface (referred to as “critical zone”), the input suspension is distributed within the water filled pore

space and this depends on j_w and θ . During this transition, some NPs may partly be strained depending on charge or pH and the local geometry of the flow field while others are released to efficient flow paths. This is another piece of evidence that physical constraints and chemical factors may be coupled during straining. We suggest that some NPs made it across the energy barrier and this tendency is much higher at pH = 5 due to the reduced repulsive electrostatic interactions (Fig. 3.3) while another group of NPs was held weakly. The weakly held NPs could be dislodged when the suspension load was decreased (e.g., application of NP-free background electrolyte solution) or when a higher hydrodynamic drag is applied or the net charge is altered.

3.5 Conclusion

The transport of citrate-coated Ag NPs has been investigated in unsaturated sand. For the established chemical conditions, the BTCs and their corresponding RPs suggest non-equilibrium interaction at the SWI. Attachment is pronounced close to the column surface where the particles enter the flow field and much less further along the flow path. Additionally, a reversible attachment process described as equilibrium sorption led to NP retardation and is attributed to the AWI. Thus, the BTCs could be modeled based on interaction kinetics far from equilibrium in combination with an effective retardation factor. The NPs will generally not sorb onto the AWI considering the classic DLVO interaction. However, the DLVO model augmented for hydrophobic interaction suggests unfavorable attachment conditions and a secondary minimum at the AWI. Therefore, the equilibrium process is related to θ and herewith to the area of the AWI. The non-equilibrium process attributed to the SWI has been observed by others under water saturated conditions. The retardation observed in this study seems to be an additional feature of unsaturated transport explained by the presence of AWI. Our model concept can be extended to natural soil where NOM coatings may render the Ag NPs more hydrophobic and the AWI more negative.

Chapter 4

Transport of soil-aged silver nanoparticles in unsaturated sand

4.1 Abstract

Engineered nanoparticles released into soils may be coated with humic substances, potentially modifying their surface properties. Due to their amphiphilic nature, humic coating is expected to affect interaction of nanoparticle at the air–water interface. In this study, we explored the roles of the air–water interface and solid–water interface as potential sites for nanoparticle attachment and the importance of hydrophobic interactions for nanoparticle attachment at the air–water interface. By exposing Ag nanoparticles to soil solution extracted from the upper soil horizon of a floodplain soil, the mobility of the resulting “soil-aged” Ag nanoparticles was investigated and compared with the mobility of citrate-coated Ag nanoparticles as investigated in an earlier study. The mobility was determined as a function of hydrologic conditions and solution chemistry using column breakthrough curves and numerical modeling. Specifically, we compared the mobility of both types of nanoparticles for different unsaturated flow conditions and for pH = 5 and pH = 9. The soil-aged Ag NP were less mobile at pH = 5 than at pH = 9 due to lower electrostatic repulsion at pH = 5 for both types of interfaces. Moreover, the physical flow field at different water contents modified the impact of chemical forces at the solid–water interface. An extended Derjaguin–Landau–Verwey–Overbeek

This chapter has been submitted to Elsevier Journal of Contaminant Hydrology: Kumahor, S.K., P. Hron, G. Metreveli, G. E. Schaumann, S. Klitzke, F. Lang, H.–J. Vogel. 2016. Transport of soil-aged silver nanoparticles in unsaturated sand.

(eDLVO) model did not provide satisfactory explanation of the observed transport phenomena unlike for the citrate-coated case. For instance, the eDLVO model assuming sphere-plate geometry predicts a high energy barrier ($> 90 kT$) for the solid-water interface, indicating that nanoparticle attachment is less likely. Furthermore, retardation through reversible sorption at the air-water interface was probably less relevant for soil-aged nanoparticles than for citrate-coated nanoparticles. An additional cation bridging mechanism and straining within the flow field may have enhanced nanoparticle retention at the solid-water interface. The results indicate that the mobility of engineered Ag nanoparticles is sensitive to solution chemistry, especially pH and the concentration of multivalent cations, and to the unsaturated flow conditions influencing particle interaction at biogeochemical interfaces.

Keywords: Unsaturated transport, water dynamics, cation bridging, amphiphilic, eDLVO.

4.2 Introduction

Exposure of the derivatives of nanotechnology to the environment is burgeoning [1, 40]. Examining the fate of engineered nanoparticles (NPs) is therefore useful to formulate strategies to protect the environment. Upon release to the environment, the mobility of engineered NPs will depend on their properties and on their interactions with the host media, which are strongly influenced by host media properties. In soils and surface waters for instance, humic substances may coat engineered NPs, potentially impacting their stability [3, 5], mobility (e.g., [46]) and toxicity [80, 81]. Hydrodynamic diameter, h_d [L], of NPs and wettability and surface charge of both NPs and pore surfaces [43] are properties that may alter upon organic matter (OM) sorption. Stability of NPs in aqueous solution due to electrostatic and steric effects of OM may depend on the interplay among: (i) dissolved OM content [110], (ii) ionic strength [5, 28], (iii) cation valence [40, 65], (iv) anion composition [112], (v) pH [28], (vi) concentration of NPs [8, 65] and (vii) exposure time [10, 28, 49]. For instance, high ionic strength destabilizes and lowers mobility of NPs [32] via compression of the electric double layer (EDL). High concentration of multivalent cations (e.g., Ca^{2+} and Mg^{2+}) may oppose the electrostatic and steric effects of OM on NPs via cation bridging complexation and flocculation [69]. Furthermore, reduced electrostatic and steric effects of OM on

NPs can result from lowering pH [91], which may lead to coiling of OM structure. All these possible effects of OM coating on surface properties and stability are supposed to be relevant for the transport of NPs in porous media. The impact of humic substances on transport has been investigated extensively for saturated porous media, whereas much less is known about the impact of soil-borne OM on unsaturated transport.

Besides the properties of NPs, solution chemistry controls particle transport [32, 82]. For example, increase in ionic strength from 1 to 50 mM significantly enhanced the retention of TiO₂ NPs for both saturated and unsaturated transport in sand, and this was attributed to aggregation of NPs and enhanced straining [32]. The relation of h_d [L], to pore diameter, d_p [L], and/or water film thickness, W_f [L], is expected to be relevant for straining [15]. Thus, above a critical threshold for h_d/d_p enhanced straining was observed (e.g., [15]). The ratio, h_d/d_p , has been found in the range between 0.002 and 0.2 [15, 58, 82]. Shen et al. [82] noted that variation in ionic strength may account for this range explainable by an additional straining induced via compression of the EDL at high ionic strength. Aggregation of NPs and subsequent increase in h_d/d_p [28, 49] is, thus, expected to enhance straining. For unsaturated flow, the thickness of water film may decrease to the size range of h_d [11], which might render straining relevant [77]. Overall, the colloidal state of NPs, the structure of pores and the surface properties of collectors (i.e., air-water, AWI and solid-water interfaces, SWI) formed during unsaturated flow govern the mobility of NPs [51]. These complex interactions have not yet been explored sufficiently to predict transport of NPs in unsaturated soil.

Another aspect to consider for transport is the influence of degree of hydrophobicity of NPs in relation to the properties of collectors. For example, Wan and Wilson [104, 105] observed that hydrophobic latex particles showed reduced mobility with increase in air content in repacked glass beads compared to hydrophilic latex particles. This was attributed to the enhanced interaction of the latex particle at the AWI. Based on an extended Derjaguin-Landau-Verwey-Overbeek (eDLVO) analysis, Kumahor et al. [51] also found that citrate-coated Ag NPs attached reversibly to the AWI for unsaturated flow in sand. However, the eDLVO (accounting for hydrophobic interaction) calculations showed that an energy barrier and the relevance of a secondary minimum in the attachment profile strongly depend on the water contact angle of the NPs. Consequently, small changes in the water contact angle of the NPs can induce a change from reversible to irreversible

attachment or render attachment improbable [51]. Therefore, it is still open as to what extent and by which type of attachment Ag NPs coated with other organic matter will interact with the AWI interface and how this will affect their transport in unsaturated porous media.

In this work, transport of soil-aged Ag NPs in unsaturated sand was studied with focus on the combined effects of divalent cations, pH, soil-borne dissolved OM and hydraulic states. The latter is related to the chosen unsaturated flow rate, j_w [LT^{-1}] leading to different water contents, θ [-] and pressure heads, h_m [L]. Measured breakthrough curves (BTCs) of the soil-aged Ag NPs were used to validate a model based on the classical convection–dispersion (CD) approach accounting for different interaction mechanisms at the AWI (i.e., reversible sorption) and the SWI (i.e., irreversible sorption) as proposed by Kumahor et al. [51]. We further explored to what extent the results are in accordance with the eDLVO model for the given experimental conditions in terms of hydraulic states, aqueous chemistry and pore structure.

4.3 Materials and methods

4.3.1 Aging of Ag nanoparticle in soil solution

The procedure for the aging of the Ag NPs in soil solution was modified according to Klitzke et al. [49]. In summary, disturbed soil obtained from the upper horizon of a floodplain soil (Rhine valley near Leimersheim, Germany) was wet sieved to obtain < 2 mm fraction and stored field-moist at 4 °C. The sieved soil was equilibrated in deionized water at a gravimetric solid-to-solution ratio of 1:10 by shaking at 20 revolutions per minute (rpm) using an end-over-end shaker (GFL 3040) for 16 h and subsequently filtered over a 1.2 μm cellulose nitrate membrane (Sartorius, Type 11303). The filtrate was ultra-centrifuged at 132750 g for 4 h to minimize the formation of heteroaggregates between Ag NPs and soil colloids by removing soil-borne colloids larger than 16 nm. Calcium was the dominant cation of the watery extract from the floodplain soil (61 mg Ca L^{-1} , [49]). The citrate-coated Ag NPs were synthesized in AgNO_3 and trisodium citrate solution at 100 °C and pH = 11 using citrate reduction method (refer to Metreveli et al. [65] for synthesis procedure). Then, 100 mg L^{-1} dispersion of citrate-coated Ag NPs with

primary particle size of about 40 nm was mixed with the soil solution to obtain a concentration of about 5 mg L⁻¹. The resulting dispersion was shaken at 20 rpm for 24 h and thereafter referred to as soil-aged. The dispersion was then diluted with deionized water to attain about 1 mg L⁻¹ concentration and the pH adjusted to either pH = 5 (using 65 % HNO₃; Suprapur, MERCK) or pH = 9 (using NaOH; pure, MERCK) for the transport experiments.

4.3.2 Porous media and transport experiments

This study follows up on an earlier study on transport of citrate-coated Ag NPs [51]. The same porous media, i.e., quartz sand with 0.1–0.3 mm grain size distribution and bulk density, ρ_b [ML⁻³] of 1.52 g cm⁻³, was used. The experimental column (diam.: 16.2 cm and depth: 10 cm) was preconditioned by percolating 5 pore volumes (PV) of soil solution free of NPs (i.e., the same soil solution as previously used to “age” the NPs) at the same j_w as applied in the subsequent experiment. The solution was adjusted to either pH = 5 or pH = 9. For each j_w (Table 4.1, quasi-steady state and gravity flow conditions were established to ensure that h_m and θ were constant along the length of the column (Fig. B.1). Without changing the flow conditions, about 8 PV of soil-aged Ag NPs dispersion were infiltrated. The transport experiment was finished by infiltration of soil solution free of Ag NPs (adjusted to either pH = 5 or pH = 9). After the transport experiments, retention profiles (RPs) were measured following a procedure detailed in Kumahor et al. [51]. The BTCs and RPs were integrated to establish a mass balance. In total, six transport experiments at two different pH values and three different flow rates were conducted (Table 4.1). The experiments were not replicated since the porous media is well defined and macroscopically homogeneous. In this case, the different physical and chemical conditions explored for the identical porous media should provide a solid basis for a consistent interpretation of the results.

4.3.3 Characterization of the flow field

A decrease in j_w results in a decrease in θ of the porous medium. Consequently, the structure of the microscopic velocity field changes, since water flow is restricted to

TABLE 4.1: Description of the soil-aged Ag NPs transport experiments conducted at the various flow rates (j_w) corresponding to the measured water contents (θ) and pH values. The experiments, Exp1 and Exp2, have slightly different flow rates and this could be captured because the specified (based on pump calibration) and actual (obtained from balance reading) flow rates were monitored.

<i>Experiments</i>	j_w [cm h ⁻¹]	pH [-]	θ [-]
Exp1	2.7	5	0.17
Exp2	2.4	9	0.17
Exp3	9.7	5	0.29
Exp4	9.7	9	0.29
Exp5	17	5	0.35
Exp6	17	9	0.35

smaller pores and the total area of the AWI increases when starting from flow conditions close to water saturation. Both aspects are deemed relevant for macroscopic transport. The 3-D pore structure of the material (quartz sand) was obtained using X-ray micro-tomography (X-Tek HMX 225), and the distribution of water and air was calculated at the pore scale for different pressure heads as measured during the experiments. This was done based on the Young-Laplace-Equation relating h_m to the curvature of the AWI as detailed in Kumahor et al. [51]. This approach provides an estimation of the total extent of AWI as potential collector surface during unsaturated flow conditions.

4.3.4 Characterization of pore-water chemistry

Pore-water composition (Table B.2) was determined in column eluates sampled between the 7th and 8th PV. Major cations (Ca^{2+} , Mg^{2+} , K^+ , and Na^+) and anions (Cl^- , SO_4^{2-} , NO_3^-) were determined using ion chromatography (881 Compact IC pro, Metrohm), whereas dissolved organic carbon (OC) (particles $> 0.1 \mu\text{m}$ were filtered out) was determined using TOC analyzer (multi N/C 2100, Analytik Jena AG).

4.3.5 Hydrodynamic diameter, zeta potential and interfacial interaction energy

The hydrodynamic diameter (h_d) and zeta (ζ) potential of the soil-aged Ag NPs were measured at pH = 5 and pH = 9 according to Kumahor et al. [51]. The measurements were made in soil extract with 5 mg L⁻¹ soil-aged Ag NPs. The interaction energy profiles between soil-aged Ag NPs and collectors were calculated based on the eDLVO model as shown in the supplementary information (Appendix B).

4.3.6 Model formulation

A model concept proposed for transport of citrate-coated Ag NPs in unsaturated sand [51] was used to evaluate the soil-aged Ag NPs BTCs. This model concept considers two collector types: one with a reversible interaction in equilibration with the solution (supposed to be applicable to AWI) and another one characterized by an irreversible interaction far from equilibrium (supposed to be applicable to SWI). The model is based on 1-D form of the convection–dispersion (CD) and reaction equation:

$$\frac{\partial \theta RC}{\partial t} = \theta D_{eff} \frac{\partial^2 C}{\partial z^2} - j_w \frac{\partial C}{\partial z} - \rho_b \frac{\partial S_{np}}{\partial t} \quad (4.1)$$

where C [ML⁻³] is the concentration of NPs in the aqueous phase, D_{eff} [L²T⁻¹] is the effective dispersion coefficient, z [L] is the travel distance, t [T] is the time and S_{np} [-] is the amount of attached NPs to the solid phase. For the special case of linear sorption [1, 51], the retardation factor (R) [-] of the soil-aged Ag NPs relates to an equilibrium sorption coefficient (K_{eq}) [L³M⁻¹]:

$$R = 1 + \frac{\rho_b K_{eq}}{\theta} \quad (4.2)$$

where $K_{eq} = S_{np}^e / C$ and S_{np}^e is the amount of soil-aged Ag NPs sorbed under equilibrium condition. The reaction term, the last term on the right hand side of equation (4.1), describes the dynamics of attachment and detachment and here-with accounts for the non-equilibrium mass transfer between the aqueous phase and the SWI:

$$\rho_b \frac{\partial S_{np}}{\partial t} = \theta k_{att} \psi C - \rho_b k_{det} S_{np} \quad (4.3)$$

where k_{att} [T^{-1}] is the attachment coefficient and k_{det} [T^{-1}] is the detachment coefficient. Equation (4.3) incorporates a dimensionless time and depth dependent straining function, ψ [-]:

$$\psi = \left(1 - \frac{S_{np}}{S_{np,max}} \right) \left(\frac{d_{50} + z}{d_{50}} \right)^{-\beta} \quad (4.4)$$

where d_{50} [L] is the mean grain diameter, $S_{np,max}$ [-] is the maximal attainable amount of soil-aged Ag NPs attached for given chemical and hydrologic boundaries and β [-] is a shape factor for retention along the flow path. The first and second terms on the right hand side of equation (4.4) correspond to the temporal dynamics and depth dependent retention of soil-aged Ag NPs at the SWI respectively [60, 89]. While β values of 0.432 and 1.532 were considered for sand [60, 89] and undisturbed loamy sand soil [59] respectively, Kumahor et al. [51]) optimized β for the transport of citrate-coated Ag NPs in sand since the measured RPs show sensitivity to j_w and pH.

4.3.7 Parameter estimation

The model was parameterized as described by Kumahor et al. [51]. Thus, j_w (flux boundary condition) and θ (measured using a balance) were directly obtained from the transport experiments, D_{eff} was obtained by fitting a 1-D analytical solution of the CD model to tracer BTCs [50] and $S_{np,max}$ was obtained from the measured RPs. Additionally, we allowed flexibility in $S_{np,max}$ and reoptimized one of the experiments of Kumahor et al. [51] conducted at $j_w = 17 \text{ cm h}^{-1}$ and $\text{pH} = 5$ to improve the prediction of RPs. The remaining parameters k_{att} , k_{det} , R and β were obtained via parameter estimation [51]. The 1-D model domain (10 cm in length) was discretized into 512 elements following a cell-centered finite volume scheme [38] and the last element taken as outflow concentration in each time step.

4.4 Results and discussion

4.4.1 Porous media properties and hydraulic state during transport

The hydraulic states (i.e., j_w , θ and h_m) for the different unsaturated flow conditions are shown in Figure B.1. For each j_w , θ and h_m were stable within a narrow range such that the structure of the flow field is expected to be the same along the entire flow path. The structure of the flow field and extent of the AWI at different flow rates were reported by Kumahor et al. [51]. Considering a ρ_b of 1.52 g cm^{-3} (packing density) and a particle density (ρ_s) of 2.65 g cm^{-3} for mineral soils, a total porosity of 0.42 (volume basis) was obtained which was in good agreement with the porosity from structure analysis (Fig. B.2). The proportion of water-filled pores decreased with θ (Figs. B.1 and B.2) and the total area of AWI is expected to increase as j_w and θ decreased. Kumahor et al. [50] found for the same material and similar flow rates that dispersivity, $\lambda(\theta)$ [L], of inert solute increased as θ decreased. This was explained by the geometry of the water phase forming an increasing contrast between well connected pathways and more isolated clusters connected via water films or regions of relatively low hydraulic conductivity. This was observed to impact the transport of citrate-coated Ag NPs at low j_w and θ [51] and we expect that this situation generally reduces the mobility of NPs.

4.4.2 Properties of nanoparticles

In Table 4.2, the properties of soil-aged Ag NPs are compared with citrate-coated Ag NPs investigated by Kumahor et al. [51]. We expect that dissolved OM would coat the Ag NPs as observed by Klitzke et al. [49]. Lau et al. [54] also noted a possible displacement of Ag NPs capping agents by natural organic matter. In contrast to the citrate-coated Ag NPs, the soil-aged particles had a considerably larger h_d (about factor 5) and a lower ζ potential (about factor 2). This is the same for both pH values. Obviously, the soil-aged Ag NPs are more aggregated and less charged than the citrate-coated Ag NPs. The differences in hydrodynamic sizes as well as ζ potentials of soil-aged Ag NPs and citrate-coated are discussed in detail by Klitzke et al. [49]. In short, multivalent cations (Fig. 4.1) may have

TABLE 4.2: Properties of soil-aged Ag nanoparticles versus citrate-coated Ag nanoparticles.

Dispersion	Hydrodynamic diam. (h_d) [nm]		Zeta (ζ) potential [mV]	
	pH = 5	pH = 9	pH = 5	pH = 9
Soil-aged	213 ± 7	201 ± 9	-14 ± 4	-21 ± 4
Citrate-coated	48 ± 1	40 ± 1	-25 ± 4	-52 ± 2

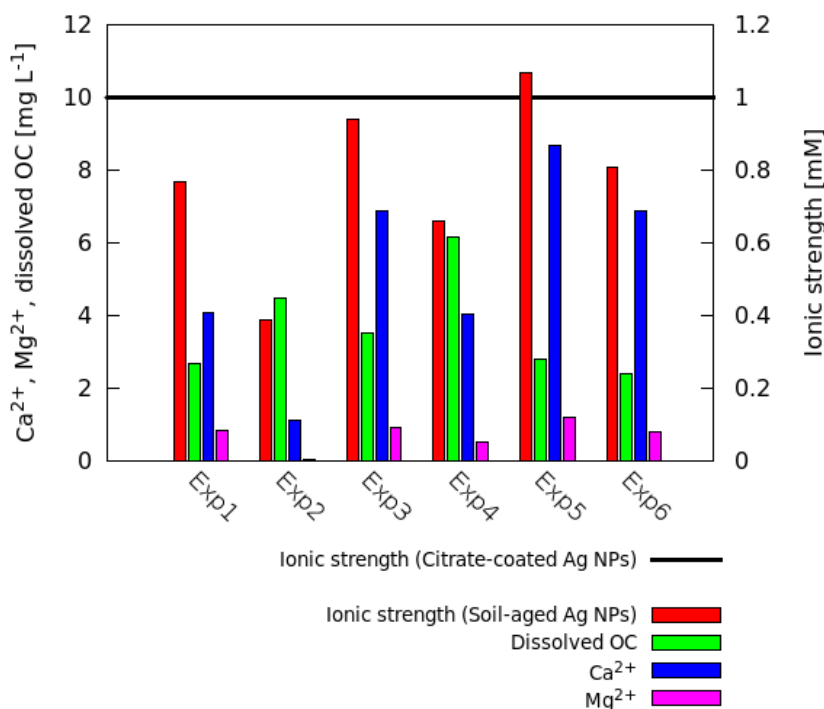


FIGURE 4.1: Dissolved organic carbon (OC) content, concentration of Ca^{2+} and Mg^{2+} and ionic strength measured in column eluate sampled between the 7th and 8th pore volume (PV). The horizontal line (in black) indicates 1 mM KNO_3 solution used as electrolyte for the citrate-coated Ag NPs transport experiments. The labels of x-axis are described in Table 4.1.

screened carboxyl and other functional groups of dissolved OM, compressed the EDL and led to less negative ζ potential values for the soil-aged Ag NPs. Further, the larger h_d of soil-aged Ag NPs suggests that aggregation of NPs progressed alongside charge screening [49]. At pH = 5, electrostatic repulsion between NPs on the one hand and collectors versus NPs on the other hand should be lower than at pH = 9 and this should further enhance aggregation and deposition. The differences in ζ potential and aggregation status are expected to result in different transport properties of soil-aged Ag NPs compared to the citrate-coated case.

4.4.3 Experimental breakthrough curves and soil-aged Ag nanoparticle transport

Figures 4.2–4.4 show observed (points) and modeled (lines) BTCs for soil-aged (this study) and citrate-coated Ag NPs [51]. Errors in mass balance derive largely from the quantification of mass sorbed to the solid phase (Table 4.3). The transport model [51] which includes both reversible and irreversible attachment sites was found to be appropriate to discriminate the observed parallel processes: (i) a shift in time of initial breakthrough as compared to tracer which suggests equilibrium sorption to one collector along the flow path and (ii) a tailing depicted as imbalanced attachment and detachment to another collector along the flow path. The shift in time and tailing are considered as equilibrium retardation and non-equilibrium retention respectively. The soil-aged Ag NPs showed lower breakthrough at pH = 5 compared to pH = 9. At the lowest j_w (2.4 cm h⁻¹) and at pH = 9, retention of soil-aged Ag NPs was lower compared to the citrate-coated case (Fig. 4.2). More retention of the soil-aged Ag NPs is however apparent for the intermediate (9.7 cm h⁻¹) and highest (17 cm h⁻¹) flow rates (Figs. 4.3–4.4). The results clearly suggest that the mobility of soil-aged particles is not only influenced by j_w but a combined effect of solution chemistry and properties of the NPs. For instance, coupling between physical and chemical processes during interaction at the SWI is depicted by comparing Exp2 (pH = 9; j_w = 2.4 cm h⁻¹; ionic strength = 0.39 mM) versus Exp5 (pH = 5; j_w = 17 cm h⁻¹; ionic strength = 1.07 mM) which both led to similar breakthrough curves. Thus, slow transport in relatively small pores at lower j_w and θ for Exp2 compared to Exp5 (Fig. B.1) was counteracted by low ionic strength (i.e., less compressed EDL) and high electrostatic repulsion, leading to reduced interaction and enhanced mobility. Contrarily, fast transport in relatively large pores at higher j_w and θ for Exp5 compared to Exp2 (Fig. B.1) was counteracted by high ionic strength (i.e., more compressed EDL) and low electrostatic repulsion, leading to efficient interaction and enhanced retention.

The sensitivity of transport to pH with considerably lower mobility at pH = 5 was similar for both types of particles. This will be elaborated further in the session on the eDLVO theory. At pH = 5 and the highest j_w (17 cm h⁻¹), the observed retardation is comparable for both particles whereas for the intermediate j_w (9.7 cm h⁻¹), the soil-aged Ag NPs were weakly retarded (Fig. 4.5). It should be noted that for the lowest j_w (2.7 cm h⁻¹) at pH = 5, no retardation value was reported

since the experiment was not modeled. Then again, at $\text{pH} = 9$ increase in the area of the AWI produced some effect for soil-aged Ag NPs at the lowest j_w (2.4 cm h^{-1}). The result suggests that the reversible attachment process is less relevant for the soil-aged Ag NPs and, given that this process is related with the AWI, this matches with the observation that the impact of the AWI on retardation is weaker for the soil-aged Ag NPs compared to the citrate-coated case. The results however, partly agree with that of Wan and Wilson [104, 105], who observed reduced mobility of hydrophobic latex particles compared to hydrophilic latex particles due to enhanced sorption of the former at the AWI. Since the soil-aged Ag NPs were still retarded compared to a tracer (Figs. 4.2–4.4), an additional process may account for the observed retardation and this requires further enquiry.

4.4.4 Retention profiles

The RPs were predicted reasonably well by the chosen model concept (Figs. 4.2–4.4). Similar to the citrate-coated case, a greater proportion of the soil-aged Ag NPs were retained close to the top of the column. Kumahor et al. [51] noted that redistribution of infiltrating droplets by capillary forces generally favored straining of NPs at the top of the column. This should be absent or less pronounced for saturated transport as observed by Wang et al. [106]. Reduced electrostatic repulsion and steric effects expected at $\text{pH} = 5$ as compared to $\text{pH} = 9$ also favoured more retention of soil-aged Ag NPs at $\text{pH} = 5$. This would be discussed in more detail in the section on eDLVO interactions. Further, slightly larger h_d at $\text{pH} = 5$ (Table 4.2) enhanced straining of NPs especially at the top of the column (Figs. 4.2–4.4). Straining becomes more enhanced at lower j_w (Figs. 4.2–4.4), thus lower θ , where transport is shifted towards smaller pores (Figs. B.1 and B.2) with shorter distances to the SWI and more time is available for diffusion and interaction. Clearly, both chemical and physical factors constrain transport.

4.4.5 Consequence of pore–water chemistry on transport

In the following sections, solution chemistry (i.e., dissolved organic carbon content, multivalent cations and ionic strength; Fig. 4.1) is discussed in relation to relevant chemical controls on transport. It should be noted that the column was flushed with 5 PV of soil solution free of NPs adjusted to either $\text{pH} = 5$ or $\text{pH} = 9$ prior to

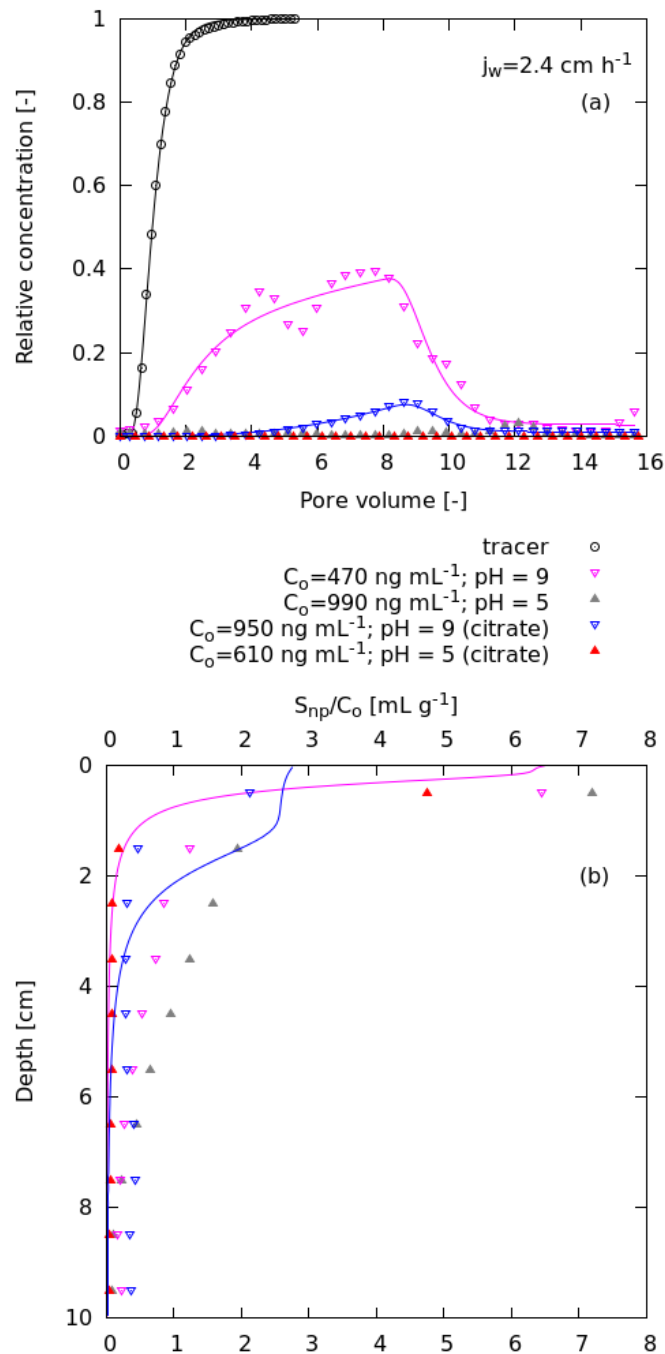


FIGURE 4.2: Experiment breakthrough curves, BTCs (a) and retention profiles, RPs (b) for soil-aged Ag nanoparticles, NP ($j_w = 2.7 \text{ cm h}^{-1}$ at pH = 5 and $j_w = 2.4 \text{ cm h}^{-1}$ at pH = 9). The symbols and lines represent experiment and model results respectively. The BTCs for soil-aged (this study) and citrate-coated Ag NPs [51] are compared. The results of the tracer experiment [50] are shown in black symbols (experiment) and line (model result) for $j_w = 2.4 \text{ cm h}^{-1}$. The dispersion coefficient, $D_{eff} = 14.15 \text{ cm}^2 \text{ h}^{-1}$ for $j_w = 2.4 \text{ cm h}^{-1}$, of the tracer experiment was fixed during parameter estimation for the soil-aged Ag NPs.

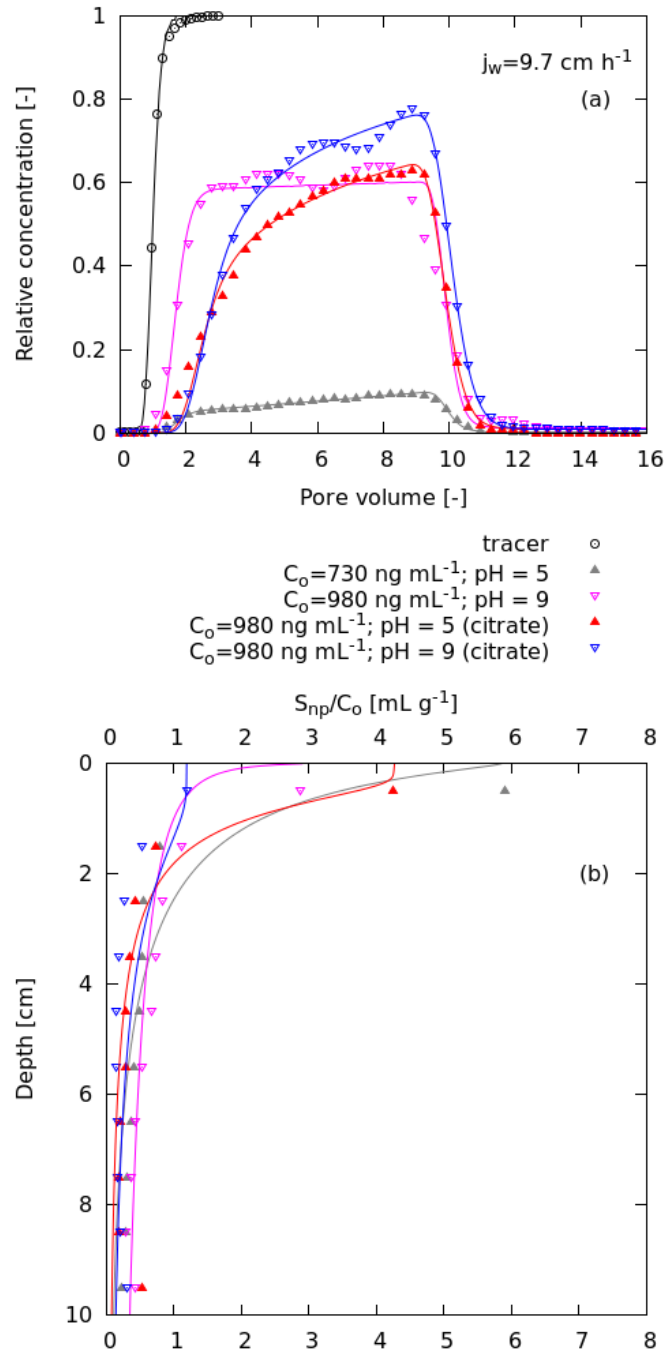


FIGURE 4.3: Experiment breakthrough curves, BTCs (a) and retention profiles, RPs (b) for soil-aged Ag nanoparticles, NP ($j_w = 9.7 \text{ cm h}^{-1}$; pH = 5 and pH = 9). The symbols and lines represent experiment and model results respectively. The BTCs for soil-aged (this study) and citrate-coated Ag NPs [51] are compared. The results of the tracer experiment [50] are shown in black symbols (experiment) and line (model result) for $j_w = 9.7 \text{ cm h}^{-1}$. The dispersion coefficient, $D_{eff} = 6.95 \text{ cm}^2 \text{ h}^{-1}$ for $j_w = 9.7 \text{ cm h}^{-1}$, of the tracer experiment was fixed during parameter estimation for the soil-aged Ag NPs.

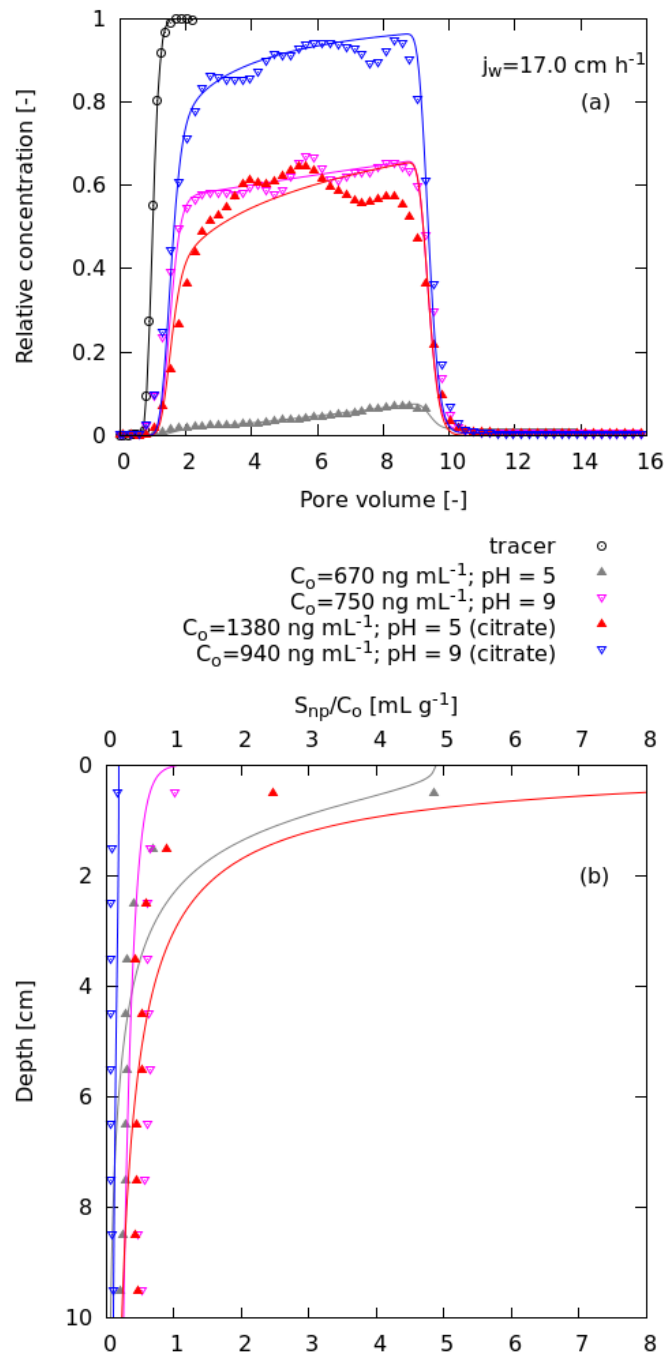


FIGURE 4.4: Experiment breakthrough curves, BTCs (a) and retention profiles, RPs (b) for soil-aged Ag nanoparticles, NPs ($j_w = 17 \text{ cm h}^{-1}$; pH = 5 and pH = 9). The symbols and lines represent experiment and model results respectively. The BTCs for soil-aged (this study) and citrate-coated Ag NPs [51] are compared. The results of the tracer experiment [50] are shown in black symbols (experiment) and line (model result) for $j_w = 17 \text{ cm h}^{-1}$. The dispersion coefficient, $D_{eff} = 6.48 \text{ cm}^2 \text{ h}^{-1}$ for $j_w = 17 \text{ cm h}^{-1}$, of the tracer experiment was fixed during parameter estimation for the soil-aged Ag NPs. The data (BTCs and RPs) for citrate-coated Ag NPs at $j_w = 17 \text{ cm h}^{-1}$ and pH = 5 were reoptimized by allowing flexibility in fitting $S_{np,max}$.

TABLE 4.3: Parameters obtained from a 1-D convection dispersion and reaction model for the soil-aged Ag NPs compared with parameter estimates for that of the citrate-coated Ag NPs (in parenthesis; obtained from Kumahor et al., [51]). The model concept accounts for retardation at the air-water interface (AWI) as well as time and depth dependent retention at the solid-water interface (SWI). Due to almost complete retention within the column, the experiment conducted at $j_w = 2.7 \text{ cm h}^{-1}$ at pH = 5 could not be modeled.

j_w	v	pH	$S_{np,max}$	k_{att}	k_{det}	β	R	Mass balance		r^2
cm h ⁻¹	cm h ⁻¹	[-]	L g ⁻¹	h ⁻¹	h ⁻¹	[-]	[-]	Solid	Aqueous	Total
								[%]		[-]
2.7(2.4) ^a	15.7(14.1)	5	–	–	–	–	–	146.8	–	–
2.4(2.4) ^b	14.1(14.1)	9	3.62(2.176)	9017.3(314187.9)	0.016(0.014)	1.74(1.88)	2.67(3.44)	123.4	–	0.983
9.7(9.7) ^c	33.4(33.4)	5	4.80(4.415)	170.1(3162.8)	0.007(0.014)	0.55(1.47)	1.96(2.46)	90.2	–	0.996
9.7(9.7) ^d	33.4(33.4)	9	3.35(1.234)	8.3(1082.2)	0.018(0.015)	0.29(1.22)	1.77(2.65)	56.6	–	0.990
17(17) ^e	48.6(46.8)	5	7.86(2.468)	734.3(984.2)	0.070(0.000)	0.71(1.03)	1.78(1.48)	64.6	–	0.973
17(17) ^f	48.6(46.8)	9	1.02(0.194)	9.0(102.2)	0.028(0.038)	0.23(0.84)	1.59(1.58)	–	–	–
17 ^g	48.6	5	2.468	1155.9	0.000	1.21	1.60	45.7	64.0	109
										0.994

^aExp1

^bExp2

^cExp3

^dExp4

^eExp5

^fExp6

^gExp5(2): Parameters reoptimized for the citrate-coated Ag NPs data (BTCs and RPs) at $j_w = 17 \text{ cm h}^{-1}$ and pH = 5 [51]. This approach used allows flexibility in determining $S_{np,max}$. The previous model parameterization [51] considers $S_{np,max}$ as the maximum attainable load of NPs at the top of the column for prescribed chemical and hydrologic boundaries ($S_{np,max}$) and this was fixed at the measured value (i.e., 2.468 mL g⁻¹)

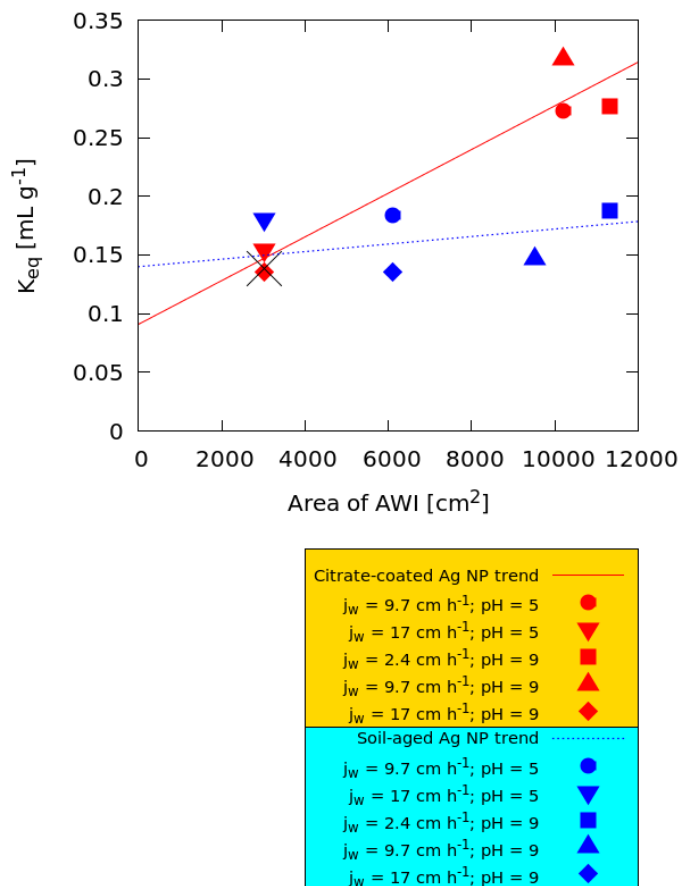


FIGURE 4.5: Equilibrium sorption coefficient (K_{eq}) of soil-aged Ag NPs versus area of the air-water interface (AWI). The red and blue points (data) and line (trend) refer to citrate-coated (Kumahor et al. [51]) and soil-aged Ag NPs (this study) respectively. The data (BTCs and RPs) for the citrate-coated Ag NPs at $j_w = 17 \text{ cm h}^{-1}$ and $\text{pH} = 5$ (refer to key) were reoptimized by allowing flexibility in fitting $S_{np,max}$ (represented as cross).

the infiltration of soil-aged Ag NPs. Therefore, the measured solution chemistry should reflect the chemical conditions for each experiment.

4.4.5.1 Dissolved organic carbon

The concentrations of dissolved organic carbon (OC) for the experiments are shown in Figure 4.1. Flushing the column with soil solution prior to the infiltration of the soil-aged Ag NPs may coat pore surfaces with OM, a situation that has been reported to favor deposition of NPs in the presence of Ca^{2+} [52]. Dissolved OM is also expected to coat the NPs inducing an increase of the colloidal stability of NPs due to electrostatic and steric stabilization [49]. Due to their amphiphilic property, the organic matter coated NPs are expected to interact with the AWI

in a reversible fashion as observed for citrate-coated Ag NPs [51]. However, the reversibility of sorption to the AWI due to the amphiphilic coating provided by OM is less relevant for the soil-aged Ag NPs (Fig. 4.5). It could be suggested that other factors especially the hydrodynamic size of the soil-aged Ag NPs and the area of the AWI played a role in this expected reversible attachment process. We note in passing that dissolved OM sorption onto Ag NPs presumably suppresses Ag^+ release and may stabilize or destabilize Ag NPs depending on the interplay among dissolved OM content, the concentration of Ag NPs and the concentration of divalent cations such as Ca^{2+} in solution [49].

4.4.5.2 Impact of multivalent cations and ionic strength

The influence of Ca^{2+} and Mg^{2+} (Fig. 4.1) on transport is addressed due to their valence and concentrations. Moreover, multivalent ions control ionic strength and modulate the structure of EDL more strongly than monovalent ions, thus, ions with higher valence compress the EDL more. Higher Ca^{2+} and Mg^{2+} (Fig. 4.1) concentrations and ionic strength measured at $\text{pH} = 5$ than at $\text{pH} = 9$ translate into a more compressed EDL and this partly explains the enhanced retention of NPs at $\text{pH} = 5$. Meanwhile, ionic strength is generally lower in the experiments conducted with soil-aged Ag NPs than for the citrate-coated Ag NPs (1 mM KNO_3). Additional effects are that, Ca^{2+} and Mg^{2+} may: (i) be complexed by soil-aged Ag NPs (via carboxyl groups) leading to charge screening [49], (ii) bridge soil-aged Ag NPs referred to as aggregation [49] and (iii) bridge soil-aged Ag NPs (via carboxyl groups sorbed onto NP surface) and the SWI (via carboxyl groups of dissolved OM sorbed onto pore surface) referred to as cation bridging [90]. Aggregation and bridging effects are expected in the presence of divalent cations because, part of the constituents of dissolved OM are expected to behave as charged polyelectrolytes at both $\text{pH} = 5$ and $\text{pH} = 9$ [85]. For example, Torkzaban et al. [90] found that cation bridging is absent in the presence of Na^+ in contrast to the presence of Ca^{2+} for the transport of quantum dots and carboxylate-modified latex particles in acid-treated Accusand. Cation bridging is also absent in the transport experiments conducted with the citrate-coated Ag NPs [51] since only K^+ (monovalent) ions were present in solution. Slightly higher concentration of cations measured at $\text{pH} = 5$ than at $\text{pH} = 9$ (Fig. 4.1) favored charge screening and cation bridging [49, 90] at $\text{pH} = 5$.

4.4.6 Extended DLVO energies and their controls on transport

Figure 4.6 shows eDLVO (electrostatic, van der Waals and hydrophobic energies) profiles for the interaction between the soil-aged Ag NPs and the collectors (refer to the supplemental material for details). Contact angle is a sensitive parameter for the calculation of the hydrophobic interactions [51]. To the best of our knowledge, no established methodology exists to directly measure the water contact angle of NPs. The contact angles of NPs are determined either by theoretical calculation [56] or experimentally after spreading of NPs on the AWI using aqueous solution containing 35% isopropanol [6] and this can modify the interface properties and contact angle of NPs. Therefore, the eDLVO calculations are based on a contact angle of 40° given by Hu et al. [39] for Ag NPs, as well as for slightly lower (30°) and higher (50°) values.

At the AWI, variations in water contact angle of NPs resulted in a transition from reversible to irreversible attachment (Figs. 4.6a, b, c). At pH = 5, the profiles predicted a secondary minimum at the AWI for a contact angle of 30° (Fig. 4.6a) but not for 40° (Fig. 4.6b) and 50° (Fig. 4.6c). But then at pH = 9, the profiles predicted a secondary minimum at the AWI for contact angles of 30° (Fig. 4.6a) and 40° (Fig. 4.6b) but not for 50° (Fig. 4.6c). Although the chosen contact angles were not directly measured, reversible attachment to the AWI cannot be fully excluded, especially for pH = 9. In any case, the K_{eq} values showed weak dependence on the area of the AWI especially for pH = 9 (Fig. 4.5) and hence a partial impact of AWI on the retardation of soil-aged Ag NPs is probable.

For the SWI (Figs. 4.6d, e, f), the profiles are unaffected by hydrophobic interactions. Increased protonation of the NPs and the SWI as well as higher concentration of Ca^{2+} and Mg^{2+} and ionic strength lowered the energy barrier at pH = 5 (92–96 kT at about 2 nm; Exp1, Exp3, Exp5) compared to pH = 9 (163–173 kT at about 2 nm; see Exp2, Exp4, Exp6). The energy required by the soil-aged Ag NPs to attain a primary minimum at the SWI ($> 92 kT$) is substantially higher than the energies induced by Brownian motion of the particles ($< 20 kT$) [29]. Therefore, an irreversible attachment of the soil-aged Ag NPs to the SWI seems improbable. Thus, the eDLVO profiles do not sufficiently account for the attachment of the Ag NPs to the SWI. The retention of NPs as opposed to the high eDLVO barrier at the SWI, however, agrees with Chen and Elimelech [52] who observed that in the

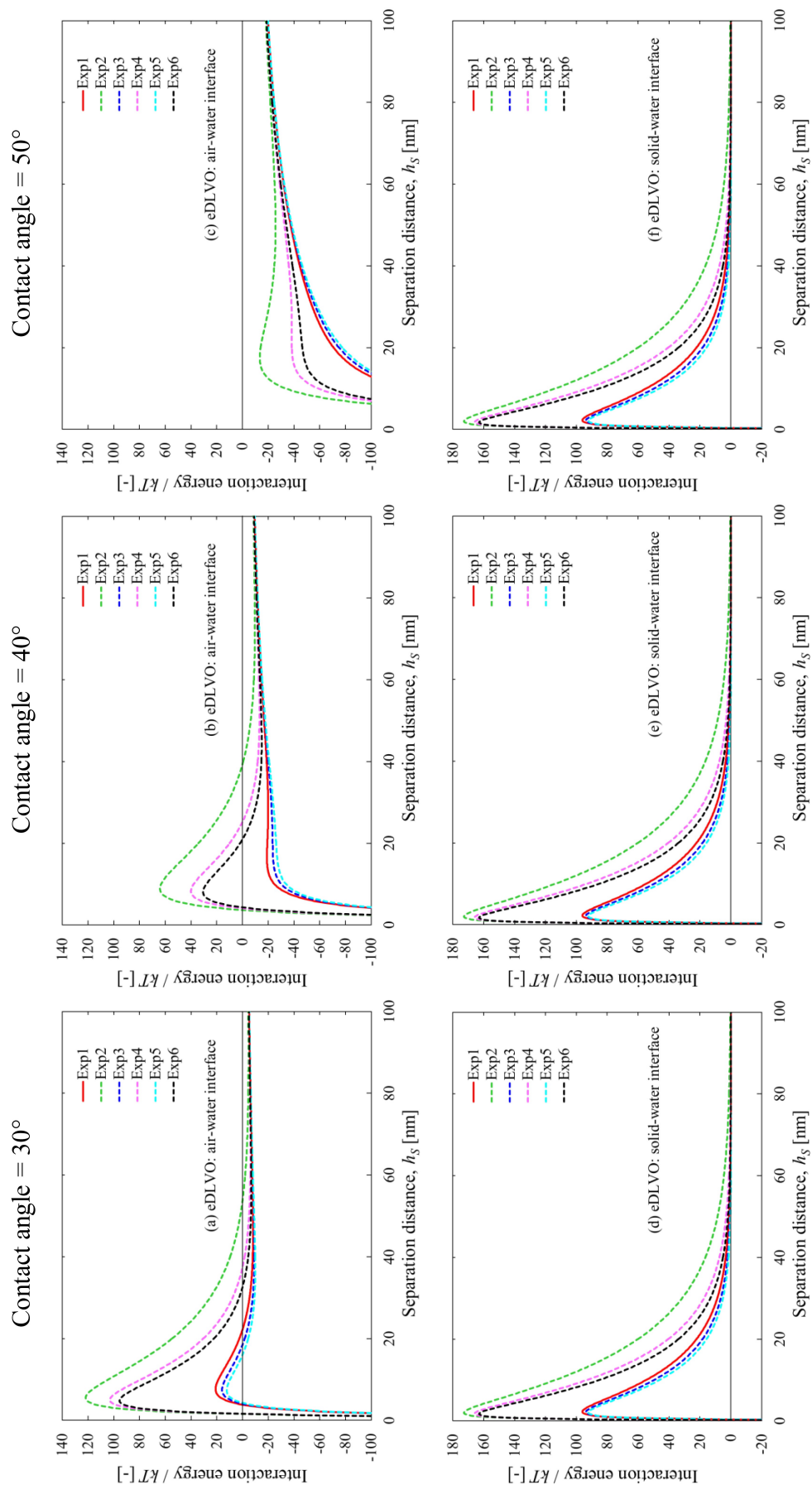


FIGURE 4.6: Dimensionless extended Derjaguin–Landau–Verwey–Overbeek (eDLVO) interaction energy profiles for soil-aged Ag NPs versus air–water interface (top Figures) and solid–water interface (bottom Figures) at pH = 5 (Exp1, Exp3, Exp5) and pH = 9 (Exp2, Exp4, Exp6). The eDLVO profiles account for hydrophobic interaction in addition to van der Waals and electrical double layer interactions.

presence of CaCl_2 , the deposition kinetics of fullerene NPs onto both humic acid- and alginate-coated surfaces are relatively high, even at relatively low (0.3 mM) Ca^{2+} concentration due to complex formation with Ca^{2+} . Therefore, the presence of the dissolved OM and multivalent cations with the soil-aged scenario could at least partly explain the larger irreversible retention component than observed for the citrate-coated Ag NPs. Additionally, the physical flow field (i.e., reduced transverse distance to the SWI and the formation of water films with decreasing θ) may have facilitated deposition via straining.

The eDLVO predictions have the following deficiencies: (i) both cation bridging and straining are not considered, (ii) the h_d values used for the calculations may be poorly estimated for aggregates by dynamic light scattering, (iii) the geometry of aggregates can be variable and therefore the assumption of sphericity and smooth surface for the NPs may not necessarily be valid (iv) the orientation of aggregated NPs which plays a role in the interaction is not succinctly accounted for and (v) there is some uncertainty in the chosen contact angles and the development of a direct method to measure water contact angle of NPs is required for validation.

4.5 Conclusion

The transport of soil-aged Ag NPs in unsaturated sand was investigated at $\text{pH} = 5$ and $\text{pH} = 9$. The experimental results could be modeled using an approach that includes equilibrium retardation at the AWI and a non-equilibrium retention at the SWI. An eDLVO analysis provides a useful module to compliment transport studies, however, great care is required with its application to the interaction of aggregated particles and in the absence of smooth surfaces and spherical geometries. In addition to straining, cation bridging is suggested to account for attachment of the NPs at the SWI. The study provides new insights into unsaturated transport of Ag NPs under variably saturated condition. Future work would be dedicated to: (i) measurement of water contact angle of NPs to validate the relevance of reversible attachment processes, (ii) characterization of the different qualities of soil-borne dissolved OM with respect to their effect on particle coating and interaction (iii) extending our knowledge on the role of capillary forces at the AWI for particle retention and (iv) studying potential release of Ag ions due to retention of Ag NPs along their transport pathways.

Chapter 5

Conclusions recommendations and outlook

5.1 Experimental concept

Based on the overarching objectives and working hypotheses stated in Chapter 1, the MS–O and MS–F approaches were used to characterize hydraulic property of sand (grain diam.: 0.1–0.3 mm) and extended for measuring tracer breakthrough curves (MS–T) within a single experimental setting. Further, the MS–T was adapted to investigate the transport of nanoparticles as a function of hydrologic and chemical factors. The MS–T establishes a constant j_w and a uniform h_m profile along an experimental column and therefore provides an ideal setup to investigate the influence of j_w on $\lambda(\theta)$. A peculiar property of the sand used in this study is its similarity to that used in water treatment systems in terms of grain size distribution. Therefore, the results of this study can be transferred to water treatment systems to reduce suspension load of nanoparticles in wastewater. The quartz sand treated of organics and oxides minerals allowed to investigate influence of air–water interface in addition to solid–water interface on transport. Morphological synthesis of X–ray CT images provided an additional module to understand how flow geometry adapts to changes in j_w and θ . Local collector (i.e., air–water interface and solid–water interface) versus nanoparticles interaction was investigated using the DLVO and extended DLVO models.

5.2 Major outcomes

For tracer transport, decrease in θ at decreasing j_w led to a non-linear increase in λ . This is linked with the divergence from continuous percolating water clusters (close to saturation) to a combination of both continuous and poorly connected water clusters with decreasing θ . The tracer breakthrough curves also suggested that $\lambda(\theta)$ might be hysteretic. Beyond a critical θ value, asymmetry in breakthrough curves is apparent and we approach the limit of applicability of the convection–dispersion model. Dispersivity values served as input data into the dispersion and reaction equation to model transport of nanoparticles.

Based on objective 1 and working hypotheses 1 and 2, the transport of citrate-coated and soil-aged Ag nanoparticles was investigated in the quartz sand used for the tracer experiments. Two observations are peculiar for both the citrate-coated and the soil-aged Ag nanoparticles breakthrough curves relative to the tracer breakthrough curves: (i) a shift in time (retardation) and (ii) reduced area under the curve (mass loss from effluent by sorption at the solid phase). The retardation is an additional feature of unsaturated transport attributed to reversible attachment at the air–water interface. Considering the classical DLVO interaction, the nanoparticles will generally not sorb onto the air–water interface. However, the eDLVO model offers a framework (thus, an energy barrier and a secondary minimum at the air–water interface) to suggest reversible attachment. The energy barrier at the solid–water interface indicates irreversible attachment when nanoparticles with sufficient thermal energy transit into the solid–water interface primary minimum. Mobility was generally reduced at pH = 5 than at pH = 9 with almost complete retention for the soil-aged Ag nanoparticles at pH = 5. Attachment was more pronounced close to the inflow boundary than further along the column for both the citrate-coated and the soil-aged Ag nanoparticles.

Based on objective 2 and working hypothesis 3, the breakthrough curves were modeled based on an interaction kinetics far from equilibrium in combination with an effective retardation factor (equilibrium process). The non-equilibrium process attributed to the solid–water interface has been observed by others under water saturated conditions. The retardation which is an added feature was modeled as equilibrium sorption at the air–water interface. This is motivated by the occurrence of an energy barrier and secondary minimum at the air–water interface. The non-equilibrium interaction is largely governed by the physical

flow field (which promotes straining) and eDLVO forces (which promotes transition of nanoparticles into the primary minimum) especially for the citrate-coated Ag nanoparticles. In this case, only nanoparticles with sufficient thermal energy could attain a primary minimum at the solid-water interface and be irreversibly attached since an energy barrier is present. An additional chemical process, cation bridging, aided attachment of the soil-aged Ag nanoparticles to the solid-water interface. The combination of hydraulic and transport data, state variables during transport, morphological analysis, DLVO and extended DLVO models provide a holistic framework towards the understanding of transport of nanoparticles in unsaturated porous media. Our modeling approach is applicable for both citrate-coated and soil-aged Ag nanoparticles given that flow is unsaturated but the eDLVO (accounting for hydrophobic interactions) analysis shows some degree of uncertainty especially for the soil-aged Ag nanoparticles.

5.3 Unsaturated transport framework

At the laboratory scale and for repacked granular porous medium, the study therefore proposes the following framework to investigate transport of dissolved chemicals or nanoparticles:

- i. Characterisation of hydraulic properties [i.e., $\theta(h_m)$ and $K(h_m)$] as a first step. Hydraulic measurements define state variables for the transport experiments and help to evaluate the impact of changing flow field due to change in θ . The MS-O and MS-F approaches, which can be performed within a single experimental setting, serve as valuable tools.
- ii. Synthesis of pore structure and the geometry of the flow field at different θ values using X-ray computer tomography and morphological analysis. This permits estimation of flow field based on morphological analysis of the pore structure (Chapter 2) and the quantification of air-water interfacial area (Chapter 3 and 4). Morphological synthesis has a limitation; it is performed at energetic minimum which is rarely achieved in nature due to hydraulic non-equilibrium.
- iii. Measurement and evaluation of tracer and nanoparticles breakthrough curves. Tracer and nanoparticles breakthrough curves can be measured using MS-T approach. The MS-T can be performed within the same setting as the

MS–O and MS–F without moving the sample (Chapter 2). For transport of nanoparticles, the termination of each experiment can be followed by further activities (i.e., quantification of sorbed nanoparticles on the solid phase) The convection–dispersion model is adequate to evaluate the tracer breakthrough curves, but, approaches the limit of applicability at low water content. Evaluating the breakthrough curves for nanoparticles requires a qualitative inspection of breakthrough trends in conjunction with hydrologic states, solution chemistry and properties of the nanoparticles as a first step to identify the appropriate process model.

- iv. Parameterization of the transport model for nanoparticles. This should be done in a way such that physical and/or chemical processes controlling transport are well reflected in the set of parameters that are considered. Examples are presented in chapters 3 and 4. Thus, (a) the parameters j_w , θ , were directly obtained from the transport experiments, (b) D_{eff} was obtained by fitting a 1–D analytical solution of the convection–dispersion model and that defines a length scale variability in velocity field, $\lambda(\theta)$ (c) the remaining parameters k_{att} , k_{det} , R and β were obtained via parameter estimation and (d) the retention profiles are predicted via forward approach and matched with the observed data. It could be noted that our model parameterization indicate sensitivity of the shape parameter, β , to the set the hydrologic and chemical conditions. This parameter is often fixed during parameter estimation. Also, flexibility in $S_{np,max}$ could be allowed to improve the prediction of the retention profiles. Further work would suffice to know how inclusion of the retention data (sorbed nanoparticles on the solid phase) in parameter estimation could improve our modeling approach.
- v. Evaluation of DLVO and eDVLO energies. This is applicable for particles that can interact at the collectors (air–water interface and solid–water interface) during transport due to difference in chemical potential. This should be informed by the properties (e.g., ζ potential, hamaker constants) of collectors and nanoparticles (e.g., ζ potential, contact angle), solution chemistry, and the nature of the breakthrough curves. This has been shown in Chapters 3 and 4. The following are however noted:
 - (a) the h_d values used for the calculations of DLVO and eDLVO energies may be poorly estimated for aggregates by dynamic light scattering.

This is especially true for the soil-aged Ag nanoparticles since they are aggregated.

- (b) for aggregated particles, their geometry can vary widely. The assumption of sphericity and smooth surface for the nanoparticles therefore requires validation,
- (c) the orientation of aggregated nanoparticles which plays a role in interaction is not succinctly accounted for and
- (d) there is some uncertainty in the chosen contact angles especially for the soil-aged nanoparticles.

5.4 Outlook

Nanomaterials are naturally present in the environment but the release of engineered forms may be unprecedented. Consequently, detailed monitoring of environmental levels is required for decision making. The aquatic-terrestrial interface is vast and cannot be adequately sampled. Column experiments may provide information on the expected residence times of nanoparticles and concentration loads for a given set of hydrologic and chemical conditions. This may provide an option for upscaling to the wider aquatic-terrestrial systems. Due to the ubiquitous presence of biogeochemical interfaces (oxides and organics) and air-water interfaces in soils, engineered Ag nanoparticles are expected to be attenuated in the environment leading to a potential release of Ag ions. This further raises environmental concerns since studies have found that ions, not particles, are more likely to make silver toxic to bacteria. The study therefore generates fundamental knowledge for decision making across science, engineering and policy interface. It also provides valuable data for mechanistic understanding of the controlling transport processes while paving way for optimizing particle properties for further applications. Further to this would be studies on: (i) whether $\lambda(\theta)$ is hysteretic, (ii) quantification of the pore-scale velocity distribution (accounting for pore connectivity and tortuosity), the surface densities of solid-water interface and air-water interface both as functions of water content. This will provide better estimates for attachment and detachment coefficients. (iii) the role of capillary forces at the air-water interface on the retention of nanoparticles, (iv) transport of nanoparticles in natural porous media, (v) discriminate the different kinds of soil-borne dissolved organic matter

and their impacts on unsaturated nanoparticle transport, (vi) the use of a pore scale model to further validate the observed transport processes and (vii) validation of specific constants (e.g., Hamaker constant) and parameters (e.g., contact angles) that were chosen from literature and how this modifies the DLVO and eDLVO profiles.

Appendix A

Supplementary data

Experimental investigation and modeling of fate and transport of citrate-coated silver nanoparticles in unsaturated sand

Samuel K. Kumahor^{1*}, Pavel Hron², George Metreveli³, Gabriele E. Schaumann³, and Hans-Jörg Vogel^{1,4}

¹Department of Soil Physics, Helmholtz Centre for Environmental Research-UFZ, Theodor-Lieser-Strasse 4, 06120 Halle-Saale, Germany.

²Interdisciplinary Center for Scientific Computing, University of Heidelberg, Im Neuenheimer Feld 368, Raum 422, 69120 Heidelberg, Germany.

³Universität Koblenz-Landau, Institute for Environmental Sciences, Group of Environmental and Soil Chemistry, Fortstr. 7, D-76829 Landau, Germany.

⁴Institute of Soil Science and Plant Nutrition, Martin-Luther-University Halle-Wittenberg, Von-Seckendorff-Platz 3, 06120 Halle-Saale.

*Corresponding Author. Tel: +49 345 558 5215

Email addresses: samuel.kumahor@ufz.de (Samuel K. Kumahor), pavel.hron@iwr.uni-heidelberg.de (Pavel Hron), metreveli@uni-landau.de (G. Metreveli), schaumann@uni-landau.de (G.E. Schaumann), hans-joerg.vogel@ufz.de (Hans-Jörg Vogel).

Calculation of extended DLVO interactions

The interactions between Ag NPs and collector were calculated according to the DLVO and extended DLVO models. The van der Waals interaction Energy E'_{vdW}

$[\text{ML}^2\text{T}^{-2}]$ was calculated under assumption of sphere–plate interaction using following equation [29]:

$$E'_{vdW} = -\frac{A_{132}}{6} \left[\frac{r_{NP}}{h_s} + \frac{r_{NP}}{h_s + 2r_{NP}} + \ln \left(\frac{h_s}{h_s + 2r_{NP}} \right) \right] \quad (\text{A.1})$$

where A_{132} $[\text{ML}^2\text{T}^{-2}]$ is the Hamaker constant in the used system (nanoparticles and collectors in aqueous solution), r_{NP} [L] is the radius of NP and h_s [L] is the separation distance between NP and collector surface. The Hamaker constant used in equation B.2 is calculated according to the following expression [29]:

$$A_{132} \approx \left(\sqrt{A_{11}} - \sqrt{A_{33}} \right) \left(\sqrt{A_{22}} - \sqrt{A_{33}} \right) \quad (\text{A.2})$$

where A_{11} $[\text{ML}^2\text{T}^{-2}]$ is the Hamaker constant of the nanoparticle, A_{22} $[\text{ML}^2\text{T}^{-2}]$ is the Hamaker constant of the collector and A_{33} $[\text{ML}^2\text{T}^{-2}]$ is the Hamaker constant of the aqueous solution. The electrical double layer interaction energy E'_{EDL} $[\text{ML}^2\text{T}^{-2}]$ was calculated under assumption of sphere (NP)–plate (collector) interaction according to the linear superposition approximation [11]:

$$E'_{EDL} = 64\pi\epsilon\epsilon_0 r_{NP} \left(\frac{kT}{z_{el}e} \right)^2 \frac{\exp \left(\frac{z_{el}e\Phi_{NP}}{2kT} \right) - 1}{\exp \left(\frac{z_{el}e\Phi_{CL}}{2kT} \right) - 1} \frac{\exp \left(\frac{z_{el}e\Phi_{NP}}{2kT} \right) + 1}{\exp \left(\frac{z_{el}e\Phi_{CL}}{2kT} \right) + 1} \exp(-\kappa h_s) \quad (\text{A.3})$$

where ϵ [-] is the dimensionless dielectric constant of the aqueous solution, ϵ_0 $[\text{M}^{-1}\text{L}^{-3}\text{T}^4\text{A}^2]$ is the permittivity of vacuum, k $[\text{ML}^2\text{T}^{-2}\text{K}^{-1}]$ is the Boltzmann constant, T [K] is the absolute temperature, z_{el} [-] is the charge number of the electrolyte, e [TI] is the charge of an electron, Φ_{NP} $[\text{ML}^2\text{T}^{-3}\text{A}^{-1}]$ is the surface potential of the nanoparticles, Φ_{CL} $[\text{ML}^2\text{T}^{-3}\text{A}^{-1}]$ is the surface potential of the collector and κ $[\text{L}^{-1}]$ is the Debye–Hückel parameter, which is estimated from the following expression [11]:

$$\kappa = \sqrt{\frac{1000e^2 N_A}{\epsilon\epsilon_0 kT} \sum c_i z_i^2} \quad (\text{A.4})$$

where N_A [N] is the Avogadro constant, c_i $[\text{NL}^{-3}]$ is the molar concentration of the ion i and z_i [-] is the charge number of the ion i . The hydrophobic interaction energy E_{HYD} $[\text{ML}^2\text{T}^{-2}]$ between nanoparticles and collector surface was calculated

using following equation [114]:

$$E'_{HYD} = \frac{-10^{0.5a}(\cos \Theta_{NP} + \cos \Theta_{CL}) + b}{h_s} r_{NP} \quad (\text{A.5})$$

where Θ_{NP} [-] is the contact angle of the nanoparticle–water surface, Θ_{CL} [-] is the contact angle of the collector–water surface and a and b are the system–specific constants. The dimensionless van der Waals (E'_{vdW}), electric double layer (E'_{EDL}) and hydrophobic (E'_{HYD}) interaction energies are calculated by dividing E'_{vdW} , E'_{EDL} and E'_{HYD} by kT . The dimensionless total DLVO interaction energy EDLVO was calculated as the sum of dimensionless van der Waals and electric double layer interaction energies:

$$E_{DLVO} = E_{vdW} + E_{EDL} \quad (\text{A.6})$$

The extension for hydrophobic interaction is justified by the presence of AWI and citrate which is amphiphilic. The dimensionless total extended DLVO interaction energy E_{eDLVO} was calculated as the sum of dimensionless van der Waals, electric double layer and hydrophobic interaction energies:

$$E_{eDLVO} = E_{vdW} + E_{EDL} + E_{HYD} \quad (\text{A.7})$$

A sphere (NP)–plate (collector) interaction (e.g., [11, 29, 89]) was considered given a small d_h of Ag NP (about 40 nm) relative to either the r of the AWI (varies with θ) or d_{50} . Constants and input parameters used for the calculation of the DLVO and eDLVO interaction energies are listed in Table A.1.

TABLE A.1: Input parameters and physical constants used for the calculation of the total interaction energy between nanoparticles and collector.

Parameter	Symbol	Dimension symbol	Unit	Value	Source
Hamaker constant of Ag NPs	A_{11}	$[\text{ML}^2\text{T}^{-2}]$	J	1.558×10^{-19}	[70]
Hamaker constant of SWI ^a	A_{22}	$[\text{ML}^2\text{T}^{-2}]$	J	6.5×10^{-20}	[11]
Hamaker constant of AWI ^b	A_{22}	$[\text{ML}^2\text{T}^{-2}]$	J	0	[11]
Hamaker constant of the aqueous solution	A_{33}	$[\text{ML}^2\text{T}^{-2}]$	J	3.7×10^{-20}	[11]
Radius of the Ag NPs at pH 5	r_{NP}	[L]	m	2.46×10^{-8}	This work
Radius of the Ag NPs at pH 9	r_{NP}	[L]	m	1.98×10^{-8}	This work
Dimensionless dielectric constant of the aqueous solution	ϵ	[-]	-	81	-
Permittivity of vacuum	ϵ_0	$[\text{M}^{-1}\text{L}^{-3}\text{T}^4\text{A}^2]$	$\text{J}^{-1}\text{C}^2\text{m}^{-1}$	8.854×10^{-12}	-
Boltzmann constant	k	$[\text{ML}^2\text{T}^{-2}\Theta^{-1}]$	JK^{-1}	1.38×10^{-23}	-
Absolute temperature	T	$[\Theta]$	JK^{-1}	298.15	-
Charge number of K^+ cation	Z_{K^+}	[-]	-	1	-
Charge number of NO_3^- anion	$Z_{Nitrate}$	[-]	-	1	-
Charge number of citrate ($\text{C}_6\text{H}_5\text{O}_7^{3-}$) anion	$Z_{citrate}$	[-]	-	3	-
Charge of an electron	e	[TI]	C	1.602×10^{-19}	-
Surface potential of Ag NPs at pH 5	Φ_{NP}	$[\text{ML}^2\text{T}^{-3}\text{A}^{-1}]$	V	-0.032 ^c	This work
Surface potential of Ag NPs at pH 9	Φ_{NP}	$[\text{ML}^2\text{T}^{-3}\text{A}^{-1}]$	V	-0.052 ^c	This work
Surface potential of SWI ^a at pH 5	Φ_{CL}	$[\text{ML}^2\text{T}^{-3}\text{A}^{-1}]$	V	-0.047 ^c	[45]
Surface potential of SWI ^a at pH 9	Φ_{CL}	$[\text{ML}^2\text{T}^{-3}\text{A}^{-1}]$	V	-0.055 ^c	[45]
Surface potential of AWI ^b at pH 5	Φ_{CL}	$[\text{ML}^2\text{T}^{-3}\text{A}^{-1}]$	V	-0.050 ^c	[57]
Surface potential of AWI ^b at pH 9	Φ_{CL}	$[\text{ML}^2\text{T}^{-3}\text{A}^{-1}]$	V	-0.072 ^c	[57]
Avogadro constant	N_A	[N]	mol^{-1}	6.022×10^{23}	-
System-specific constant	a	[-]	-	-5	[75]
System-specific constant	b	[-]	-	-20	[75]
Contact angle of Ag NP-water surface	Θ_{NP}	[-]	°	40	[39]
Contact angle of SWI ^a	Θ_{CL}	[-]	°	30	[53]
Contact angle of AWI ^b	Θ_{CL}	[-]	°	180	[39]

^aSWI: solid-water interface^bAWI: air-water interface^cThe values represent ζ potential, which was assumed to be equal to the surface potential.

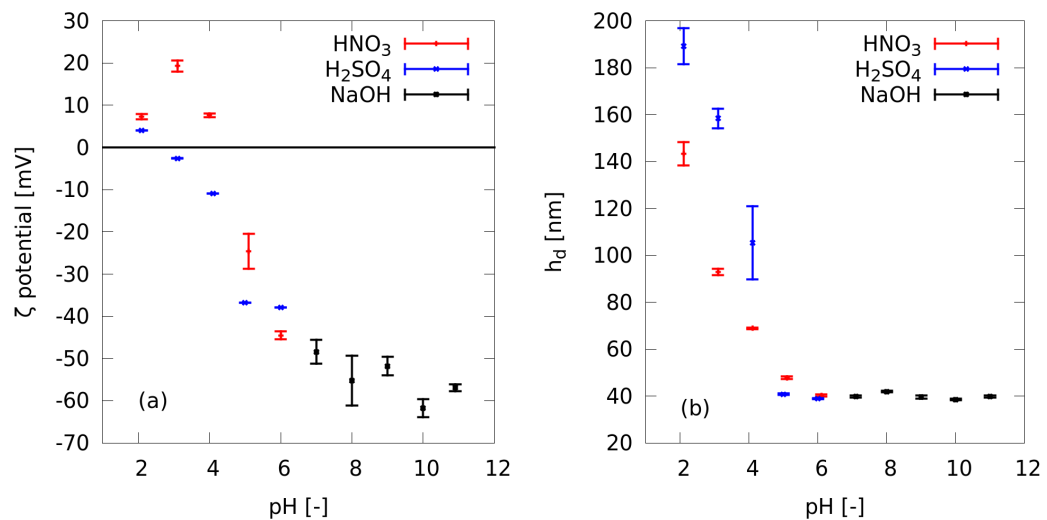


FIGURE A.1: (a) Hydrodynamic diameter (h_d) of citrate-coated Ag nanoparticles (NPs) as a function of pH. The dispersion pH was adjusted in the range from neutral (pH = 7) to basic (pH = 11) using NaOH (black) while in the acidic (pH 2 to 6) range using either HNO₃ (red) or H₂SO₄ (blue). The average h_d value was calculated from 6 values obtained from 2 measurements (thus each measurement is repeated three times) (b) Zeta (ζ) potential of citrate-coated Ag NPs as a function of pH. The dispersion pH was adjusted in the range from neutral (pH = 7) to basic (pH = 11) using NaOH (black) while in the acidic range (pH = 2 to 6) using either HNO₃ (red) or H₂SO₄ (blue). The average ζ potential value was calculated from 6 values obtained from 2 measurements (thus each measurement is repeated three times).

Appendix B

Supplementary data

The section on the calculation of extended DLVO interactions was modified after Kumahor et al. [51]

Transport of soil-aged Ag nanoparticle in unsaturated sand

Samuel K. Kumahor^{a,*}, Pavel Hron^b, George Metreveli^c, Gabriele E. Schaumann^c, Sonda Klitzke^{d,e}, Friederike Lang^d Hans-Jörg Vogel^{a,f}.

^aDepartment of Soil Physics, Helmholtz Centre for Environmental Research–UFZ, Theodor–Lieser–Strasse 4, 06120 Halle–Saale, Germany

^bInterdisciplinary Center for Scientific Computing, University of Heidelberg, Im Neuenheimer Feld 368, Raum 422, 69120 Heidelberg, Germany

^cUniversität Koblenz–Landau, Institute for Environmental Sciences, Group of Environmental and Soil Chemistry, Fortstr. 7, D–76829 Landau, Germany

^dAlbert–Ludwigs–Universität Freiburg, Chair of Soil Ecology, D–79085 Freiburg

^eTechnische Universität Berlin, Institute for Ecology, Department of Soil Science, Ernst–Reuter–Platz 1, D–10587 Berlin

^fInstitute of Soil Science and Plant Nutrition, Martin–Luther–University Halle–Wittenberg, Von–Seckendorff–Platz 3, 06120 Halle–Saale, Germany

*Corresponding Author. Tel: +49 345 558 5215

E-mail addresses: samuel.kumahor@ufz.de (S.K. Kumahor), pavel.hron@iwr.uni-heidelberg.de (P. Hron), metreveli@uni-landau.de (G. Metreveli), schaumann@uni-landau.de (G.E. Schumann), Sondra.klitzke@tu-berlin.de (S. Klitzke), friederike.lang@bodenkunde.uni-freiburg.de (F. Lang), and hans-joerg.vogel@ufz.de (H.-J. Vogel).

Calculation of extended DLVO interactions

The following text, dedicated to calculation of extended Derjaguin–Landau–Verwey–Overbeek (eDLVO) interaction, was modified after Kumahor et al. [51]. Interaction between collector (i.e., air–water, AWI and solid–water interfaces, SWI) and soil–aged Ag nanoparticles (NPs) was calculated according to the eDLVO model. The eDLVO model includes (i) van der Waals (E'_{vdW}), (ii) electrical double layer (E'_{EDL}) and (iii) hydrophobic (E'_{HYD}) interaction energies.

The van der Waals interaction Energy E'_{vdW} [ML^2T^{-2}] was calculated under assumption of sphere–plate interaction using following equation [29]:

$$E'_{vdW} = -\frac{A_{132}}{6} \left[\frac{r_{NP}}{h_s} + \frac{r_{NP}}{h_s + 2r_{NP}} + \ln\left(\frac{h_s}{h_s + 2r_{NP}}\right) \right] \quad (\text{B.1})$$

where A_{132} [ML^2T^{-2}] is the Hamaker constant in the used system (nanoparticles and collectors in aqueous solution), r_{NP} [L] is the radius of NP and h_s [L] is the separation distance between NP and collector surface. The Hamaker constant used in equation B.2 is calculated according to the following expression [29]:

$$A_{132} \approx \left(\sqrt{A_{11}} - \sqrt{A_{33}} \right) \left(\sqrt{A_{22}} - \sqrt{A_{33}} \right) \quad (\text{B.2})$$

where A_{11} [ML^2T^{-2}] is the Hamaker constant of the nanoparticle, A_{22} [ML^2T^{-2}] is the Hamaker constant of the collector and A_{33} [ML^2T^{-2}] is the Hamaker constant of the aqueous solution. The electrical double layer interaction energy E'_{EDL} [ML^2T^{-2}] was calculated under assumption of sphere (NP)–plate (collector) interaction according to the linear superposition approximation [11]:

$$E'_{EDL} = 64\pi\epsilon\epsilon_o r_{NP} \left(\frac{kT}{z_{el}e} \right)^2 \frac{\exp\left(\frac{z_{el}e\Phi_{NP}}{2kT}\right) - 1}{\exp\left(\frac{z_{el}e\Phi_{CL}}{2kT}\right) - 1} \frac{\exp\left(\frac{z_{el}e\Phi_{NP}}{2kT}\right) + 1}{\exp\left(\frac{z_{el}e\Phi_{CL}}{2kT}\right) + 1} \exp(-\kappa h_s) \quad (\text{B.3})$$

where ϵ [-] is the dimensionless dielectric constant of the aqueous solution, ϵ_0 [$M^{-1}L^{-3}T^4A^2$] is the permittivity of vacuum, k [$ML^2T^{-2}K^{-1}$] is the Boltzmann constant, T [K] is the absolute temperature, z_{el} [-] is the charge number of the electrolyte, e [TI] is the charge of an electron, Φ_{NP} [$ML^2T^{-3}A^{-1}$] is the surface potential of the nanoparticles, Φ_{CL} [$ML^2T^{-3}A^{-1}$] is the surface potential of the collector and κ [L^{-1}] is the Debye–Hückel parameter, which is estimated from the following expression [11]:

$$\kappa = \sqrt{\frac{1000e^2N_A}{\epsilon\epsilon_0kT} \sum c_i z_i^2} \quad (B.4)$$

where N_A [N] is the Avogadro constant, c_i [NL^{-3}] is the molar concentration of the ion i and z_i [-] is the charge number of the ion i . The hydrophobic interaction energy E_{HYD} [ML^2T^{-2}] between nanoparticles and collector surface was calculated using following equation [114]:

$$E'_{HYD} = \frac{-10^{0.5a}(\cos \Theta_{NP} + \cos \Theta_{CL}) + b}{h_s} r_{NP} \quad (B.5)$$

where Θ_{NP} [-] is the contact angle of the nanoparticle–water surface, Θ_{CL} [-] is the contact angle of the collector–water surface and a and b are the system–specific constants. The dimensionless van der Waals (E_{vdW}), electric double layer (E_{EDL}) and hydrophobic (E_{HYD}) interaction energies are calculated by dividing E'_{vdW} , E'_{EDL} and E'_{HYD} by kT . The dimensionless total extended DLVO interaction energy, E_{eDLVO} , is therefore a sum of the dimensionless van der Waals, electric double layer and hydrophobic interaction energies:

$$E_{eDLVO} = E_{vdW} + E_{EDL} + E_{HYD} \quad (B.6)$$

The input parameters and physical constants used in the calculations are listed in the Table B.1. Additionally the solution chemistry is are listed in Table B.2

TABLE B.1: Input parameters and physical constants used for the calculation of the total interaction energy between nanoparticles and collector.

Parameter	Symbol	Dimension	Unit	Value	Source
Hamaker constant of Ag NPs	A_{11}	$[\text{ML}^2\text{T}^{-2}]$	J	1.558×10^{-19}	[70]
Hamaker constant of SWI ^a	A_{22}	$[\text{ML}^2\text{T}^{-2}]$	J	6.5×10^{-20}	[11]
Hamaker constant of AWI ^b	A_{22}	$[\text{ML}^2\text{T}^{-2}]$	J	0	[11]
Hamaker constant of the aqueous solution	A_{33}	$[\text{ML}^2\text{T}^{-2}]$	J	3.7×10^{-20}	[11]
Radius of the Ag NPs at pH 5	r_{NP}	[L]	m	1.07×10^{-7}	This work
Radius of the Ag NPs at pH 9	r_{NP}	[L]	m	1.00×10^{-7}	This work
Dimensionless dielectric constant of the aqueous solution	ϵ	[—]	—	81	—
Permittivity of vacuum	ϵ_0	$[\text{M}^{-1}\text{L}^{-3}\text{T}^4\text{A}^2]$	$\text{J}^{-1}\text{C}^2\text{m}^{-1}$	8.854×10^{-12}	—
Boltzmann constant	k	$[\text{ML}^2\text{T}^{-2}\Theta^{-1}]$	JK^{-1}	1.38×10^{-23}	—
Absolute temperature	T	$[\Theta]$	JK^{-1}	298.15	—
Charge of an electron	e	[TI]	C	1.602×10^{-19}	—
Surface potential of Ag NPs at pH 5	Φ_{NP}	$[\text{ML}^2\text{T}^{-3}\text{A}^{-1}]$	V	-0.0142 ^c	This work
Surface potential of Ag NPs at pH 9	Φ_{NP}	$[\text{ML}^2\text{T}^{-3}\text{A}^{-1}]$	V	-0.0205 ^c	This work
Surface potential of SWI ^a at pH 5	Φ_{CL}	$[\text{ML}^2\text{T}^{-3}\text{A}^{-1}]$	V	-0.047 ^c	[45]
Surface potential of SWI ^a at pH 9	Φ_{CL}	$[\text{ML}^2\text{T}^{-3}\text{A}^{-1}]$	V	-0.055 ^c	[45]
Surface potential of AWI ^b at pH 5	Φ_{CL}	$[\text{ML}^2\text{T}^{-3}\text{A}^{-1}]$	V	-0.050 ^c	[57]
Surface potential of AWI ^b at pH 9	Φ_{CL}	$[\text{ML}^2\text{T}^{-3}\text{A}^{-1}]$	V	-0.072 ^c	[57]
Avogadro constant	N_A	[N]	mol^{-1}	6.022×10^{23}	—
system-specific constant	a	[—]	—	-5	[75]
system-specific constant	b	[—]	—	-20	[75]
Contact angle of Ag NP–water surface	Θ_{NP}	[—]	°	40 (30 ^d , 50 ^d)	[39]
Contact angle of SWI ^a	Θ_{CL}	[—]	°	30	[53]
Contact angle of AWI ^b	Θ_{CL}	[—]	°	180	[39]

^aSWI: solid–water interface^bAWI: air–water interface^cThe values represent ζ potential, which was assumed to be equal to the surface potential.^dThese values were chosen as slightly lower and higher compared to the contact angle (40°) from the literature.

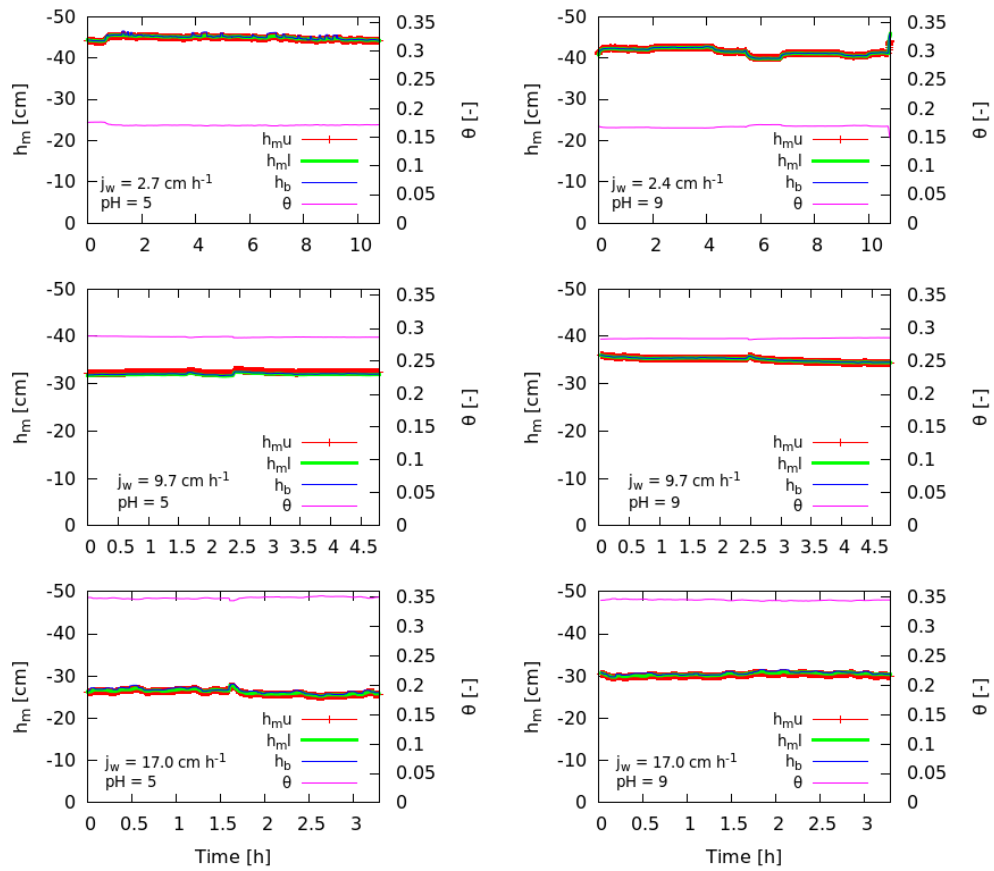


FIGURE B.1: Hydraulic states during transport. The parameters $h_{m,u}$, $h_{m,l}$ and h_b , represent lower, upper and boundary pressure heads respectively while θ , and j_w are water content and flow rate respectively. Considering a bulk density (ρ_b) of 1.52 g cm^{-3} and a particle density (ρ_s) of 2.65 g cm^{-3} for mineral soils, the total porosity is calculated to be 0.42 (volume basis).

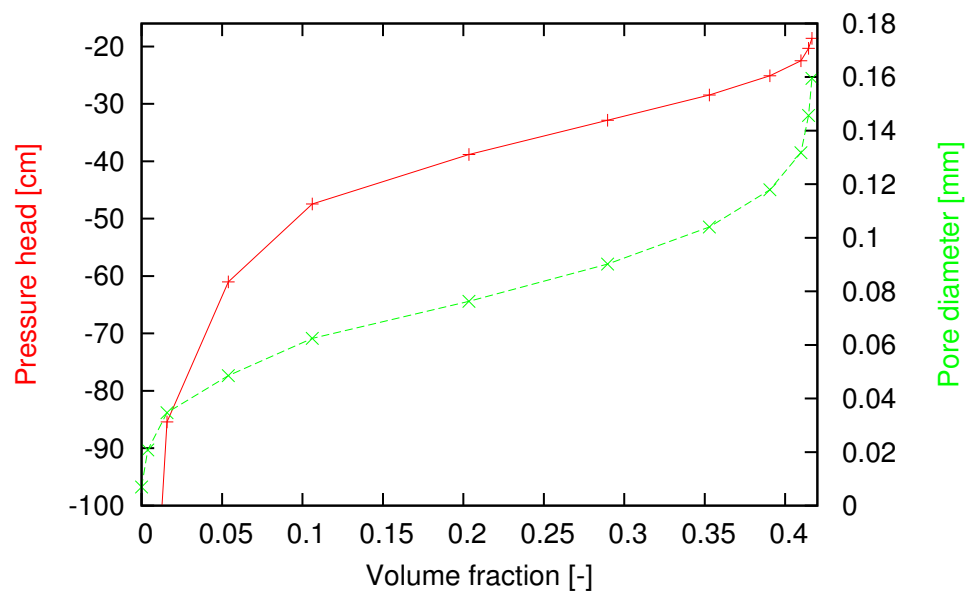


FIGURE B.2: Pressure head (red) and size distribution (green) of pores versus volume fraction of pores derived from X-ray computer tomography (CT) images and pore structure analysis. The figure was obtained at a state of energetic minimum assuming spherical air–water interfaces and complete wettability of the pore surfaces using the Young–Laplace Equation.

TABLE B.2: Major constituents in eluate collected between the 7th and 8th pore volume. Addition of HNO₃ to adjust pH elevated NO₃⁻ concentration at pH = 5.

Sample	Na ⁺	K ⁺	Ca ²⁺	Mg ²⁺	Cl ⁻	NO ₃ ⁻	SO ₄ ²⁻	Ionic strength mM
Exp1 ^a	3.57	1.45	4.08	0.86	0.07	22.02	-	0.77
Exp2 ^b	3.79	0.65	1.12	0.04	-	2.48	-	0.39
Exp3 ^c	3.48	0.86	6.90	0.93	0.22	24.92	-	0.94
Exp4 ^d	5.70	0.99	4.04	0.54	-	7.14	-	0.66
Exp5 ^e	3.82	0.96	8.70	1.19	0.30	26.35	0.025	1.07
Exp6 ^f	5.47	0.66	6.87	0.81	0.32	5.11	-	0.81

^a J_{fw} = 2.7 cm h⁻¹, pH = 5

^b J_{fw} = 2.4 cm h⁻¹, pH = 9

^c J_{fw} = 9.7 cm h⁻¹, pH = 5

^d J_{fw} = 9.7 cm h⁻¹, pH = 9

^e J_{fw} = 17 cm h⁻¹, pH = 5

^f J_{fw} = 17 cm h⁻¹, pH = 9

Bibliography

- [1] Abraham, P. (2015). *Attachment of engineered silver nanoparticles to collector surfaces - A batch sorption study using model and environmental surfaces* . PhD thesis.
- [2] Abraham, P., Barnikol, S., Baumann, T., Kühn, M., Ivleva, N., and Schaubmann, G. (2013). Sorption of silver nanoparticles to environmental and model surfaces. ... *science & technology*, 47:50835091.
- [3] Adegboyega, N., Sharma, V., Siskova, K., Zbor, R., Sohn, M., Schultz, B., and Banerjee, S. (2013). Interactions of Aqueous Ag + with Fulvic Acids: Mechanisms of Silver Nanoparticle Formation and Investigation of Stability. *Environ. Sci. Technol.*, 47:757–764.
- [4] Aitken, R., Chaudhry, M., Boxall, A., and Hull, M. (2006). Manufacture and use of nanomaterials: current status in the UK and global trends. *Occupational medicine (Oxford, England)*, 56(5):300–6.
- [5] Akaighe, N., Depner, S., Banerjee, S., and Sohn, M. (2013). Transport and deposition of Suwannee River Humic Acid/Natural Organic Matter formed silver nanoparticles on silica matrices: the influence of solution pH and ionic strength. *Chemosphere*, 92(4):406–12.
- [6] Arnaudov, L., Cayre, O., Stuart, M., Stoyanov, S., and Paunov, V. (2010). Measuring the three-phase contact angle of nanoparticles at fluid interfaces. *Phys Chem Chem Phys.*, 12(2):363–373.
- [7] Atkins, P. and de Paula, J. (2006). *Physical chemistry*. W. H. Freeman and Company, eighth edi edition.
- [8] Baalousha, M. (2009). Aggregation and disaggregation of iron oxide nanoparticles: Influence of particle concentration, pH and natural organic matter. *The Science of the total environment*, 407:2093–101.

- [9] Badawy, A., Hassan, A., Scheckel, K., Suidan, M., and Tolaymat, T. (2013). Key factors controlling the transport of silver nanoparticles in porous media. *Environmental Science & Technology*, 47:4039–4045.
- [10] Bae, S., Hwang, Y., Lee, Y.-J., and Lee, S.-K. (2013). Effects of Water Chemistry on Aggregation and Soil Adsorption of Silver Nanoparticles. *Environmental Health and Toxicology*, 28:1–7.
- [11] Bradford, S. and Torkzaban, S. (2008). Colloid Transport and Retention in Unsaturated Porous Media: A Review of Interface-, Collector-, and Pore-Scale Processes and Models. *Vadose Zone Journal*, 7(2):667–681.
- [12] Bradford, S., Torkzaban, S., and Šimůnek, J. (2011). Modeling colloid transport and retention in saturated porous media under unfavorable attachment conditions. *Water Resources Research*, 47(W10503):1–12.
- [13] Bradford, S., Šimůnek, J., Bettahar, M., van Genuchten, M., and Yates, S. (2003). Modeling colloid attachment, straining, and exclusion in saturated porous media. *Environmental Science & Technology*, 37:2242–2250.
- [14] Bradford, S., Šimůnek, J., Bettahar, M., van Genuchten, M., and Yates, S. (2006). Significance of straining in colloid deposition: Evidence and implications. *Water Resources Research*, 42(W12S15):1–16.
- [15] Bradford, S., Yates, S., Bettahar, M., and Šimůnek, J. (2002). Physical factors affecting the transport and fate of colloids in saturated porous media. *Water Resources Research*, 38(12):63–1–63–12.
- [16] Chen, G. and Flury, M. (2005). Retention of mineral colloids in unsaturated porous media as related to their surface properties. *Colloids and Surfaces A: Physicochemical and Engineering Aspects*, 256:207–216.
- [17] Cho, S.-H., Kim, J.-Y., Chun, J.-H., and Kim, J.-D. (2005). Ultrasonic formation of nanobubbles and their zeta-potentials in aqueous electrolyte and surfactant solutions. *Colloids and Surfaces A: Physicochemical and Engineering Aspects*, 269:28–34.
- [18] Choi, O., Deng, K., Kim, N.-J., Ross, L., Surampalli, R., and Hu, Z. (2008). The inhibitory effects of silver nanoparticles, silver ions, and silver chloride colloids on microbial growth. *Water Research*, 42:3066–74.

- [19] Chowdhury, I., Hong, Y., Honda, R., and Walker, S. (2011). Mechanisms of TiO₂ nanoparticle transport in porous media: role of solution chemistry, nanoparticle concentration, and flowrate. *Journal of colloid and interface science.*, 360(2):548–55.
- [20] Chun, M.-S. and Lee, I. (2008). Rigorous estimation of effective protein charge from experimental electrophoretic mobilities for proteomics analysis using microchip electrophoresis. *Colloids and Surfaces A: Physicochemical and Engineering Aspects.*, 318(1-3):191–198.
- [21] Cuenca, A., Jiang, H., Hochwald, S., Delano, M., Cance, W., and Grobmyer, S. (2006). Emerging implications of nanotechnology on cancer diagnostics and therapeutics. *Cancer*, 107(3):459–66.
- [22] Cumberland, S. and Lead, J. (2009). Particle size distributions of silver nanoparticles at environmentally relevant conditions. *Journal of chromatography A.*, 1216(52):9099–105.
- [23] Dagan, G. (1986). Statistical Theory of Groundwater Flow and Transport' Pore to Laboratory, Laboratory to Formation, and Formation to Regional Scale. *Water Resources Research.*, 22(9):120S–134S.
- [24] De Smedt, F., Wauters, F., and Sevilla, J. (1986). Study of Tracer Movement through Unsaturated Sand. *Journal of Hydrology*, 85:169–181.
- [25] Diamantopoulos, E. and Durner, W. (2012). Dynamic Nonequilibrium of Water Flow in Porous Media: A Review. *Vadose Zone Journal.*, 11(3):1–18.
- [26] Diamantopoulos, E., Iden, S., and Durner, W. (2012). Inverse modeling of dynamic nonequilibrium in water flow with an effective approach. *Water Resources Research.*, 48:1–16.
- [27] El Badawy, A., Luxton, T., Silva, G., K.G., S., Suidan, M., and Thabet, T. (2010). Impact of environmental conditions (pH, ionic strength, and electrolyte type) on the surface charge and aggregation of silver nanoparticles suspensions. *Environmental science & technology*, 44(4):1260–1266.
- [28] El Badawy, A., Scheckel, K., Suidan, M., and Tolaymat, T. (2012). The impact of stabilization mechanism on the aggregation kinetics of silver nanoparticles. *The Science of the Total Environment.*, 429:325–31.

- [29] Elimelech, M., Gregory, J., Jia, X., and Williams, R. (1995). *Particle Deposition and Aggregation - Measurement, Modelling and Simulation*. Elsevier.
- [30] Elimelech, M., Nagai, M., Ko, C.-H., and Ryan, J. (2000). Relative Insignificance of Mineral Grain Zeta Potential to Colloid Transport in Geochemically Heterogeneous Porous Media. *Environmental Science & Technology.*, 34:2143–2148.
- [31] Elimelech, M. and O’Melia, C. (1990). Kinetics of Deposition of Colloidal Particles in Porous Media. *Environmental Science & Technology.*, 24(10):1528–1536.
- [32] Fang, J., Xu, M.-J., Wang, D.-J., Wen, B., and Han, J.-Y. (2013). Modeling the transport of TiO₂ nanoparticle aggregates in saturated and unsaturated granular media: effects of ionic strength and pH. *Water Research.*, 47(3):1399–1408.
- [33] Gelhar, L. (1986). Stochastic Subsurface Hydrology From Theory to Applications. *Water Resources Research.*, 22(9):135S–145S.
- [34] Griffioen, J., Barry, D., and Parlange, J.-Y. (1998). Interpretation of two-region model parameters. *Water Resources Research.*, 34(3):373–384.
- [35] Hilpert, M. and Miller, C. (2001). Pore-morphology-based simulation of drainage in totally wetting porous media. *Advances in Water Resources.*, 24:243–255.
- [36] Hopmans, J. W., Šimůnek, J., Romano, N., and Durner, W. (2002). *Simultaneous determination of water transmission and retention properties-Inverse methods*. In: J.H. Dane and G.C. Topp, editors, *Methods of soil analysis, Part 4. Physical methods*. SSSA Book Ser. 5. SSSA.
- [37] Hoshen, J. and Kopelman, R. (1976). Percolation and cluster distribution: Cluster multiple labeling technique and critical concentration algorithm. *Physical Review B.*, 14(8):3438–3446.
- [38] Hron, P., Jost, D., Bastian, P., Gallert, C., Winter, J., and Ippisch, O. (2014). Application of reactive transport modelling to growth and transport of microorganisms in the capillary fringe. page 17.

- [39] Hu, J.-W., Han, G.-B., Ren, B., Sun, S.-G., and Tian, Z.-Q. (2004). Theoretical Consideration on Preparing Silver Particle Films by Adsorbing Nanoparticles from Bulk Colloids to an Air - Water Interface. *American Chemical Society.*, 20:8831–8838.
- [40] Huynh, K. and Chen, K. (2011). Aggregation kinetics of citrate and polyvinylpyrrolidone coated silver nanoparticles in monovalent and divalent electrolyte solutions. *Environmental Science & Technology*, 45(13):5564–71.
- [41] Huysmans, M. and Dassargues, A. (2004). Review of the use of Péclet numbers to determine the relative importance of advection and diffusion in low permeability environments. *Hydrogeology Journal.*, 13(5–6):895–904.
- [42] Ippisch, O., Vogel, H.-J., and Bastian, P. (2006). Validity limits for the van GenuchtenMualem model and implications for parameter estimation and numerical simulation. *Advances in Water Resources.*, 29(12):1780–1789.
- [43] Jada, A., Akbour, A., and Douch, J. (2006). Surface charge and adsorption from water onto quartz sand of humic acid. *Chemosphere*, 64(8):1287–95.
- [44] Jiang, H., Moon, K.-S., Lu, J., and Wong, C. (2005). Conductivity Enhancement of Nano Silver-Filled Conductive Adhesives by Particle Surface Functionalization. *Journal of ELECTRONIC MATERIALS.*, 34(11):1432–1439.
- [45] Johnson, P. (1999). A Comparison of Streaming and Microelectrophoresis Methods for Obtaining the ζ Potential of Granular Porous Media Surfaces. *Journal of Colloid and Interface Science.*, 267:264–267.
- [46] Johnson, R., Johnson, G., Nurmi, J., and Tratnyek, P. (2009). Natural Organic Matter Enhanced Mobility of Nano Zerovalent Iron. *Environmental Science & Technology.*, 43:5455–5460.
- [47] Kasel, D., Bradford, S., Šimůnek, J., Heggen, M., Vereecken, H., and Klumpp, E. (2013). Transport and retention of multi-walled carbon nanotubes in saturated porous media: effects of input concentration and grain size. *Water Research.*, 47:933–44.
- [48] Khlebtsov, B. and Khlebtsov, N. (2011). On the measurement of gold nanoparticle sizes by the dynamic light scattering method. *Colloid Journal.*, 73(1):118–127.

- [49] Klitzke, S., Metreveli, G., Peters, A., Schaumann, G., and Lang, F. (2015). The fate of silver nanoparticles in soil solution - Sorption of solutes and aggregation. *The Science of the Total Environment.*, 535:54–60.
- [50] Kumahor, S., de Rooij, G., Schlüter, S., and Vogel, H.-J. (2015a). Water Flow and Solute Transport in Unsaturated Sand A Comprehensive Experimental Approach. *Vadose Zone Journal.*, 14(2).
- [51] Kumahor, S., Hron, P., Metreveli, G., Schaumann, G., and Vogel, H.-J. (2015b). Transport of citrate-coated silver nanoparticles in unsaturated sand. *The Science of the total environment.*
- [52] L., C. K. and Elimelech, M. (2008). Interaction of Fullerene (C60) Nanoparticles with Humic Acid and Alginate Coated Silica Surfaces: Measurements, Mechanisms, and Environmental Implications. *Environmental Science and Technology.*, 42(20):7607–7614.
- [53] Lamparter, A., Bachmann, J., Woche, S., and Goebel, M.-O. (2014). Biogeochemical Interface Formation: Wettability Affected by Organic Matter Sorption and Microbial Activity. *Vadose Zone Journal*, 13(7).
- [54] Lau, B., Hockaday, W., Ikuma, K., Furman, O., and Decho, A. (2013). A preliminary assessment of the interactions between the capping agents of silver nanoparticles and environmental organics. *Colloids and Surfaces A: Physicochemical and Engineering Aspects*, 435:22–27.
- [55] Lazouskaya, V., Jin, Y., and Or, D. (2006). Interfacial interactions and colloid retention under steady flows in a capillary channel. *Journal of colloid and interface science*, 303:171–84.
- [56] Lee, Y., Chou, W., and Chen, L. (1998). The adsorption and nucleation of water vapor on an insoluble spherical solid particle. *Surf Sci.*, 414(3):363–373.
- [57] Li, C. and Somasundaran, P. (1991). Reversal of Bubble Charge in Multivalent Inorganic Salt Solutions-Effect of Magnesium. *Journal of Colloid and Interface Science.*, 146(1):215–218.
- [58] Li, X., Scheibe, T., and Johnson, W. (2004). Apparent Decreases in Colloid Deposition Rate Coefficients with Distance of Transport under Unfavorable Deposition Conditions : A General Phenomenon. *Environmental Science & Technology.*, 38(21):5616–5625.

- [59] Liang, Y., Bradford, S., Šimůnek, J., Heggen, M., Vereecken, H., and Klumpp, E. (2013a). Retention and remobilization of stabilized silver nanoparticles in an undisturbed loamy sand soil. *Environmental Science & Technology.*, 47:1222912237.
- [60] Liang, Y., Bradford, S., Šimůnek, J., Vereecken, H., and Klumpp, E. (2013b). Sensitivity of the transport and retention of stabilized silver nanoparticles to physicochemical factors. *Water Research.*, 7:2572–2582.
- [61] Maraqa, M. A., Wallace, R. B., and Voice, T. C. (1997). Effects of degree of water saturation on dispersivity and immobile water in sandy soil columns. *Journal of Contaminant Hydrology.*, 25:199–218.
- [62] Matsubayashi, U., Devkota, L., and Takagi, F. (1997). Characteristics of the dispersion coefficient in miscible displacement through a glass beads medium. *Journal of Hydrology.*, 192:51–64.
- [63] Mbamala, E. and von Grünberg, H. (2003). Charged colloids and proteins at an air-water interface: The effect of dielectric substrates on interaction and phase behavior. *Physical Review E*, 67(3):031608–11.
- [64] McCarthy, J. and McKay, L. (2004). Colloid Transport in the Subsurface : Past , Present , and Future Challenges. *Soil Science Society of America Journal.*, 3:326–337.
- [65] Metreveli, G., Philippe, A., and Schaumann, G. (2014). Disaggregation of silver nanoparticle homoaggregates in a river water matrix. *The Science of the total environment*, 535:35–44.
- [66] Mualem, Y. (1984). A modified dependent domain theory of hysteresis. *Soil Science.*, 137(5):283–291.
- [67] Padilla, I., Yeh, T.-C., and Conklin, M. (1999). The effect of water content on solute transport in unsaturated porous media. *Water Resources Research.*, 35(11):3303–3313.
- [68] Phenrat, T., Kim, H.-J., Illangasekare, T., Tilton, D. R., and Lowry, G. (2009). Particle Size Distribution , Concentration , and Magnetic Attraction Affect Transport of Polymer-Modified Fe₀ Nanoparticles in Sand Columns. *Environmental Science and Technology.*, 43(13):5079–5085.

- [69] Philippe, A. and Schaumann, G. (2014). Interactions of Dissolved Organic Matter with Natural and Engineered Inorganic Colloids : A Review. *Environ. Sci. Technol.*, 48:8946–8962.
- [70] Pinchuk, A. (2012). Size-Dependent Hamaker Constant for Silver Nanoparticles. *Journal of Physical Chemistry*, 116:20099–20102.
- [71] Raoof, A. and Hassanizadeh, S. (2013). Saturation-dependent solute dispersivity in porous media: Pore-scale processes. *Water Resources Research.*, 49:1943–1951.
- [72] Redman, J., Walker, S., and Elimeiech, M. (2004). Bacterial adhesion and transport in porous media: Role of the secondary energy minimum. *Environmental science & Technology.*, 38(6):1777–1785.
- [73] Ren, D. and Smith, J. (2013). Retention and transport of silver nanoparticles in a ceramic porous medium used for point-of-use water treatment. *Environmental Science & Technology.*
- [74] Richardson, S. D. and Ternes, T. A. (2011). Water Analysis : Emerging Contaminants and Current Issues. *Anal. Chem.*, 83:4614–4648.
- [75] Schäfer, A., Hauke, H., and Zehnder, A. (1998). Bacterial Accumulation at the Air - Water Interface. *Environmental Science & Technology*, 32(23):3704–3712.
- [76] Schaumann, G., Philippe, A., Bundschuh, M., Metreveli, G., Klitzke, S., Rakcheev, D., Grün, A., Kumahor, S., Kühn, M., Baumann, T., Lang, F., Manz, W., Schulz, R., and Vogel, H.-J. (2014). Understanding the fate and biological effects of Ag- and TiO₂-nanoparticles in the environment: The quest for advanced analytics and interdisciplinary concepts. *The Science of the Total Environment.*, (STOTEN-16953):17.
- [77] Schaumann, G., Philippe, A., Bundschuh, M., Metreveli, G., Klitzke, S., Rakcheev, D., Grün, A., Kumahor, S., Kühn, M., Baumann, T., Lang, F., Manz, W., Schulz, R., and Vogel, H.-J. (2015). Understanding the fate and biological effects of Ag- and TiO₂-nanoparticles in the environment: The quest for advanced analytics and interdisciplinary concepts. *The Science of the Total Environment.*, (STOTEN-16953):17.

- [78] Schlüter, S., Sheppard, A., Brown, K., and Wildenschild, D. (2014). Image processing of multiphase images obtained via X-ray microtomography: A review. *Water Resources Research.*, 50:3615–3639.
- [79] Schlüter, S., Weller, U., and Vogel, H.-J. (2010). Segmentation of X-ray microtomography images of soil using gradient masks. *Computers & Geosciences.*, 36(10):1246–1251.
- [80] Seitz, F., Rosenfeldt, R., Storm, K., Metreveli, G. Schaumann, G. S. R., and Bundschuh, M. (2015). Effects of silver nanoparticle properties, media pH and dissolved organic matter on toxicity to *Daphnia magna*. *Ecotoxicology and Environmental Safety*, 111:263–270.
- [81] Sharma, V., Siskova, K., Zboril, R., and Gardea-Torresdey, J. (2014). Organic-coated silver nanoparticles in biological and environmental conditions: fate, stability and toxicity. *Advances in colloid and interface science*, 204:15–34.
- [82] Shen, C., Huang, Y., Li, B., and Jin, Y. (2008). Effects of solution chemistry on straining of colloids in porous media under unfavorable conditions. *Water Resources Research.*, 44(W05419):1–12.
- [83] Sotiriou, G., Sannomiya, T., Teleki, A., Krumeich, F., Vörös, J., and Pratsinis, S. (2010). Non-toxic dry-coated nanosilver for plasmonic biosensors. *Advanced functional materials*, 20:4250–4257.
- [84] Takahashi, M. (2005). A Comparison of Streaming and Microelectrophoresis Methods for Obtaining the ζ Potential of Granular Porous Media Surfaces. *The Journal of Physical Chemistry B*, 109:21858–21864.
- [85] Tate, K. and Theng, B. (1980). Organic matter and its interactions with inorganic soil constituents. In: G.K.G Theng (Editor), Soil with a variable charge. *N.Z. Soc. Soil. Sci. Lower Hutt, New Zealand.*, pages 225–249.
- [86] Topp, G., Klute, A., and Peters, D. (1967). Comparison of water content-pressure head data obtained by equilibrium steady-state and unsteady-state methods. *Soil Sci. Soc. Am. Proc.*, 31:312–314.
- [87] Toride, N., Inoue, M., and Leij, F. (1979). Hydrodynamic Dispersion in an Unsaturated Dune Sand. *Soil Science Society of America Journal.*, 67:703–712.

- [88] Toride, N., Leij, F., and van Genuchten, M. (1995). The CXTFIT Code for Estimating Parameters from Laboratory or Field Tracer Experiments. Technical Report 137.
- [89] Torkzaban, S., Bradford, S., van Genuchten, M., and Walker, S. (2008). Colloid transport in unsaturated porous media: the role of water content and ionic strength on particle straining. *Journal of Contaminant Hydrology.*, 96:113–127.
- [90] Torkzaban, S., Wan, J., Tokunaga, T., and Bradford, S. (2012). Impacts of bridging complexation on the transport of surface-modified nanoparticles in saturated sand. *Journal of contaminant hydrology*, 136-137:86–95.
- [91] Tourinho, P., van Gestel, C., Lofts, S., Svendsen, C., Soares, A., and Loureiro, S. (2012). Metal-based nanoparticles in soil: fate, behavior, and effects on soil invertebrates. *Environmental toxicology and chemistry.*, 31(8):1679–92.
- [92] Tufenkji, N. (2007). Modeling microbial transport in porous media: Traditional approaches and recent developments. *Advances in Water Resources*, 30:1455–1469.
- [93] Tufenkji, N. and Elimelech, M. (2005). Breakdown of colloid filtration theory: Role of the secondary energy minimum and surface charge heterogeneities. *Langmuir*, (18):841–852.
- [94] Vachaud, G., Vauclin, M., and Wakil, M. (1972). A study of the uniqueness of the soil moisture characteristic during desorption by vertical flow in unsaturated porous media. *Soil Sci. Soc. Am. Proc.*, 36:531–532.
- [95] van Dam, J. C., Stricker, J. N. M., and Droogers, P. (1994). Inverse Methods to Determine Soil Hydraulic Functions from Multistep outflow Experiments. *Soil Science Society of America Journal.*, 58:647–652.
- [96] van Genuchten, M. (1980). A closed-form equation for predicting the hydraulic conductivity of unsaturated soils. *Soil Science Society of America Journal.*, 44:892–898.
- [97] Vanderborght, J., Timmerman, A., and Feyen, J. (2000). Solute Transport for Steady-State and Transient Flow in Soils with and without Macropores. *Soil Science Society of America Journal.*, 64:1305–1317.
- [98] Vanderborght, J. and Vereecken, H. (2007). Review of Dispersivities for Transport Modeling in Soils. *Vadose Zone Journal.*, 6(1):29.

- [99] Vogel, H.-J. (1997). Morphological determination of pore connectivity as a function of pore size using serial sections. *European Journal of Soil Science.*, 48(3):365–377.
- [100] Vogel, H.-J. and Kretzschmar, A. (1996). Topological characterization of pore space in soil - sample preparation and digital image-processing. *Geoderma*, 73:23–38.
- [101] Vogel, H.-J. and Roth, K. (2001). Quantitative morphology and network representation of soil pore structure. *Advances in water resources*, 24:233–242.
- [102] Vogel, H.-J., Weller, U., and Schlüter, S. (2010). Quantification of soil structure based on Minkowski functions. *Computers & Geosciences.*, 36(10):1236–1245.
- [103] Šimůnek, J., van Genuchten, M., Senja, M., Toride, N., and Leij, F. (1999). The STANMOD Computer Software for Evaluating Solute Transport in Porous Media Using Analytical Solutions of The STANMOD Computer Software for Evaluating Solute Transport in Porous Media Using Analytical Solutions of Convection-Dispersion Equation. Technical Report November.
- [104] Wan, J. and Wilson, J. (1994a). Colloid transport in unsaturated porous media. *Water Resources Research*, 30:587–864.
- [105] Wan, J. and Wilson, J. (1994b). Visualization of the role of the gas-water interface on the fate and transport of colloids in porous media. *Water Resources Research*, 30:11–23.
- [106] Wang, D., Jaisi, D., Yan, J., Jin, Y., and Zhou, D. (2015). Transport and Retention of Polyvinylpyrrolidone-Coated Silver Nanoparticles in Natural Soils. *Vadose Zone Journal*, 14(7):1–13.
- [107] Wang, Y., Li, Y., and Costanza, J. (2012). Enhanced mobility of fullerene (C60) nanoparticles in the presence of stabilizing agents. *Environmental science & Technology.*, 46:11761–11769.
- [108] Weller, U., Ippisch, O., Köhne, M., and Vogel, H.-J. (2011). Direct Measurement of Unsaturated Conductivity including Hydraulic Nonequilibrium and Hysteresis. *Vadose Zone Journal.*, 10(2):654.
- [109] Weller, U. and Vogel, H.-J. (2012). Conductivity and Hydraulic Nonequilibrium across Drainage and Infiltration Fronts. *Vadose Zone Journal.*, 11(3).

- [110] Wilkinson, K., Negre, J.-C., and Buffle, J. (1997). Coagulation of colloidal material in surface waters : the role of natural organic matter. *Journal of contaminant hydrology*, 26:229–243.
- [111] Willets, K. and van Duyne, R. (2007). Localized surface plasmon resonance spectroscopy and sensing. *Annual Review of Physical Chemistry.*, 58:267–297.
- [112] Xu, C.-Y., Deng, K.-Y., Li, J.-Y., and Xu, R.-K. (2015). Impact of environmental conditions on aggregation kinetics of hematite and goethite nanoparticles. *Journal of Nanoparticle Research*, 17:394.
- [113] Yang, C., Dabros, T., Li, D., Czarnecki, J., and Masliyah, J. (2001). Measurement of the Zeta Potential of Gas Bubbles in Aqueous Solutions by Microelectrophoresis Method. *Journal of Colloid and Interface Science*, 243:128–135.
- [114] Yoon, R., Flinn, D., and Rabinovich, Y. (1997). Hydrophobic interactions between dissimilar surfaces. *Journal of Colloid and Interface Science.*, 185(2):363–370.
- [115] Yu, L., Zhang, Y., Zhang, B., and Liu, J. (2014). Enhanced antibacterial activity of silver nanoparticles/halloysite nanotubes/graphene nanocomposites with sandwich-like structure. *Scientific reports*, 4:4551–5.
- [116] Zhou, D., Bennett, S., and Keller, A. (2012). Increased mobility of metal oxide nanoparticles due to photo and thermal induced disagglomeration. *PloS one*, 7(5):e37363.
- [117] Zurmühl, T. and Durner, W. (1998). Determination of Parameters for Bimodal Hydraulic Functions by Inverse Modeling. *Soil Science Society of America*, 62(4):874–880.

Eidesstattliche Erklärung / Declaration under Oath

Ich erkläre an Eides statt, dass ich die Arbeit selbstständig und ohne fremde Hilfe verfasst, keine anderen als die von mir angegebenen Quellen und Hilfsmittel benutzt und die den benutzten Werken wörtlich oder inhaltlich entnommenen Stellen als solche kenntlich gemacht habe.

I declare under penalty of perjury that this thesis is my own work entirely and has been written without any help from other people. I used only the sources mentioned and included all the citations correctly both in word or content.

Datum / Date

Unterschrift des Antragstellers / Signature of the applicant

Curriculum vitae

Personal data

Name: Samuel Kwame Kumahor
Date of Birth: 01 August 1981

Education

2012–2016: Doctoral studies (Soil Physics)
Helmholtz–Center for Environmental Research–UFZ
Halle (Saale), Germany
2009–2011: Hydrology studies (Hydrogeology specialization)
Free University of Amsterdam, The Netherlands
2006–2008: Soil Science studies
University of Ghana, Legon–Accra, Ghana
2001–2005: Agriculture studies
University of Ghana, Legon–Accra, Ghana

Experience

2012–present: Research fellowship–Structure and function working group
Department of Soil Physics
Helmholtz–Center for Environmental Research–UFZ
Halle (Saale), Germany